



HAL
open science

Laser-plasma acceleration at ultra high intensity - numerical modeling

Emilian-Dragos Tatomirescu

► **To cite this version:**

Emilian-Dragos Tatomirescu. Laser-plasma acceleration at ultra high intensity - numerical modeling. Astrophysics [astro-ph]. Université de Bordeaux; Universitatea de Vest (Timișoara, Roumanie), 2019. English. NNT : 2019BORD0013 . tel-02128435

HAL Id: tel-02128435

<https://theses.hal.science/tel-02128435>

Submitted on 14 May 2019

HAL is a multi-disciplinary open access archive for the deposit and dissemination of scientific research documents, whether they are published or not. The documents may come from teaching and research institutions in France or abroad, or from public or private research centers.

L'archive ouverte pluridisciplinaire **HAL**, est destinée au dépôt et à la diffusion de documents scientifiques de niveau recherche, publiés ou non, émanant des établissements d'enseignement et de recherche français ou étrangers, des laboratoires publics ou privés.



**WEST UNIVERSITY OF
TIMISOARA
FACULTY OF PHYSICS**



**UNIVERSITÉ DE
BORDEAUX
CELIA**

LASER-PLASMA ACCELERATION AT ULTRA HIGH INTENSITY - NUMERICAL MODELING

-PhD Thesis-

28/01/2019

Scientific advisors:

Prof. Dr. Daniel VIZMAN

Prof. Dr. Emmanuel d'HUMIÈRES

Ph.D. Student:

Emilian-Dragoș TATOMIRESCU

Timișoara 2018

Contents

Abstract	5
1. Laser plasma acceleration mechanisms.....	9
1.1. Target normal sheath acceleration	10
1.1.1. Electron component	11
1.1.2. TNSA main mechanism.....	16
1.1.3. Ion beam characteristics	20
1.1.3.1. Particle count	20
1.1.3.2. Energy range	20
1.1.3.3. Opening angle.....	21
1.2. Laser radiation pressure regime	23
1.3. Other related acceleration schemes	24
2. Basic introduction to the Particle-In-Cell method for laser-plasma interaction numerical modeling	26

2.1. Interacting systems classification.....	27
2.2. Interacting systems description.....	29
2.3. Particle-particle approach	31
2.4. Finite-size particles	32
2.5. Particle-in-cell method	34
2.5.1. Iteration cycle	36
2.5.2. Motion equations integration	38
2.5.3. Field equations integration	39
2.5.4. Weighting of particles and forces	41
2.6. Practical considerations when using the PIC method ..	43
2.6.1. Stability	43
2.6.2. Energy conservation.....	44
2.6.3. Diagnostics	44
2.6.4. Normalization and non-dimensional units.....	45
2.6.5. Boundary conditions.....	46

3. Laser ion acceleration from micro-structured solid targets	47
3.1. Simulation parameters	48
3.2. Results and discussion	49
3.2.1. Flat target with microdot.....	50
3.2.2. Curved target with microdot.....	51
3.2.3. Curved target with microdot and a pulse focusing cone-like structure	53
3.2.4. Improving the beam characteristics obtained from laser ion acceleration interaction with micro- structured solid targets	55
3.3. Conclusions on structured targets	57
4. Target curvature influence on particle beam characteristics resulting from laser ion acceleration with microstructured enhanced targets at ultra-high intensity	60
4.1. Simulation parameters	61
4.2. Results and discussions	62
4.3. Conclusions on curvature influence	68

5. Laser ion acceleration and high energy radiation generation from near-critical gas jets	70
5.1. Simulation parameters	71
5.2. Results and discussions	73
5.3. Conclusions on near-critical gas targets	83
6. Final conclusions	84
References	87
Acknowledgments	99
Annexes	101
Scientific activity.....	106

Abstract

Due to the present enhancements in maximum attainable laser intensity through high power short pulses (femtosecond range) an increased focus has grown in developing potential laser plasma sources with applications in proton radiography [1], fast ignition [2], hadrontherapy [3], [4], radioisotope production [5] and laboratory astrophysics [6]. Because of these advances in technology, numerous new laser facilities have been created, allowing the popularization of particle acceleration from laser-plasma interaction as a research field. In recent years, the progress achieved in the field was very rapid, showing that the understanding of the physics that stands behind the interaction of a high intensity laser pulse with plasma has been greatly improved.

The problems that are sought to be solved within this research field require the use of plasmas. At sufficiently high pressures and densities (such as the pressure of the laser light at target surface), molecules can dissociate and atoms can ionize, turning the targets (solid, liquid or gaseous) into a plasma. In this kind of environment, one can state that the dominant processes are of a kinetic and collective nature, with an abundance of non-linear phenomena. This makes the use of analytical or fluid models very difficult, therefore, Particle-In-Cell codes have been crucial in the modelling of such parameters and also in experimental work optimization.

The typical Particle-In-Cell codes in use for laser-plasma interaction numerical modelling solve the electromagnetic fields using Maxwell's equations coupled with the Vlasov equations. The method uses macroparticles (a group of real particles that can be depicted as a reduced portion of the phase space) to solve Vlasov equations by the method of characteristics for each species of particle present in the case under study, conserving the charge and the mass of the species that is under study.

The key factor in the development of all the laser-based applications previously mentioned is the need for collimated ion beams that exhibit an adjustable energy bandwidth. The high repetition requirement can be overcome with the new laser facilities

either available such as the BELLA laser [7], or under construction, such as the ELI-NP facility [8].

The work performed within this thesis sets out to prepare for the first experiments that will be performed at the newly constructed ELI-NP facility. In this regard, several target models are numerically modeled to obtain a roadmap to the first experimental results. The thesis contains a short introduction followed by 6 chapters described in the following:

Chapter 1, named "*Laser plasma acceleration mechanisms*", is dedicated to the description of the physical processes that occur during the interaction of a strong electromagnetic field with a charged plasma. We talk about the main acceleration mechanisms as reported in the specialty literature. Their occurrence depends on the parameters of both the target and the laser pulse (i.e. density, intensity, shape). This chapter is structured in three sections. In the first two we deal with the most common acceleration schemes, while in the third one we discuss the mechanisms that are less common or require special parameters. In the first section we describe the Target Normal Sheath Acceleration and its electron and ion components. The second section deals with characteristics of the Radiation Pressure Acceleration. The last sub-chapter presents short descriptions for the related acceleration schemes and the mechanisms that are particular cases of the ones discussed in the first two sections.

Chapter 2, named "*Basic introduction to the Particle-In-Cell method for laser-plasma interaction numerical modeling*", is envisioned to present the basis on how the Particle-In-Cell method is being utilized in the numerical modeling of laser plasma interaction. The first part starts with two sub-chapters that differentiate and describe the classes of plasma interacting systems. The chapter then continues with a description of the Particle-Particle approach, and reasons on why it is not suited for the kind of phenomena studied in this work. In the third sub-chapter, we begin by describing the Particle-In-Cell method, its basic iteration cycle, how the integration of the equations involved in this method can be performed and the interpolations required by this approach. The chapter ends with a few practical considerations that are being handled when running Particle-In-Cell simulations.

Chapter 3, named "*Laser ion acceleration from micro-structured solid targets*", is structured into three sub-chapters and deals with the first of the studies performed during the last three years. We start with a description of the simulation parameters. The study has been focused on the particularities of several types of density profiles with a proton-rich microdot: flat, curved and cone target with a concave tip. We study the advantages and disadvantages of each of these target modifications (curvature, microdot and cone structure), and determine if a composite target featuring all three attributes has the potential to produce higher quality proton and ion beams. By comparing the cases of flat versus curved targets, we intend to determine what effect has the addition of a slight curvature to the target, in particular how it affects beam collimation. In this chapter we also want to determine the effects of a pulse focusing structure on the laser pulse electric field. For this purpose, we added into our simulation a conical structure before the main target to investigate its effects. The second section deals with the results of our simulations and their interpretation, while in the last part we draw the conclusions regarding this study.

Chapter 4, named "*Target curvature influence on particle beam characteristics resulted from laser ion acceleration with microstructured enhanced targets at ultra-high intensity*", continues the studies performed in Chapter 3 on structured targets. The first subchapter presents the simulation parameters, which are intended to determine how effective the manipulation of target curvature is in determining the beam collimation and maximum ion energies. The chapter continues with the presentation of the obtained results and their interpretation, culminating with the conclusions drawn from this study.

The work done in **Chapter 5**, named "*Laser ion acceleration and high energy radiation generation from near-critical gas jets*", focuses on the effects resulted from the manipulation of the density of a gaseous Xe target in interaction with a high intensity ultra-short laser pulse in order to prepare first ultra-high intensity experiments on facilities like BELLA, CETAL, APOLLON and the ELI high power lasers. Similar to the structure of the last chapter, it starts with presenting the study parameters. We want to ascertain if the spectrum features can be controlled by changing the peak density of the gas jet when using ultra high intensity laser pulses, in correlation with the results for lower intensity pulses in the literature. In this study we have the pulse interacting, at normal incidence, with the target composed of Xenon ions and electrons with an increasingly higher maximum

density. The gas target has a \cos^2 density profile with a 50 microns FWHM in the x direction and uniform in the y direction. The last two sub-chapters are dedicated to interpreting the results obtained through numerical modeling and the drawing of conclusions on the study.

The last chapter of this work, **Chapter 6**, contains the final conclusions that were drawn from the studies presented within the thesis.

The thesis concludes with three sections: References, Acknowledgements and Annexes. The **References** section contains the relevant papers, books and various sources that made it possible to complete the studies performed throughout this work. The funding that permitted me to accomplish my studies is presented in the **Acknowledgements** section. The last section, **Annexes**, lists some of the contributions that have been added to the PICLS code.

Chapter 1

Laser plasma acceleration mechanisms

Ions are accelerated by different physical processes in the laser-target interaction, processes that depend on their position in the target. The shared common feature of these mechanisms is that the ions are accelerated by intense electric fields, occurring because of the strong charge separation induced by the interaction of the laser pulse with the target, directly or indirectly.

We can identify two distinct main sources for charge displacement. One is the charge gradient caused by the direct action of the laser ponderomotive force on the electrons in the front surface of the target, which is the premise for the Radiation Pressure Acceleration (RPA) process [9-11].

The second source can be pinpointed as coming from the laser radiation being converted into kinetic energy of a relativistically hot (~few MeV) electron population. The hot electrons move and recirculate through the target, forming a cloud of relativistic electrons around the target, in the vacuum. The cloud extends for several Debye lengths, creating an extremely intense longitudinal electric field, mostly directed along the surface normal, which, consequently, is the cause of the efficient ion acceleration [12], [13] that leads to the Target Normal Sheath Acceleration (TNSA) process [14].

1.1. Target Normal Sheath Acceleration

A distinctive feature of the TNSA process is that ions are accelerated in directions perpendicular to the target surface, with a very good beam collimation. Usually, the most efficient acceleration mechanisms occur on the rear side of the target, producing ions accelerated to energies greater than the laser ponderomotive force F_p (for a laser intensity of $I = 10^{20} \frac{W}{cm^2}$ the ponderomotive potential is $F_p = 3.9 MeV$).

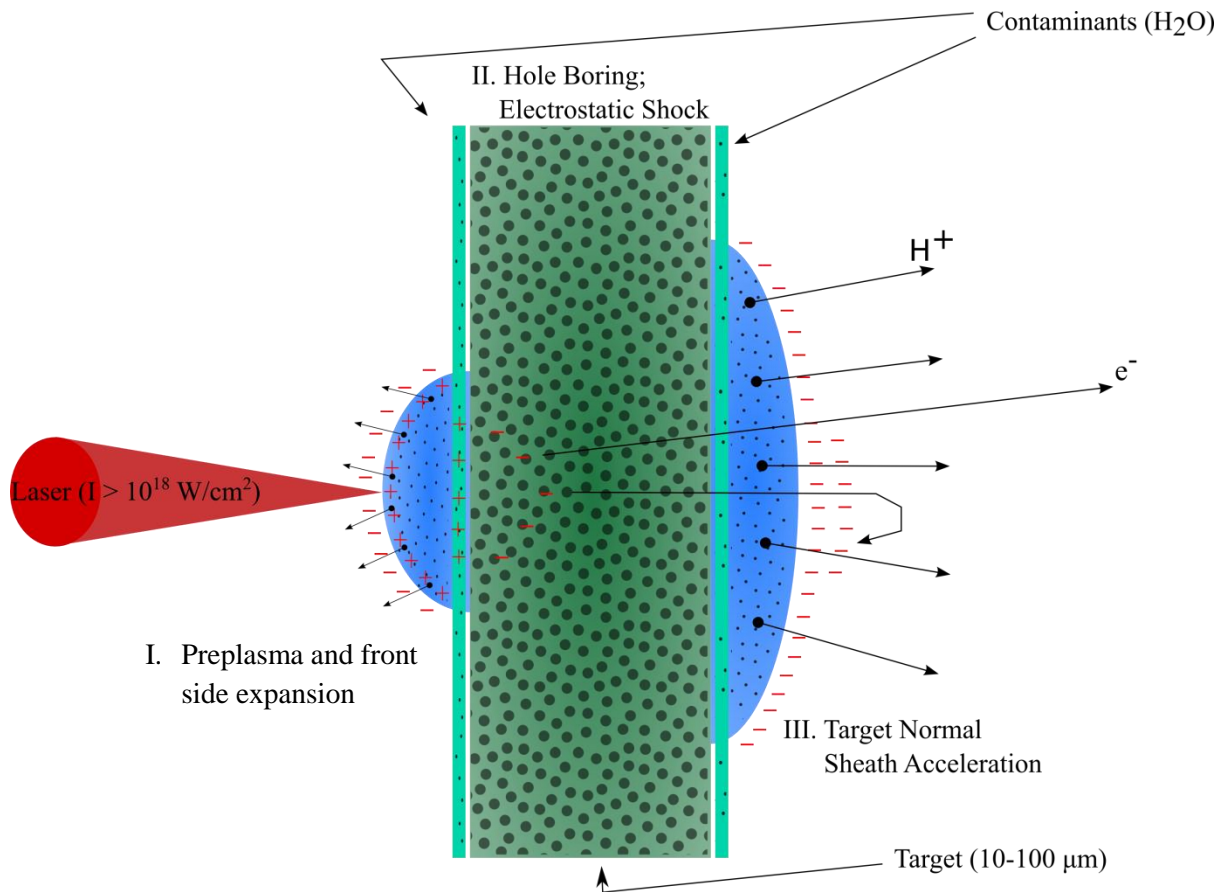


Figure 1. Target Normal Sheath Acceleration schematic overview. Zone I: The preplasma generated by the laser prepulse on the target front side; The main pulse interacts with this plasma and accelerates electrons mainly in the forward direction. Zone II: Electrons recirculate through the target, and due to the collisions with the target material their divergence increases. Zone III: Electrons leave the target, creating a dense sheath. The electric field generated by the charge separation then accelerates the heavier ions.

The rear surface electric field will depend on the electron distribution parameters, such as the divergence, temperature, number, as well as on the parameters of the surface itself (target density profile). The possibility of reaching TNSA also on the front surface of the target has been demonstrated by Ceccotti et al. [15] in an experiment by using laser pulses with ultra-high contrast which leave the surface almost unperturbed. The laser-plasma interaction process for a solid target is illustrated in Figure 1. The particular segments of the laser-plasma acceleration can be pinpointed with respect to their localization. The main pulse touches the plasma and electrons will be accelerated in Zone I, from the preplasma generated by the laser prepulse on the target front side to the critical density surface, for the most part, in a forward direction. Within the target the electrons will collide with the target material and therefore their divergence will increase (Zone II). Electrons leave the target, creating a dense sheath (Zone III). The electric field generated by the charge separation then accelerates the heavier ions.

1.1.1. Electron component

Depending on the laser intensity, the laser contrast, the laser incidence angle and the target density, collisionless heating of electrons by laser radiation takes place via several heating mechanisms such as Brunel absorption (vacuum heating) [110], resonance heating [111], [112], anomalous skin effect [113], [114], sheath inverse bremsstrahlung absorption [115], relativistic $\mathbf{j} \times \mathbf{B}$ heating [16], [119] and stochastic heating by counter propagating electromagnetic waves [116-118]. For laser intensities higher than $10^{18} \frac{W}{cm^2}$ and solid targets, the dominant absorption mechanism is the $\mathbf{j} \times \mathbf{B}$ mechanism [16]. Existing laser ion acceleration mechanisms are based on the electrons excited by the laser pulse and their resulting electric field determined by the charge separation. Calculations done with Particle-In-Cell simulation codes [16-18] have shown that the hot electron component has a logarithmic slope that estimates the ponderomotive potential of the laser beam. In the relativistic regime, the kinetic energy of an electron oscillating in the electromagnetic field of the laser, averaged over the laser cycles represents this estimation [19]:

$$T_{hot} \approx U_{ponderomotive} \approx 1[MeV] \times \left(\frac{I\lambda^2}{10^{19}} \right)^{\frac{1}{2}} \left[\frac{W \cdot \mu m^2}{cm^2} \right] \quad (1)$$

where λ is laser wavelength.

Due to the fact that the relativistic electrons are mainly directed inward [20], the one-dimensional Maxwell-Jüttner distribution can be used to simplify the distribution function of the particles. This simplification will lead to a profile close to a normal Boltzmann distribution.

The process of converting the laser energy into hot electrons is a mechanism whose effectiveness is far from perfect. Therefore, only part, η , of the energy will be converted into energetic electrons. The total number of hot electrons is given by:

$$n_0 = \frac{\eta E_L}{c\tau_L \pi r_0^2 k_B T_{hot}} \quad (2)$$

where:

- E_L is the laser energy;
- c is the speed of light;
- τ_L is the pulse duration;
- r_0 is the laser spot radius.

The conversion efficiency is highly dependent on the preplasma conditions. It can reach values as high as 50% and has a scaling with intensity as follows [21]:

$$\eta = 1.2 \times 10^{-15} I^{0.74} \left[\frac{W}{cm^2} \right] \quad (3)$$

At ultra-high intensities, the conversion efficiency can be as high as 60% when the laser pulse is perpendicular to the target and up to 90% when angles smaller than 45° are used for irradiation [22].

When considering the intensities of state-of-the-art short-pulse lasers, a considerable number of hot electrons are produced and pushed through the target. One can estimate that at least a part of the electrons created $\left(N = \frac{\eta E_L}{k_B T_{hot}} \right)$, are in the MeV range.

An ablation plasma creates an inward-travelling shockwave that heats, ionizes, and compresses the target. Fast electrons are created by the laser, propagating into the dense plasma towards the target's rear side. The high electron current j_{fast} can lead to filamentation and magnetic field generation (shown by the light red- and blue-colored areas), as well as driving a return current j_{ret} . The global magnetic field tends to pinch the fast-electron current. Electrons propagating in the dense solid matter interact with the background material by binary collisions. This leads to a spatial broadening of the electron distribution, which becomes the major effect for longer distances. At the rear side, the electrons form a sheath and build up an electrostatic field E_z (grey line in graph). This can lead to refluxing (recirculation) of the electrons, heating the target even further. (Figure taken from [26])

Further studies are required to determine the process by which the electrons pass through a target. As we can gather from Figure 2, the front surface (of n_c critical density, where $n_c = \epsilon_0 m_e \omega_0^2 / e^2$ is the critical density of the laser at the specified wavelength) is pushed by the laser, resulting in a sharp density profile for the electrons. This plasma motion sends a shockwave into the target, ionizing it, thus changing the target electrical conductivity. After penetrating the cold solid target, we can no longer neglect the binary collisions, which have a spatial broadening effect on the electron distribution, counterbalancing the magnetic field effect [27]. For thick targets (greater than $15 \mu m$) binary collisions are the main spatial broadening mechanism [28].

For a target thickness above $15 \mu m$, one can estimate the electron beam divergence by assuming that the hot electrons are created in an area proportional to the size of the laser focus. Afterwards, the electrons are transported to the back side of the target purely collisionally (this presumption is in agreement with most of the published information). An analytical description of the broadening distribution generated by multiple Coulomb collisions is given by Bethe, using Molière's theory [29], namely, the angular distribution, $f(\theta)$, follows a Gaussian profile:

$$f(\theta) = \frac{2e^{-\theta^2}}{\chi_c^2 B} \sqrt{\frac{\theta}{\sin \theta}} \quad (4)$$

with the second term of the right-hand side being a large angle correction [29]. The ϑ angle depends on θ with $\vartheta = \theta / \chi_c B^{1/2}$. B can be determined from:

$$B - \ln B = \ln \left(\frac{\chi_c^2}{\chi_a^2} \right) \quad (5)$$

with:

- χ_a^2 , being the screening angle, deduced as $\chi_a^2 = 1.167(1.13 + 3.76\alpha^2) \lambda^2 / a^2$;
- $\lambda = \hbar / p$ (the de Broglie wavelength of an electron);
- $a = 0.885 a_B Z^{-1/3}$ (a_B is the Bohr radius and Z is the nuclear charge);
- α is given by $\alpha = Ze^2 / (4\pi\epsilon_0 \hbar \beta c)$ and $\beta = v/c$;
- e being the electron charge;
- ϵ_0 , \hbar , and c denote the absolute dielectric permittivity, the Planck constant and the speed of light, respectively.

The χ_c variable is equal to:

$$\chi_c^2 = \frac{e^4}{4\pi\epsilon_0^2 c^2} \frac{Z(Z+1)Nd}{\beta^2 p^2} \quad (6)$$

with:

- electron momentum p ;
- material thickness d ;
- number of scattering atoms $N = N_A \rho / A$;
- material density ρ ;
- mass number A ;
- Avogadro's number N_A .

From this, we can gather that χ_c is proportional to the target thickness and density as $\chi_c \propto \sqrt{\rho d}$, which means that the angular distribution of the electrons that are transported through the target is proportional to both the target density and its thickness. Using these

analytical formulae, one can make an estimation of the angular dispersion of laser-accelerated electrons (hot electrons) that are transported through cold solid materials.

The small-angle scattering electron distribution broadening can also be used to analyze proton beam profiles. Although this model appears to give a good estimation of the angular distribution of forward-propagating fast-electrons generated by laser-plasma interaction, it may not always give an accurate assessment of the electrons that reach the back part of the target. Davies [30] showed that, beside the production of the electromagnetic field, the electron recirculation must be taken into account, which turns calculations and estimations into very difficult tasks. This has been demonstrated to be true for targets below $20\mu m$ in thickness [31], but for thicker targets the number of electrons is overestimated when assuming there is a strong recirculation. To sum it up, it is still not clear if electromagnetic fields and recirculation are necessary for the determination of the hot electron transport through cold solid targets, but using a simple collision model gives a rather good estimation.

1.1.2. TNSA main mechanism

The majority of the electrons created by the laser pulse are transported through the target to the back side. The scattering resulted from simple collisions leads to a transversal extension, which can be approximated by:

$$r_{sheath} = r_0 + d \tan\left(\frac{\theta}{2}\right) \quad (7)$$

where:

- r_0 is the transversal size of the electromagnetic pulse in focus;
- d is the target thickness;
- θ is the broadening angle of the electron distribution estimated in the previous section (Equation (4)).

The energy distribution of the electrons has an exponential profile as follows:

$$n_{hot}(E) = n_0 \exp\left(-\frac{E}{k_B T_{hot}}\right) \quad (8)$$

with $k_B T$ being the temperature, and n_0 the overall density. Thus, we can estimate (not taking into account recirculation) the electron density on the rear region as:

$$n_{e,0} = \frac{\eta E_L}{c\tau_L\pi(r_0 + d \tan \theta)^2 k_B T_{hot}} \quad (9)$$

By inserting $E_0 = \sqrt{2I_0/\epsilon_0 c} \approx 2.7 \times 10^{12} V/m$ and by using equations (2) and (3), coupled with a ponderomotive scaling electron temperature notation like:

$$k_B T_{hot} = m_0 c^2 \left(\sqrt{1 + \frac{I_0 \left[\frac{W}{cm^2} \right] \lambda_L^2 [\mu m^2]}{1.37 \times 10^{18}} - 1} \right) \quad (10)$$

we can obtain an approximation for equation (9) as follows:

$$n_{e,0} \approx 1.5 \times 10^{19} \frac{r_0^2}{\left(r_0 + d \tan \frac{\theta}{2} \right)^2} \frac{\left(\frac{I}{10^{18} \frac{W}{cm^2}} \right)^{7/4}}{\sqrt{1 + 0.731 \frac{I}{10^{18} \frac{W}{cm^2}} \lambda_{\mu m}^2 - 1}} [cm^{-3}] \quad (11)$$

From this approximation, we can extrapolate that the density of the electrons that exit the target in the forward direction is proportional to the laser intensity, I , and with $\frac{1}{a^2}$. By applying these equations to a laser pulse intensity of $I = 10^{19} W/cm^2$, with a focal spot of $r_0 = 10 \mu m$ and a target thickness of $20 \mu m$, we obtain, according to equation (4), an angular expansion of $\theta = 42^\circ$ for the electrons that have the mean energy of $k_B T$. Using the approximation (11), we obtain an electron density at the rear region of $n_{e,0} = 1.4 \times 10^{20} cm^{-3}$, which supports the assumption of shielded transport through the cold solid target, being several orders of magnitude below the density of a solid.

After exiting the target, the electrons travel through a vacuum region. According to Poisson's equation, this charge separation gives rise to an electric potential Φ in the vacuum region. This can be written in one dimension as:

$$\epsilon_0 \frac{\partial^2 \Phi}{\partial z^2} = en_e \quad (12)$$

To solve this, a few assumptions have to be made: the solid matter in half the space, where z is 0 or below, compensates perfectly for the electric potential, while for $z \rightarrow \infty$, the potential also goes to infinity. For the vacuum region, the field can be calculated analytically [32]. The electron cloud density is as follows:

$$n_e = n_{e,0} \exp\left(\frac{e\Phi}{k_B T_{hot}}\right) \quad (13)$$

with the initial density for the electrons approximated with equation (11). The solution is achieved by using the assumption that $\frac{e\Phi}{k_B T_{hot}} = -2\ln(\lambda z + 1)$. The potential then becomes:

$$\Phi(z) = -\frac{2k_B T_{hot}}{e} \ln\left(1 + \frac{z}{\sqrt{2}\lambda_D}\right) \quad (14)$$

which in turn yields the corresponding electric field:

$$E(z) = \frac{2k_B T_{hot}}{e} \frac{1}{z + \sqrt{2}\lambda_D} \quad (15)$$

where λ_D is the electron Debye length:

$$\lambda_D = \left(\frac{\epsilon_0 k_B T_{hot}}{e^2 n_{e,0}}\right)^{1/2} \quad (16)$$

and represents the area where most of the charge separation takes place [33]. By substituting equations (10) and (11), we obtain:

$$\lambda_D \approx 1.37\mu m \frac{r_0 + d \tan\frac{\theta}{2} \sqrt{1 + 0.73\lambda^2 \frac{I}{10^{18}W/cm^2} - 1}}{r_0 \left(\frac{I}{10^{18}W/cm^2}\right)^{7/8}} \quad (17)$$

The Debye length (longitudinal sheath extension) scales with the square of the target width ($d \tan\frac{\theta}{2} \propto d^2$) and is in inverse proportion to the intensity of the laser pulse. This means that having a higher laser intensity will produce a shorter sheath extension at the rear side and, in turn, a stronger electric field. For the pulse and target parameters used previously we obtain a Debye length of $\lambda_D = 0.6\mu m$.

The electric field is at its maximum when $z = 0$:

$$E_{max}(z = 0) = \frac{\sqrt{2}k_B T_{hot}}{e\lambda_D} \quad (18)$$

$$E_{max}(z = 0) \approx 5.2 \times 10^{11} V/m \frac{r_0}{r_0 + d \tan\frac{\theta}{2}} \left(\frac{I}{10^{18} \frac{W}{cm^2}}\right)^{7/8} \quad (19)$$

$$E_{max}(z = 0) \approx 9 \times 10^{10} V/m \frac{r_0}{r_0 + d \tan\frac{\theta}{2}} E_{12} E_{12}^{3/4} \quad (20)$$

From this, we can see that initially, at $z = 0$, $E \propto I$ and $E \propto E_{12}^{7/4}$ (the electric field strength, E_{12} , from equation (20) is in units of 10^{12} V/m). For times greater than the initial moment, the strength of the field is governed by the ionizations and ion accelerations that occur on the posterior side of the target.

Since this electric field is a few orders of magnitude above the atom ionization threshold, it leads to instant ionizations in the target rear region [34]. The laser external electric field overlaps the atoms Coulomb potential and after the field exceeds the binding energy of the electron the ionization of the atoms occurs due to the freeing of the electron. The dependence of the threshold electric field strength, E_{ion} , to the binding energy, U_{bind} , is:

$$E_{ion} = \frac{\pi \epsilon_0 U_{bind}^2}{e^3 Z} \quad (21)$$

As the rear side electron sheath is relatively dense, one could make the argument that the atoms can be ionized through collision. Despite this, Hegelich [35], showed that the collisional cross-section in the collisional area is far smaller than the field ionization cross-section at the surface of the target. Thus, the majority of atoms present at the posterior side of the target are instantly ionized, and then, due to the electric field, are accelerated. In experiments, an estimation for the maximum charge state is performed using the maximum field strength that appears in the setup. The sheath peak electric value [35] and the transverse field extension [36], [37] have been previously estimated in this manner.

Not all the electrons are trapped by this electric field. Lower energy electrons are also stopped and re-accelerated into the target. The time scale on which these phenomena occur is of just a couple of femtoseconds, due to the electron velocity being comparable to the speed of light and the distances discussed being of the micrometer order. By factoring this in, we can conclude that electrons will always be found at the posterior side of the target. The created electric field is quasi-static, in the order of the ion acceleration time. This field is directed normal to the target posterior surface, giving the accelerated ions a normal direction with respect to the target rear surface, hence the name of the mechanism, Target Normal Sheath Acceleration.

1.1.3. Characteristics of the ion beam

The reasons of the comprehensive research in laser-accelerated ions are the remarkable properties arisen from using these kinds of laser intensities, namely high brightness, high directionality and laminarity and short pulse duration. Having these particularities in mind, the produced ion beams can be used in various applications in science, technology and medicine. In the following, the main parameters of the ion beams will be discussed.

1.1.3.1. Particle count

A most useful feature of the TNSA ion beams is the high number of particles that are accelerated in the forward direction. Presently, the particle counts for protons with energies above 4 MeV, detected in experiments, have been up to 6×10^{16} , which means that the general conversion efficiency from laser to ion beam energy is about 9%. This can become an issue when considering that the target is of finite size, having a limited number of protons in the contamination layer, thus it can deplete. Allen et al. [38] determined that on the back surface of an Au foil, in a $1.2 \times 10^{-4} \mu\text{m}$ thick layer, there are $2.24 \times 10^{23} \text{ atoms}/\text{cm}^3$. It has been shown experimentally [39] that using a coating for the back surface of a metal can supply enough protons, up to a thickness of $\approx 100\text{nm}$, after which, due to limited electrical conductivity, it may cause instabilities in the electron propagation.

1.1.3.2. Energy range

The usual distribution of the ion beam energy, based on the mechanism previously described, has an exponential profile, with a cut-off depending on the hot electron temperature. The acceleration process occurs in the order of charge to mass ratio, particles with a high ratio being the first to be accelerated, unless some special target manipulation is performed. The presence of these protons is owed to the limited vacuum achievable, thus water vapors and hydrocarbon contaminants are still present on the target surface, and are exposed to the strongest electromagnetic field gradients. The contamination layer thickness has a high impact on the screening of the electric field for protons and ions situated further in the depth of the target, thus creating a broader energy distribution with the increase in

thickness. Also, the presence of an inhomogeneous electron distribution drives an inhomogeneous acceleration field in the transverse directions. The primary drawback of laser ion acceleration is comprised of this inhomogeneous ion energy range.

To date, only three groups [40-42] have obtained a quasi-monoenergetic beam with an energy spread $\leq 20\%$, using mainly the TNSA mechanism. Hegelich *et al.* [40] experimented with heated palladium foils, $20 \mu\text{m}$ thick. The target heating ($T \sim 600 \text{ K}$) meant that the surfaces were completely dehydrogenised, leaving only carbon atoms on the target surfaces. Further increasing the temperature ($T > 1100 \text{ K}$), the remaining carbon had a phase transition, forming a monolayer of graphite on the palladium surface. From this layer, C^{5+} ions were accelerated to $3 \text{ MeV}/u$ with an energy dispersion of 17%. This procedure offers both advantages and drawbacks. Even if the resistive heating removes all the hydrogen component, it requires extremely precise temperature measurements and the graphene formation cannot be controlled.

Schwoerer *et al.* [41] used titanium foils of $5 \mu\text{m}$ in width, which were coated with hydrogen-rich polymethylmethacrylate microdots of $20 \mu\text{m} \times 20 \mu\text{m}$ on the posterior surface of the foil. In this case, the accelerated protons had a quasi-monoenergetic spectrum with a peak at 1.2 MeV .

Ter-Avetisyan *et al.* [42] used the interaction of a high-intensity, high-contrast laser pulse and a water droplet of limited mass to produce quasi-monoenergetic deuteron blasts. They reported an energy dispersion of 20% for a peak position of 2 MeV in the spectrum. The major drawback of this experiment was low probability of laser-droplet interaction.

1.1.3.3. Opening angle

The most energetic protons are emitted under opening angles, $\leq 5^\circ$ half angle, then, with the drop in energy, the angle increases. This happens for the cases that are below 30% maximum energy, at which point the angle remains constant, even for lower energies. The angle increases mainly parabolically with the decrease in energy, even though this pattern may sometimes be linear (Figure 3).

The opening angle slope profile is a result of the hot electron initial distribution at the target surface [43]. According to Carroll *et al.* [43], a transverse dependent Gaussian sheath will result in a greatly curved opening angle profile, while a hot electron sheath with a parabolic profile will give a linear dependency. On the other hand, the precise modeling of the acceleration process is not described fully in [43]. The experimental results are better explained by the more detailed model presented in [44]. Another important aspect to note is that opening angle is not the same as beam divergence. The opening angle is measured from the point where the source emits its maximum output (the center) to the point where the source emits 50% of its output whereas the beam divergence is a measure of how fast the laser beam expands far from its focus. The proton beam divergence slightly increases along with the increase in energy, while the source size decreases with proton energy [45], [46].

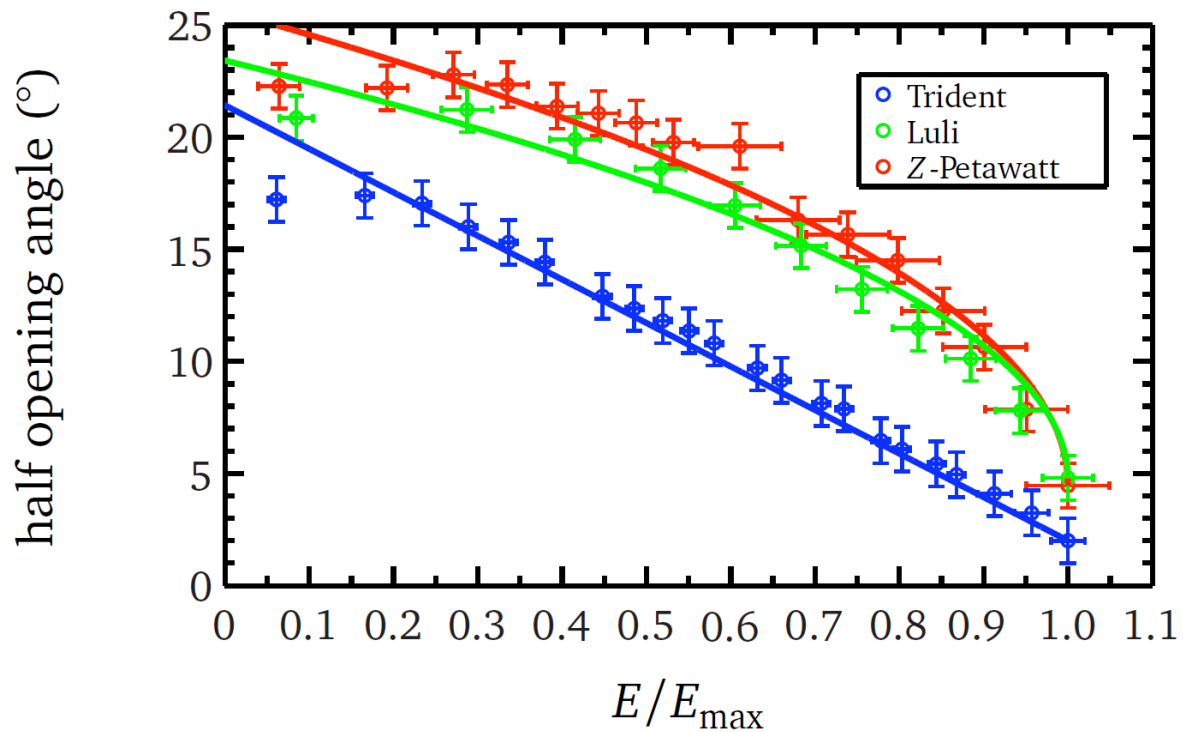


Figure 3. Half opening angle effect on the particle energy. Trident data (blue circles), LULI-100 TW (green circles), and Z-Petawatt (red circles). The plots are normalized to the beam maximum energy of each respective facility. Once the energy increases, the opening angle decreases. Data from the LULI and Z-Petawatt experiments show a

parabolic dependency while the Trident experimental results display a linear slope.
(figure taken from [24])

1.2. Laser Radiation Pressure Acceleration

The Radiation Pressure Acceleration regime (RPA) was introduced through theoretical and numerical studies by Wilks et al. [47] and Denavit et al. [48], being first referred to as the hole-boring (HB) scheme (this acceleration scheme can also be referred to as the laser piston regime). This process occurs in thick targets inside which it can produce strong electrostatic shocks [49] as it accelerates directly the ions found at the critical density interface where the laser pulse is stopped [50]. The laser ponderomotive force pushes the electrons at the front side of the target, leading to a high amplitude electrostatic field that is created due to the charge separation. As such, during the duration of the laser pulse, ions located on the front surface of the target are accelerated to high energies.

An analytical approximation of the maximum energy for ions accelerated in the forward direction can be performed. This ion maximum velocity, for the particles inside the target, can be calculated as two times the surface velocity of the receding plasma [48],[51]. In the case where we have a maximum efficiency of the regime, which means the laser is totally reflected at the critical interface, the velocity of the receding plasma is given by [47],[17]:

$$\frac{u_s}{c} = \sqrt{\frac{1}{2} \frac{n_c}{n_e} \frac{Z m_e}{M_i} a_0^2} \quad (22)$$

where:

- n_c is the critical density at the laser reflection (at normal incidence $n_e = \gamma n_c$ [52]);
- M_i is the ion mass;
- m_e is the electron mass;
- $\gamma = \sqrt{1 + a_0^2}$ is the Lorentz factor;

- $a_0^2 = \left(\frac{p_{osc}}{mc}\right)^2 = \frac{I\lambda^2}{1.37 \cdot 10^{18}}$;
- I is the laser intensity;
- λ the laser wavelength in microns.

From this we get the maximum energy of the forward accelerated ions:

$$E_{front} = 2 \cdot M_i \cdot u_s^2 = \frac{Zm_e c^2 a_0^2}{\gamma} \quad (22)$$

In the case when a circularly polarized laser pulse is used, electrons are pushed by a strong electrostatic field created at the front of the target. The key difference is that the electrons are not heated. Instead an electron layer is created within the target, that travels along it. This regime was studied in a number of theoretical and numerical studies [10], [53-57] and also in experimental studies [58]. This regime was also observed on higher wavelengths lasers at the interaction with gas jets [59], [60].

1.3. Other related acceleration schemes

When using near-critical density, partially expanded targets [61], [62], one can observe the occurrence of the Magnetic Vortex Acceleration mechanism (MVA). This mechanism relies on the quasistatic magnetic field generated by the fast electron currents in the vicinity of the rear target surface which, in turn, are generated by the propagation of the laser light through the expanded target. It has been proven that this quasistatic magnetic field generates an inductive electric field at the rear side of the target which augments the TNSA ion acceleration [63-66].

The Collisional Shock Acceleration (CSA) is another acceleration scheme first introduced for overdense targets [48], [49]. This mechanism relies upon the generation of a shock wave in the target with the laser pulse as its source, which reflects ions inside the target, thus accelerating them to high energies.

This method was also extended to underdense targets [67]. Compared to solid targets where we have limited laser absorption to the target surface, the laser pulse inside low density targets heats electrons on a large volume which leads to a higher laser

absorption overall. This acceleration regime is also advantageous for several applications because of the reduced debris produced. Another advantage of such targets is the adaptability to high repetition rate lasers.

A typical problem for thin foils is the laser contrast, but in the case of near-critical targets this becomes less detrimental than in the case of solid targets, as gas jets do not absorb much laser energy for laser intensities below 10^{13} W/cm² for a one-micron wavelength laser. Ion acceleration produced from the interaction of a very high intensity laser with underdense targets has been studied with Particle-In-Cell (PIC) simulations [68-70], but the simulated targets did not reproduce the gas targets available for experiments.

The first experiments of ion acceleration via laser interaction with underdense targets showed radial acceleration [71]. Recent experiments proved that using high intensity lasers one can obtain strong longitudinal proton acceleration [72-73]. In this case the energy of the longitudinally accelerated protons is greater than the one of the transversally accelerated protons.

The accelerating mechanism that causes the energetic accelerated ions seen in [72-73] has not yet been described in detail and therefore is the center of an ongoing debate [63], [65]. In the case of near-critical gas targets, a steep density gradient is not easy to achieve experimentally (however, such experimental endeavors have been achieved in the past [74]), thus, the dependence of the particle acceleration on the specific plasma density is important in order to optimize such experimental efforts.

The studies explored for this work require the modeling of the regimes presented within this chapter using numerical simulations. The most widely used numerical tool that models these acceleration regimes is introduced in the following chapter.

Chapter 2

Basic introduction to the Particle-In-Cell method for laser-plasma interaction numerical modeling

When we talk about the classical or relativistic description of natural phenomena, we inherently think about the interaction between base elements through force fields. The same can be attributed to the definition of plasma, as an ensemble of charged particles that interact through electric and magnetic fields. In this case, we will have a combination of the electric (E) and magnetic (B) Lorentz force acting as the force (F_p) affecting the particles. So if we consider a particle p with its charge q_p , on the position x_p having a velocity v_p we have the following equation:

$$\vec{F}_p = q_p \vec{E}(x_p) + \vec{v}_p \times \vec{B}_p(x_p) \quad (23)$$

From a computational standpoint we can say that the force that is acting on our particle is computed from the electric and magnetic field calculated at the position of the particle. These electric and magnetic fields are generated by the particles present in the

plasma system and also by external sources (external magnetic fields or electrodes). The computation of the electric and magnetic field is done by solving Maxwell's equations:

$$\begin{aligned}
 \nabla \cdot \vec{E} &= \frac{\rho}{\epsilon_0} \\
 \nabla \times \vec{E} &= -\frac{\partial \vec{B}}{\partial t} \\
 \nabla \cdot \vec{B} &= 0 \\
 \nabla \times \vec{B} &= \mu_0 \vec{J} + \mu_0 \epsilon_0 \frac{\partial \vec{E}}{\partial t}
 \end{aligned}
 \tag{24}$$

where ρ is the charge density, ϵ_0 is the vacuum permittivity, μ_0 is the vacuum permeability and J is the total current density.

2.1. Interacting systems classification

A critical step in the successful usage of the particle-in-cell (PIC) method is the correct computation of the sources in Maxwell's equations. Using a broad approach, we can state that if we have a system comprised from particles of infinitesimal size, the sources of Maxwell's equations are the sum of individual particle contributions.

If we consider a system comprised of N_D charged particles situated in a square box with the side equal to the Debye length (λ_D) then the electric field in any point of the box can be determined by superimposing all the contributions of the individual particles. The Debye length is chosen for exemplification due to the plasma basic property of shielding localized charges over distances greater than the Debye length. This effect is exponential in nature and the canceling effect is not totally achieved over just one Debye length, but sufficient for a basic grasp of the phenomena.

Considering ideal conditions, having the configuration depicted in Figure 4, we have a collection of particles that move constantly, interact with each other and are agitated by their thermal motion. If we place a detector, inside this ideal box, for the local electric field, we would obtain a signal increase as a particle approaches the detector followed by a signal decrease as it moves away.

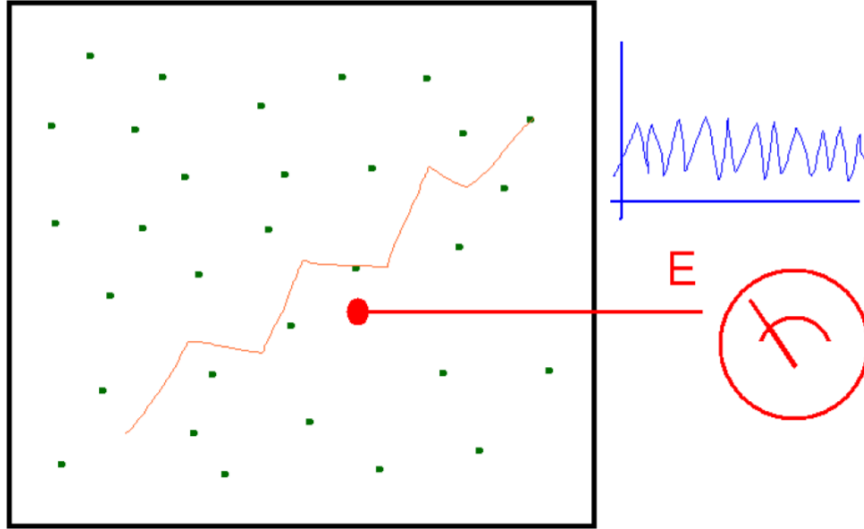


Figure 4. Strongly coupled system schematic [75]. E is the detector, and in blue we have the signal from the detector.

Statistically speaking, we have a low number of particles near the detector at any given time, but the specific position of these particles is very important in order to determine the value measured by the detector. Also, it is important to note that the effect of any particle on the signal received by the detector is strongly influenced by the distance of the particle to the detector probe, and, only when particles are in close proximity, we see a strong effect. Extrapolating this to the whole system, each of the contained particles detects the same kind of effect. The electric field that any given particle feels is the sum of all other particle contributions, but only when another particle is in close proximity, a significant increase in the electric field occurs. This event is labeled as a *collision*. As time passes, the particles in the box are affected by a series of such events that modify the particle trajectories. This kind of system is referred to as a *strongly coupled system* in the kinetic theory. The condition for this kind of system is that the number of particles present in the box is small.

On the other hand, we have the *weakly coupled system*. Its configuration can be seen in Figure 5. This kind of system is composed from a large number of particles, which, in turn, means that the number of particles that contribute to the electric field at any given time is very high. Another consequence of the high number of particles contributing to the electric field is that the measurements are smoother, and we do not have the same strong

jumps as in the case of the strongly coupled system. In the same manner, the particle trajectories are affected by a large number of collision events, and such they are smoother and without high jumps.

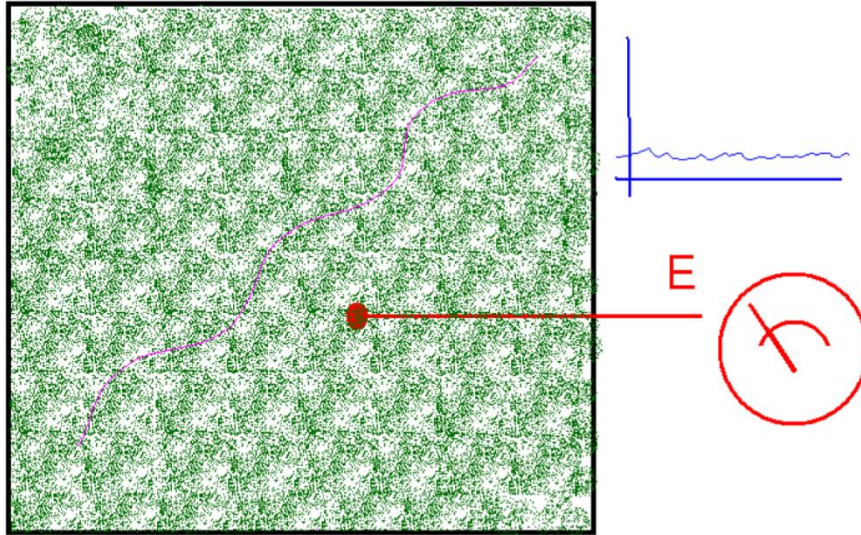


Figure 5. Schematic of a weakly coupled system [75]. E is the detector, and in blue we have the signal from the detector.

2.2. Interacting systems description

As previously stated, an important parameter in determining the kind of system we deal with is the number of particles present in the said system. For a conventional system with the size of the sides equal to the Debye length, we would have the number of particles:

$$N_D = n\lambda_D^3 \quad (25)$$

where n is the plasma density.

The classification of the systems can be done by the particle count, so we have a weakly coupled system when N_D is large, and a strongly coupled one when N_D is small. We can further elaborate on this model by taking into account the energies of the particles found in the system.

The particle distribution in the box is a random one, but we can associate an average volume to each particle. This volume would be the volume of the box divided by the number of particles found in the box.

$$V_p = \frac{\lambda_D^3}{N_D} = n^{-1} \quad (26)$$

Using this volume, we can find the average inter-particle distance, as a function of the plasma density:

$$a = \sqrt[3]{V_p} = n^{-1/3} \quad (27)$$

Going further, we can say that the electrostatic potential energy between two particles with charge q situated at a distance a from each other is:

$$E_{potential} = \frac{q^2}{4\pi\epsilon_0 a} \quad (28)$$

where ϵ_0 is the vacuum permittivity and the particle kinetic energy (from statistical physics) is:

$$E_{thermal} = kT \quad (29)$$

with k being the Boltzmann constant.

Another useful parameter in the evaluation of the coupling of plasmas is the ***plasma coupling parameter***:

$$\Lambda = \frac{E_{thermal}}{E_{potential}} = \frac{4\pi\epsilon_0 a kT}{q^2} \quad (30)$$

adding the Debye length definition and the value for a previously obtained, we get:

$$\begin{aligned} \lambda_D &= \left(\frac{\epsilon_0 kT}{ne^2} \right)^{1/2} \\ \Lambda &= \frac{4\pi\epsilon_0 kT}{q^2 n^{1/3}} = 4\pi N_D^{2/3} \end{aligned} \quad (31)$$

Having this new parameter, we can expand the previous considerations regarding the number of particles inside a Debye cube to include information regarding the energies. In the case when we have a large number of particles in the system (weakly coupled system), their thermal energy exceeds the potential energy, thus the particle trajectories have a low dependency on the inter-particle interactions. On the other hand, when the plasma coupling parameter is small, it means that the potential energy is greater than the thermal energy and we have a strong dependency of the particle trajectory on the inter-particle interaction (strongly coupled system).

2.3. Particle-Particle approach

In principle, one can run a computer simulation of an interacting particles system by simply tracking each particle present in the system. This particle-particle (PP) approach is done by updating Newton's equations for each of the N particles in the system, while having the combined effect of the component particles acting as the force influencing each individual particle (F_p).

The discretization of the evolution of the system is done in large numbers of temporal steps Δt , chosen in such a way that the particles only move a small distance between time steps. After each particle movement the force is recalculated and only after that a new move can be done. If we have the particle position x_p and the particle velocity v_p , then we can write the equation of motion as:

$$\begin{aligned} x_p^{new} &= x_p^{old} + \Delta t v_{old}^p \\ v_p^{new} &= v_p^{old} + \frac{\Delta t}{m} \end{aligned} \tag{32}$$

The major computational cost of this approach is the calculation of the force, which is the sum over all the particles present in the system. Considering $F_{pp'}$ the interaction force between two particles, p and p' , we obtain:

$$F_p = \sum_{p'} F_{pp'} \tag{33}$$

In the case of the electrostatic force, $F_{pp'}$ can be written as:

$$F_{pp'} = \frac{q_p q_{p'}}{4\pi\epsilon_0 |x_p - x_{p'}|^2} \cdot \frac{x_p - x_{p'}}{|x_p - x_{p'}|} \quad (34)$$

In practice, all forces are computed with the old values for the particle position, and once the force is calculated, then the new velocities can be obtained. After this, the new positions are calculated and this cycle is repeated until the end of the simulation. When looking at the force computations, given a number of N particles, for each particle we obtain $N-1$ terms and also taking into account that each pair of particles is only computed once, we end up with $N \frac{(N-1)}{2}$ force computations.

This method of simulation is suitable for strongly coupled systems where we have a low number of particles per Debye cube. The particle-particle method stands at the basis of the molecular dynamics method which is used in condensed matter and biomolecular studies [76]. This method is also used in the study of gravitational interactions, such as cosmological studies regarding the formation and distribution of galaxies.

When talking about weakly coupled system, where the number of particles is large, this method is not feasible. With the increase in particle number, the computational cost of the method increases quadratically (as N^2) making the computational effort to run this method for such systems unfeasible. For the case of weakly coupled systems, the goal is to have a method that reduces the description of each particle to a statistical sample of particles.

2.4. Finite-size particles

The most important aspect to successfully and efficiently simulate a weakly coupled system is that the model used needs to manage collective batches of particles instead of individual particles. One computational particle, referred to as a *superparticle* (or *macroparticle*), represents a group of particles and can be depicted as a reduced portion of the phase space. The schematic of this concept is presented in Figure 6.

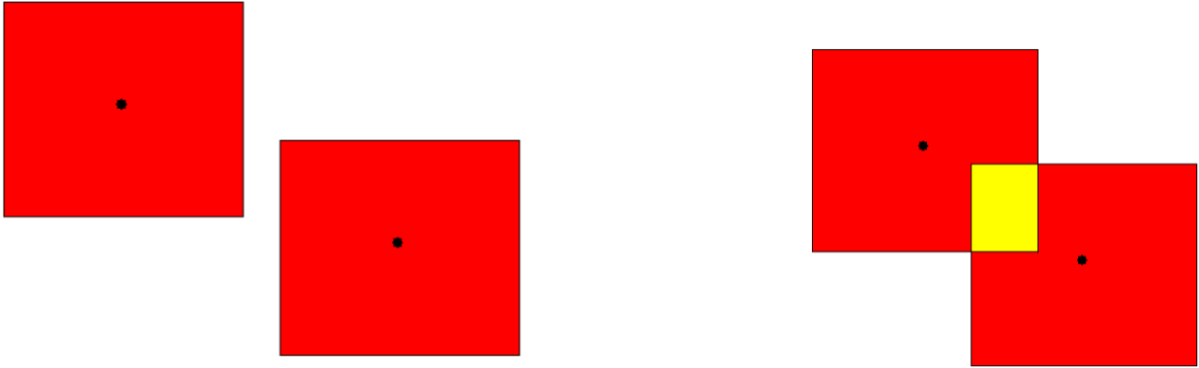


Figure 6. Finite size particle (also known as superparticle or macroparticle) schematic representation [75]; In red we have the full representation of the phase space, with the black dot in the middle as the point particle behaviour; In yellow we have the neutralized overlapped area.

The main advantage when using finite-size particles is that the superparticles interact more weakly than point particles because of their finite size. At the interaction of two point particles, via Coulombian force for this example, the repulsive or attractive force between them grows as the particles get closer together, reaching singularity at zero separation.

When we treat the interaction of finite-size particles, we have the same behavior as point particles until the surfaces of the superparticles begin overlapping. After the overlap happens, the area that is subjected to the overlapping is neutralized (yellow portion of represented in Figure 6), and it does not contribute to the inter-particle force. Once the distance between particles is zero, and the particles fully overlap, then the force becomes zero. This assumes the surface of the particles is identical.

In Figure 7 we can see the force between two charged particles of spherical form as a function of the distance between them. When the separation distance is high, the force is identical to the Coulomb force, but as the distance between them decreases and the particles begin to overlap, the force between them becomes weaker than the corresponding Coulomb force, and at full overlap it becomes zero.

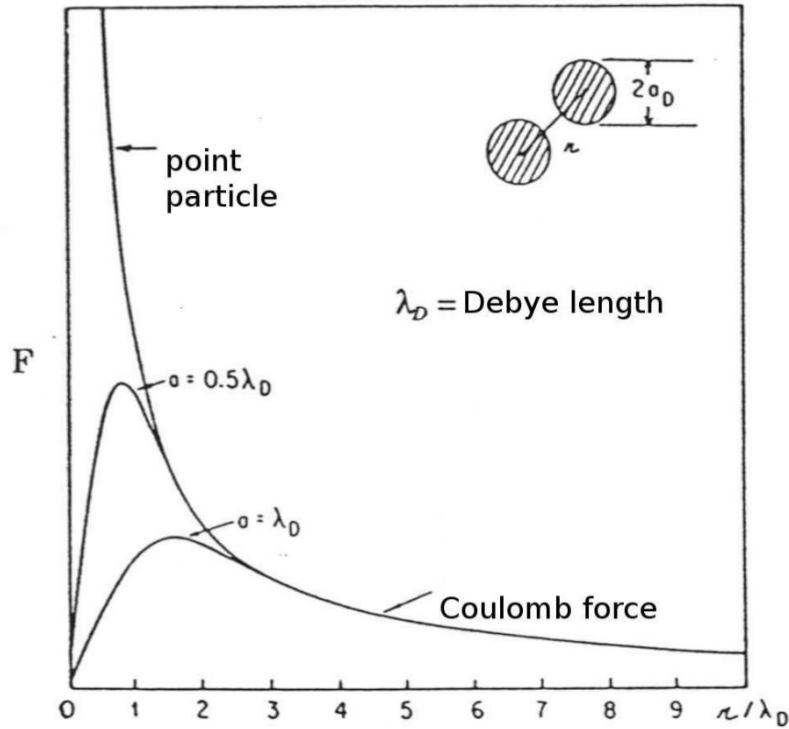


Figure 7. Interaction between two charged finite size particles [75]. Inter-particle force plotted for 3 different particle radii (point particle, $0.5\lambda_D$ and λ_D).

By using computational particles of finite size one can reduce the inter-particle interactions. Taking into account the definition of the plasma coupling parameter (equation (31)), using finite-size particles results in having lower potential energy for the same kinetic energy. This has the beneficial consequence that a correct plasma parameter can be achieved using less particles in the plasma system, thus recovering the realistic condition.

2.5. Particle-In-Cell method

In the Particle-In-Cell (PIC) method, we have the system represented by a smaller number of finite-size particles that, when the distance between them is greater than their respective overlap size, interact through the correct potential. At small distances, the reduced interaction potential is introduced, correcting the effect of the low number of particles. The method schematic is presented in Figure 8. This kind of treatment ensures that the electric field fluctuations in the system are smooth (blue graph in Figure 8), and correctly represented for a weakly coupled system. The reason behind this is that the effect

of the few particles, that are at distances less than the overlap distance, is weak. In a similar manner, we can extend the same reasoning to the particle trajectory. Hence, we have smooth trajectories, similar to what we would have in a real system, because the interactions between near neighbors are weak, and not because each particle is surrounded by a very large number of near neighbors. Furthermore, we can state that the collective effect is correct as long as the interactions at long range are being reproduced correctly as in the physical system.

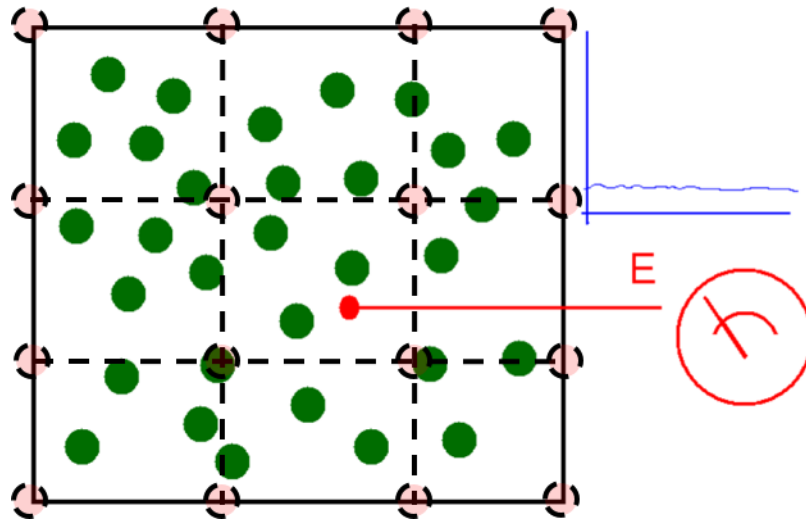


Figure 8. System composed from finite-size particles [75]. E is the detector, and in blue we have the signal from the detector. In dotted lines we have the grid discretization.

In the following we will consider an approach aimed at offering a clear mathematical link between the plasma mathematical model and its numerical solution. For the sake of clarity and simplicity, we will consider the 1D electrostatic and classical plasma. The extension to a 3D model requires a more complicated notation system, but it is not much more difficult. The motion of superparticles is determined in two steps within the PIC cycle. First step: employing Maxwell's equations the electromagnetic field can be calculated starting from the initial electrical currents and charge densities. The particles are then moved over a small distance by using this electromagnetic field in Newton's equation. At the second step the fields are also recalculated using the position and the charge density

determined here. This two-step cycle is being repeated for the whole period of the simulation.

In order to compute the fields a transition is made from the continuous space to a discrete spectrum. Therefore, the computational domain is divided into *cells* by lines that are parallel to the boundaries. From this grid discretization we can call the line intersections as *mesh points* or *grid points* (seen in Figure 8) and this is the origin of the method's name (Particle-In-Cell). The charge fields are being computed in these points, and the particle movement is being done relative to them.

The space coordinates are continuous for the particles and the particles can occupy any position within the cell. The local charge density is defined as the number of particles found in a cell divided by the volume of the cell in question. There are two main considerations to take into account when setting the resolution of the simulation (the size of the mesh cell). First, the length of the cell has to be less than the Debye length, in order to see the effects of charge density separation in the computation of the fields. On the other hand, we do not want the cell size to be smaller than the superparticle radius, due to the charge calculation [77].

2.5.1. Iteration cycle

As per usual numerical simulation, everything happens in time steps. In each time step there is a cycle of computations that are done in order to advance the system state. First the particle positions and velocities are read from memory, followed by a weighting due to the dependence of charge density calculation on the distance from the particle to the respective grid point. This is followed by an integration of the field equations and a weighting depending on how these fields computed in individual grid points affect each particle.

The basic cycle concludes with the integration of the motion equations in order to accordingly update the particle positions and velocities. For the first time step, before the basic cycle starts, the initial conditions of the system are read from an input file (the initial particle positions and velocities, the system density). The visual representation of a basic computational cycle can be seen in Figure 9.

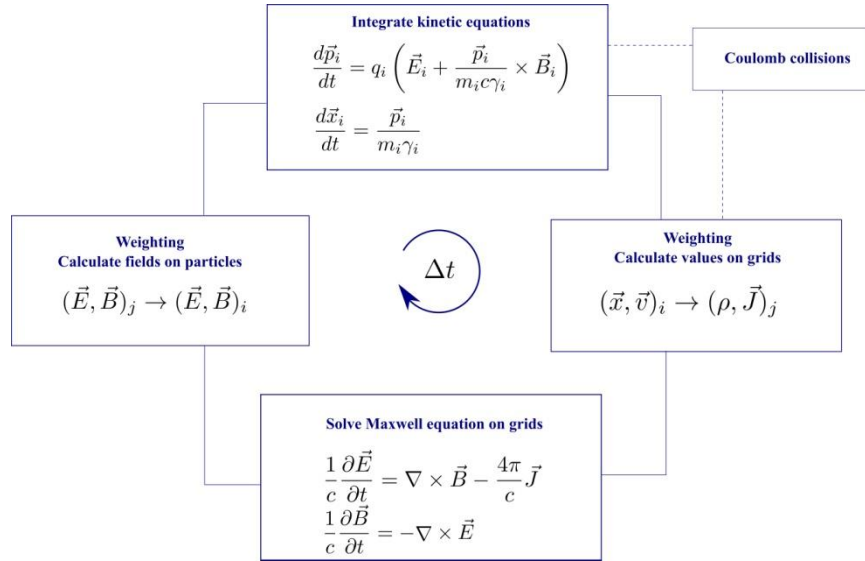


Figure 9. Basic computational cycle of a PIC code. Optional modules with dotted line.

The time advances each step by a value equal to Δt . The size of this parameter is chosen in respect to the physical phenomena that concern us. A shorter time step is needed when dealing with small mass particles, due to the higher plasma frequency, while, when having heavier particles, a longer time step can be used. If the purpose of the simulation is to study low frequency effects, a longer time step can be used, which in turn will also shorten the simulation time.

The number of integrations in such a simulation is also important because we have a large number of such computations in every cycle. For each particle in the system, we have two integrations per grid point, one for the equation of motion and another integration for the field. For example, for a simulation of a system with 10000 particles with 1000 time steps on 1000 grid points we will have 10^{11} integrations. This fact makes the choice of the numerical method used very important.

Computer memory is something else that has to be taken into account. The minimum information required to perform the integration is the particle coordinates and velocity. For the example given previously, this will amount to 20000 entries. If the method used is a high-order one (e.g., Runge-Kutta), then data from the previous time steps has to be saved, which not only increases the memory requirements, but also increases the number of operations done for each particle. This is the reason why it is crucial to save the

least amount of intermediary data coupled with the fastest method for the problem at hand. From the classic textbooks [77], [78] we can get a heuristic derivation based on the physical properties of a plasma.

2.5.2. Motion equations integration

A method used for computing these differential equations is called the leap-frog method, represented for a 1D case in Figure 10, and it replaces the two first order differential equations with two finite-difference equations. The leap-frog method is not error free, but this error is negligible if $\Delta t \rightarrow 0$. The leap-frog integrator is used in most PIC codes due to its simplicity (easy to understand and a minimal storage requirement) and good accuracy [77].

$$m \frac{d\vec{v}}{dt} = \vec{F} \Rightarrow m \frac{\vec{v}_{new} - \vec{v}_{old}}{\Delta t} = \vec{F}_{old} \quad (35)$$

$$\frac{d\vec{x}}{dt} = \vec{v} \Rightarrow \frac{\vec{x}_{new} - \vec{x}_{old}}{\Delta t} = \vec{v}_{new} \quad (36)$$

Because \vec{v}_{new} needed in eq. 35 comes from equation (36), the position step is calculated at a later time than the velocity step [42]. The simulation starts with the initial parameters for velocity and position at $t = 0$ given by the user in the input. Then the $\vec{v}(t = 0)$ is pushed back to $\vec{v}\left(-\frac{\Delta t}{2}\right)$ using the force \vec{F} calculated at $t = 0$.

The force \vec{F} has two components, one electric and the other magnetic.

$$\vec{F} = \vec{F}_{electric} + \vec{F}_{magnetic} = q\vec{E} + q(\vec{v} \times \vec{B}) \quad (37)$$

The electromagnetic fields have to be calculated at the particle coordinates, hence an interpolation from the grid to the particle has to be done for \vec{E} and \vec{B} .

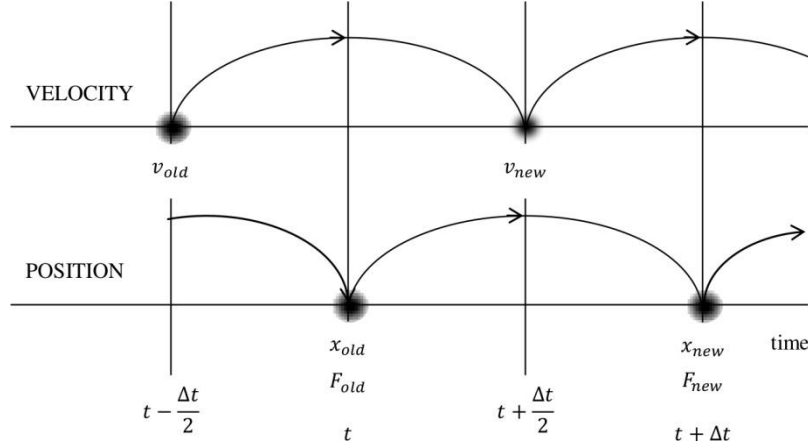


Figure 10. Leap-frog integration schematic (adapted from [77]).

Most modern Particle-In-Cell codes now use the Boris scheme [101] which is a time centered scheme for magnetic forces with an excellent long term accuracy.

2.5.3. Field equations integration

By solving Maxwell's equations, we use the initial densities for current and charge in order to obtain the electric and magnetic fields. If we assume a static case, we have:

$$\nabla \times \vec{E} = -\frac{\partial \vec{B}}{\partial t} \approx 0 \quad (38)$$

$$\vec{E} = -\nabla \Phi \quad (39)$$

$$\nabla \cdot \vec{E} = \frac{\rho}{\epsilon_0}$$

Combining these equations, we obtain Poisson's equation in terms of the scalar potential Φ :

$$\nabla^2 \Phi = -\frac{\rho}{\epsilon_0} \quad (40)$$

To continue, we can follow two approaches. The first involves solving the differential equations 39 and 40, getting:

$$E_j = \frac{\phi_{j-1} - \phi_{j+1}}{\Delta x} \quad (41)$$

$$\frac{\phi_{j-1} - 2\phi_j + \phi_{j+1}}{(\Delta x)^2} = -\frac{\rho_j}{\epsilon_0} \quad (42)$$

Equation 42 can be written in matrix form as follows:

$$A_\phi = -\frac{(\Delta x)^2}{\epsilon_0} \rho \quad (43)$$

Having all ρ_j values coupled with the imposed boundary conditions we will get as many equations as we have unknowns ϕ_j .

The second approach utilizes discrete Fourier series transformations for all the grid quantities. It is important to note, that this requires periodic boundary conditions to be applied in the simulation. Applying a Fourier transform on $\rho(\vec{x})$ and $\Phi(\vec{x})$ we obtain $\rho(\vec{k})$ and $\Phi(\vec{k})$, where \vec{k} is the wave vector of the Fourier transform kernel $\exp(-i(\vec{k}) \cdot \vec{x})$. Thus, by multiplying with $-\vec{k}^2$ in the second order derivate of Poisson's equation we obtain:

$$\Phi(k) = -\frac{\rho(k)}{\epsilon_0 k^2} \quad (44)$$

Within this finite Fourier series, $\rho(x)$ is known in the grid points positions. In the following we will denote the grid points with X_j , and the mesh function (either field, charge density or potential) with $F(X_j)$. The periodic condition for the grid function is $F(X_j) = F(X_j + L)$, where L is the overall length of the system in question. The Fourier transform becomes:

$$F(k) = \Delta x \sum_{j=0}^{NG-1} F(X_j) e^{-ikX_j}, \quad (45)$$

with NG being the total number of grid points. Then, we obtain the inverse Fourier transform as follows:

$$F(X_j) = \frac{1}{L} \sum_{n=-NG/2}^{NG/2-1} F(k) e^{ikX_j}, \quad (46)$$

Using this mathematical tool on eq. (40) and (41), we get:

$$E(k) = -ik\Phi(k) \quad (47)$$

$$\Phi(k) = \frac{\rho(k)}{\epsilon_0 K^2} \quad (48)$$

where [79]:

$$\kappa = k \left[\frac{\sin k \Delta x}{k \Delta x} \right] \text{ and } K^2 = k^2 \left[\frac{\sin k \Delta x / 2}{k \Delta x / 2} \right]^2$$

By reducing the Δx step size, κ approaches k and K^2 approaches k^2 . This means that using a finer grid we achieve more accurate results.

2.5.4. Weighting of particles and forces

Within the simulation the density and field computations are done on the grid points from the particle positions in relation to the grid, and the forces are computed at the particle positions from the closest grid point field. These kind of calculations are referred to as being called **weighting**, and it means an interpolation is done. The weighting can be of different orders, depending on the required accuracy. An important note to make is that the same order of weighting is done for both the density and the force calculations, otherwise self-force can occur, leading to particle self-acceleration.

For density computation using zero-order weighting, at a grid coordinate (index j), we perform a count of the number of particles (N_j) around the point of the grid within a radius of $\Delta x/2$ which is divided by the volume of the area taken into account. In a 1D case, this translates into counting particles in an interval $[X_j - \Delta x/2, X_j + \Delta x/2]$ and dividing this by Δx . The usual nomenclature for this kind of weighting is *nearest grid point* (NGP). For all the particles in the j^{th} cell, the electric field, used in the force calculations, is the one computed in the grid point X_j . This kind of interpolation is fast due to the singular grid look-up performed.

When a particle leaves the cell j into cell $j+1$, the density inside cell j drops by $1/\Delta x$

and rises inside cell $j+1$ by the same amount. Because of this density jump, the virtual shape of the particle is a rectangle (Figure 11). These density jumps at cell boundaries produce inconsistencies in electric field, and both occurrences produce numerical noise in the simulation that is for most plasma problems not tolerable.

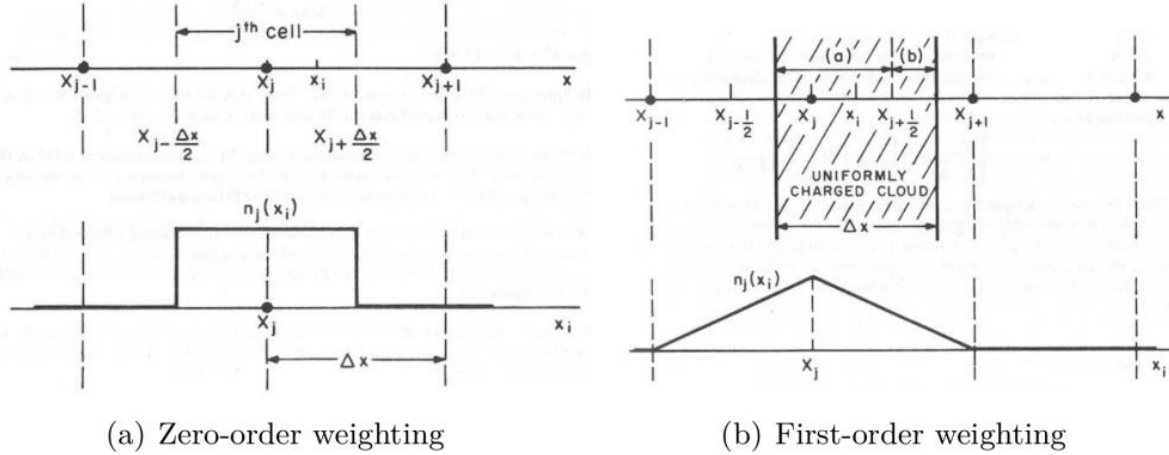


Figure 11. Zero and first order weighting and the virtual shape of the particles they produce (adapted from [77]).

The first order weighting produces smoother field and density fluctuations, reducing the noise generated, but it has the disadvantage of using more operations for the same job. This is done by accessing two grid coordinates for each particle, two times per timestep. This method considers that a particle is included in two cell densities (j and $j+1$) respectively to its position relative to X_j (and contributes to the cell charge density) as follows:

$$q_j = q_i \left(\frac{\Delta x - (x_i - X_j)}{\Delta x} \right) = q_i \left(\frac{X_{j+1} - x_i}{\Delta x} \right) \quad (49)$$

$$q_{j+1} = q_i \left(\frac{x_i - X_j}{\Delta x} \right) \quad (50)$$

where x_i and q_i are the position of the i^{th} particle, respectively its charge. This produces a triangularly shaped virtual particle (Figure 11). In order to suppress noise even more,

quadratic and cubic splines can be considered, but the computational cost of such methods is higher.

The forces and fields weighting is done using a similar approach. The zero order NGP force is imported from the field computed in the nearest grid points. The first order weighted force comes from linear interpolation equivalent to charge weighting as follows:

$$E(x_j) = \left(\frac{X_{j+1} - x_i}{\Delta x}\right) E_j + \left(\frac{x_i - X_j}{\Delta x}\right) E_{j+1} \quad (51)$$

Even if the first order weighting is more computationally heavy it can allow coarser grids and less particles than NGP with the same result [78].

2.6. Practical considerations when using the PIC method

2.6.1. Stability

When running a PIC simulation, the first step to be handled is the proper choice of time step and grid spacing. The time step needs to be set in order to resolve both the light-wave propagation, and also the Langmuir wave propagation, so we need:

$$c\Delta t < \Delta x \quad (52)$$

$$\omega_{pe}\Delta t < 2 \quad (53)$$

where ω_{pe} is the plasma frequency.

In a similar manner, the grid spacing needs to resolve the electron Debye length to avoid grid instabilities that might be caused by the different interpolations used, so we have:

$$\Delta x < \zeta\lambda_{De} \quad (54)$$

where ζ is a constant of order 1 which is chosen according to the interpolation type used. For example, for zero-order interpolations, we would have $\zeta \approx \pi$.

2.6.2. Energy conservation

The PIC method described previously is set to conserve the momentum to machine precision. This means that the energy will not be preserved exactly. This happens because the method uses a large number of particles per cell, and therefore we have infinite configurations for the same values that are recorded on the grid. This freedom in particle configuration within the cell leads to finite grid instability and the absence of exact energy conservation.

Explicit PIC codes (codes that follow the method described here) require safeguards in order to monitor the energy conservation from time step to time step. Furthermore, the time step and the grid spacing need to be chosen sufficiently small in order to conserve energy (satisfying just the stability constraints is not sufficient). Usually, in practice, we need a time step of less than $1/10$ of the problem's stability limit, and, similarly, a grid spacing less than $1/3$ of its stability limit in order to ensure a sufficient energy conservation. This fact makes the code performance to be problem dependent.

2.6.3. Diagnostics

The output of a PIC code is very similar to the quantities measured in actual plasma experiments, which is a great advantage. One obtains information on both the fields and the distribution of the particles involved. By splitting the diagnostics into two groups by these considerations, we typically have the following information.

- *Particle diagnostics:*
 - phase space output (v_p versus x_p);
 - particle density distribution onto the grid;
 - velocity distributions (particles sorted by their respective energies).
- *Field diagnostics:*
 - field plots (E, B);
 - Fast Fourier Transform modes of the field quantities in order to get growth rates.

Also, a lot of useful information is derived from the integral quantities. Here are a few examples in the non-relativistic limit:

$$E_k = \frac{1}{2} \sum_p m_p v_p^2 \rightarrow \text{total kinetic energy} \quad (55)$$

$$P = \sum_p m_p v_p \rightarrow \text{total momentum} \quad (56)$$

$$E_E = \Delta x \sum_c \frac{\epsilon_0 E^2}{2} \rightarrow \text{total electric field energy} \quad (57)$$

2.6.4. Normalization and non-dimensional units

Usually in theoretical physics derivations are done using non-dimensional units. This is even more important in computational physics, helping us keep numbers close to order one, resulting in the best accuracy for finite digit operations.

When using codes developed for plasma physics it is convenient to use the following normalizations. First let us consider space and time. This normalization is done by utilizing the plasma frequency and the speed of light:

$$t' = \omega_{pe} t \quad (58)$$

$$l' = \frac{\omega_{pe} l}{c} \quad (59)$$

which results in times being counted in periods of electron plasma waves and length in electron inertial lengths ($d_e = c/\omega_{pe}$).

The charge (and mass) can be normalized in units of charge (mass) within the unit cube:

$$Q' = \frac{Q}{n_0 e d_e^3} \quad (60)$$

$$M' = \frac{M}{n_0 m_e d_e^3} \quad (61)$$

All the other quantities encountered in the simulations can be derived from the normalized length, time, mass and charge.

In practice, when choosing these normalizations, it is easy to set fundamental quantities as 1. For example, the charge, mass and density are all linked to that of the electron, so we choose $e = 1$, $m_e = 1$, $n_e = 1$, leading to a unitary plasma frequency. In addition, if we set $\epsilon_0 = 1$ and $\mu_0 = 1$ ($c = 1$), the normalizations for velocity, charge and mass are also done. As an example, if these fundamental values are chosen to be the unit, we will have the mass for hydrogen $M_i = 1836$ if $m_e = 1$.

2.6.5. Boundary conditions

When doing this kind of simulations, we need to impose two sets of boundary conditions, one for the fields and another for the particles.

Because the method involves solving Maxwell's equations, the field boundary conditions are set similarly to other methods that involve solving these equations. To best represent a physical system, we can have particle boundary conditions such as: boundary reflection, periodic boundary (a particle exits one boundary and re-enters the opposite boundary with the same attributes) or removal.

Another possibility in these kind of simulations is injection. We can have an arbitrary inflow of plasma. This procedure can be based on deterministic methods (quiet starts) or, much more common, based on statistical methods (random starts).

Having a broad introduction into the particle-in-cell method, in the following 3 chapters, we will report the results obtained using the PICLS [83] numerical code. In order to suit the needs of our studies, several modifications were performed into the code regarding the file output of the code and the ionization modules used. A more detailed look of the changes performed can be found in the Annex section.

Chapter 3

Laser ion acceleration from micro-structured solid targets

Since their discovery, laser accelerated ion beams have been the subject of great interest. With the latest advances in attainable laser intensity, the need to obtain better quality ion and electron beams has been a major field of research. Laser ion acceleration is strongly linked to the generation and transport of hot electrons by the interaction of ultra-intense laser light with matter. Comparing ion acceleration experiments at laser systems with different beam parameters and using targets of varying thickness, material and temperature, some insight on the underlying physics can be obtained. This chapter studies the effects of different target density profiles on the spatial distribution of the accelerated particles, the maximum energies achieved, and the characteristics of the electromagnetic fields using the same laser pulse parameters.

The TNSA mechanism allows the use of different target geometries in order to achieve a better focusing of the particle beams in the order of tens of microns with high energy densities [85], [92], [103-105]. Hot electrons are produced through the irradiation of a solid foil with an intense laser pulse; these electrons are transported through the target,

forming a strong electrostatic field, normal to the target surface. Protons and positively charged ions from the back surface of the target are accelerated by this field until the electron charge is compensated.

The hot electron density and temperature in the rear vacuum depend on the target geometrical and composition properties such as target curvature, pulse focusing structures and microdots for enhanced proton acceleration [41], [82-84], [86-87], [106-109]. In order to optimize the laser accelerated particle beams we have investigated the proton and ion energy and the angular distribution by means of two-dimensional (2D) particle-in-cell (PIC) simulations of the interaction of ultra-short laser pulses with several microstructured targets.

The study starts by describing a baseline for a flat target which presents a proton-rich microdot on its backside. For the scope of this study, the laser pulse parameters were kept constant, while varying the target parameters. The laser parameters chosen are in line with the preparatory experiments for the newly build ELI-NP facility. Many of the studies already performed use the parameters for existent laser installations, and such, there is a need to prepare initial experiments on multi-PW emerging installations. The effects of introducing a target curvature and, further on, a cone laser focusing structure are compared with the flat target baseline results. The maximum energy obtained increases when using complex structures, and also a smaller divergence of the ion beam is observed.

3.1. Simulation parameters

For the simulations of microstructured solid targets, the work started with three different density profiles: flat target, curved target and concave tip cone target, as shown in Figure 12. All the density profiles have attached on their backside a proton-rich microdot. The importance of microstructured target has been also previously studied experimentally in [41]. The targets are composed of two layers, an Aluminum layer of 2 μm thickness (shown in blue in Figure 12) and a 0.1 μm thick microdot (shown in orange in Fig. 12). For the curved targets, the inner radius of the Aluminum layer is 18 μm , while for the third, concave tip cone target, the slope of the pulse focusing cone is approximately 17° .

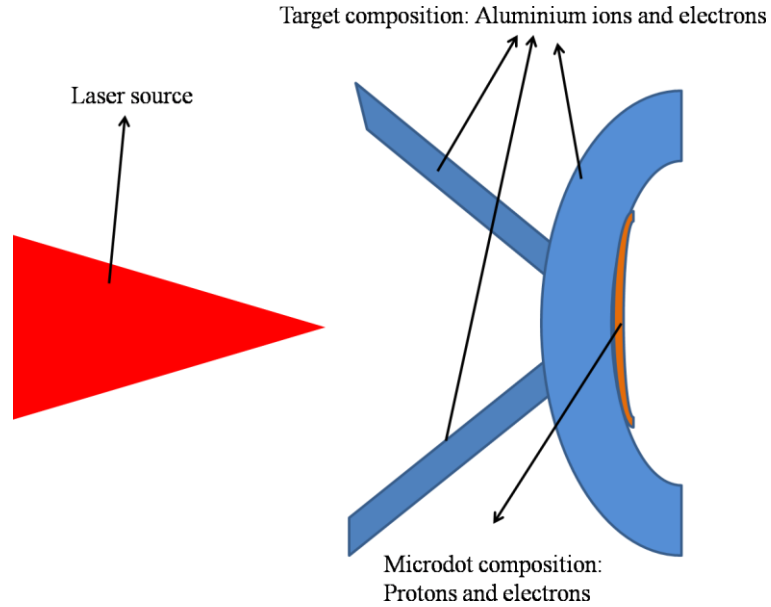


Figure 12. Basic geometrical setup for a target with pulse focusing cone structure and proton-rich microdot to increase the maximum number of accelerated particles.

The simulation box is composed of a grid with the size of 2200x2000 cells. Each cell contains 28 particles within the Aluminum target (2 Aluminum ions and 26 electrons) and 52 particles in the microdot (26 protons and 26 electrons). The target density is considered in the simulations to be $750 \cdot n_c$ (n_c is the critical density of the plasma, $n_c = 1.1 \cdot 10^{21} / \lambda_\mu^2 \text{ cm}^{-3}$). The laser pulse used in the simulations has a Gaussian profile with an irradiance of 10^{22} W/cm^2 at a wavelength of $\lambda_\mu = 1000 \text{ nm}$, a transverse FWHM of the focal spot of $5 \mu\text{m}$ and a period of $\tau = 3.3 \text{ fs}$, consisting of a total of 24 periods, with a full width at half maximum (FWHM) of 12 periods. The spatial and temporal resolution ($\lambda/\Delta x$ and $T_0/\Delta T$) are set to 100. The pulse focus point is at the tip of the cone structure (the front border of the foil structure).

3.2. Results and discussion

The simulations of the laser-foil interaction were done for the three target profiles using the PIC code PICLS [80]. In the following, the proton, electron and Al ions energy spectra, the electromagnetic fields and the particle distributions are compared.

3.2.1. Flat Target with Microdot

In order to determine the influence of the target geometry on the particle beam characteristics, a baseline case of a flat target with microdot was studied (Figure 12(a)). The foil is populated by Al ions and electrons, with a microdot consisting of protons and electrons on the back surface of the foil. The microdot is of the same dimensions as the laser spot size. Due to the fact that, for this case, the laser pulse is normal to the target surface in all points, the main laser absorption mechanism is $\mathbf{j} \times \mathbf{B}$ heating [16].

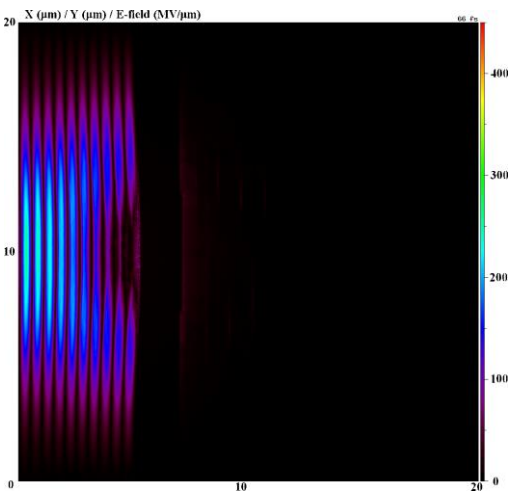


Figure 13. Instantaneous E-field magnitude at 66 fs for the flat microdotted target.

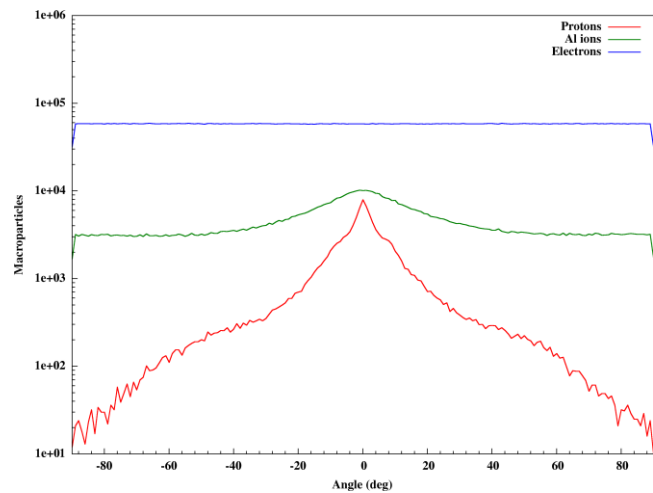


Figure 14. Angular distribution at 198 fs for protons - red curve, Al ions - green curve and electrons - blue curve for the flat microdotted target.

In Figure 13 the instantaneous E-field magnitude at the time the laser pulse reaches the target is plotted while the electron, proton and ion angular distributions are plotted in Figure 14. The angular distribution is plotted only for the forward-accelerated particles, 0° being the direction normal to the target surface.

Looking at Figure 15, the maximum energy reached in our simulation is 88.7 MeV for electrons, 51.7 MeV for protons and 10.6 MeV for Al ions (per nucleon) in the case of a flat target with a proton-rich microdot. We can observe that the maximum longitudinal electrostatic field (which is linked to the hot electron temperature and density) is reached between 90 and 100 fs, with a swift decrease after 100 fs due to the energy transfer from electrons to ions, until the charge separation field associated to the electron decreases and the ion acceleration decreases in efficiency (the velocity of electrons and ions equalizes).

The electrostatic field accelerating the protons and ions depends on these parameters [81] and this can be seen from Figure 16 that presents the temporal evolution of the electromagnetic fields. The decrease of the maximum energy for the Al ions and protons corresponds to the exit of the most energetic Al ions, respectively protons, from the simulation box.

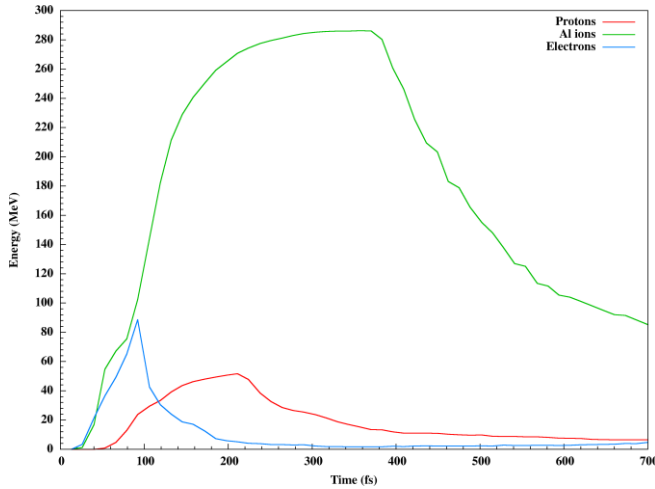


Figure 15. Temporal evolution of the maximum energy for: protons - red curve, Al ions - green curve and electrons - blue curve in the case of the flat microdotted target.

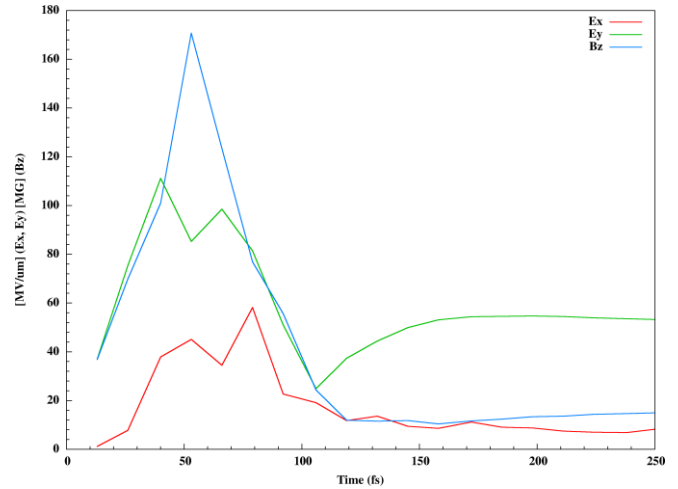


Figure 16. Temporal evolution of electromagnetic fields for the flat microdotted target; Ex - red curve, Ey - green curve, Bz - blue curve.

The energies that were observed in our simulations are consistent with the expected energies from the model presented in Chapter 1, as TNSA is the main accelerating mechanism that occurs.

3.2.2. Curved Target with Microdot

The target curvature has been demonstrated to have a significant effect both on the magnitude of the resulting electromagnetic field which accelerates the ions and on the ion angular distribution as this field is mainly directed perpendicularly to the target surface [82-85]. Coupling the improved characteristics resulting from a curved foil with a posterior side proton-rich microdot we expect to obtain high-energy collimated proton beams. Starting from these premises a numerical study was conducted on a curved 2 μm

Aluminum foil with a 0.1 μm Hydrogen microdot, the same transverse size as the pulse spot, on the target back side (Figure 12(b)).

By analyzing Figure 17 one can observe that, because of the target curvature, part of the laser pulse is reflected from the target surface, making this case ineffective in terms of laser energy conversion. Due to the back side positioning of the microdot, we observe an improvement in the angular distribution of the protons. From Figure 18 we can clearly see that the protons are accelerated at a maximum 60° angle from the target normal direction, with the majority of particles having a divergence of less than 20° from the normal direction.

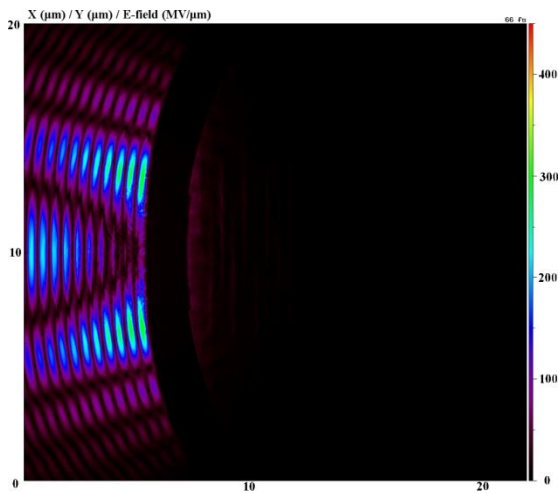


Figure 17. Instantaneous E-field magnitude at 66 fs for the curved microdotted target.

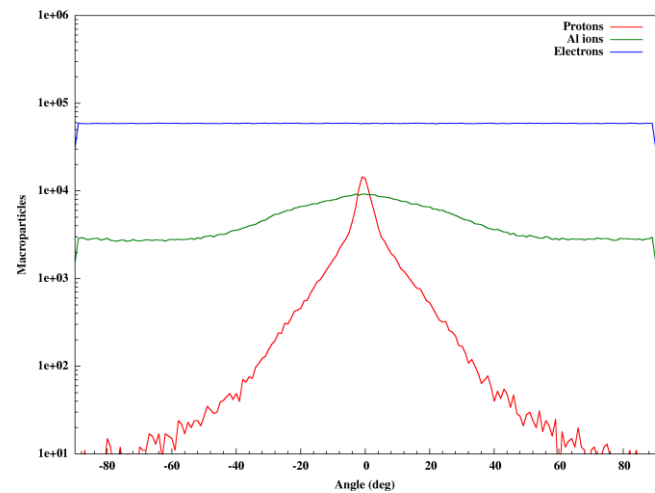


Figure 18. Angular distribution at 198 fs for protons - red curve, Al ions - green curve and electrons - blue curve for the curved microdotted target.

The maximum energy is 112.0 MeV for electrons, 91.5 MeV for protons and 22.4 MeV for Al ions (per nucleon) in the case of a curved target with a proton-rich microdot. Figure 19 depicts the maximum energy evolution during the simulation and indicates that the introduction of a curvature to the foil has a significant effect on the maximum energies of the accelerated particles.

By comparing the time evolution of the electromagnetic fields (Figure 20) with the flat target case (Figure 16) we can clearly see that the profiles are similar (with a slight

improvement for the longitudinal electric field E_x in the curved microdotted target case, consistent with the maximum ion energy increase) hence the achieved enhancement in the maximum energy can be attributed to the focusing effect generated by the target curvature which increases the local hot electron density and therefore the accelerating electric field amplitude.

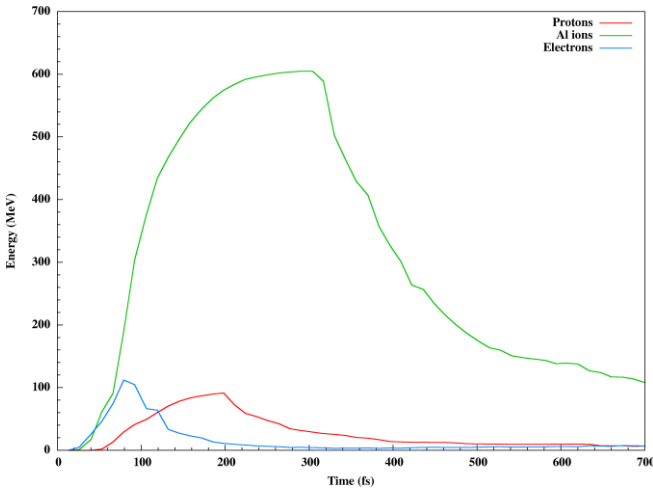


Figure 19. Temporal evolution of the maximum energy for: protons - red curve, Al ions - green curve and electrons - blue curve in the case of the curved microdotted target.

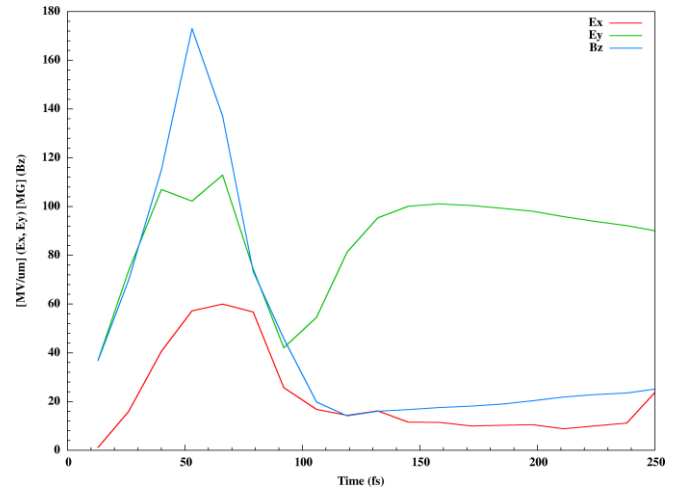


Figure 20. Temporal evolution of electromagnetic fields for the curved microdotted target; E_x - red curve, E_y - green curve, B_z - blue curve.

3.2.3. Curved Target with Microdot and a Pulse Focusing Cone-Like Structure

Previous studies on the laser light propagation inside conical targets revealed that the laser is focused at the tip while, at the same time, it interacts with the cone sides, accelerating electrons that are transported to the cone tip, thus enhancing the electromagnetic fields [86], [87], [83]. A complementary numerical study was conducted for a concave tip cone target with a proton-rich microdot (for enhanced proton acceleration) as shown in Figure 12(c).

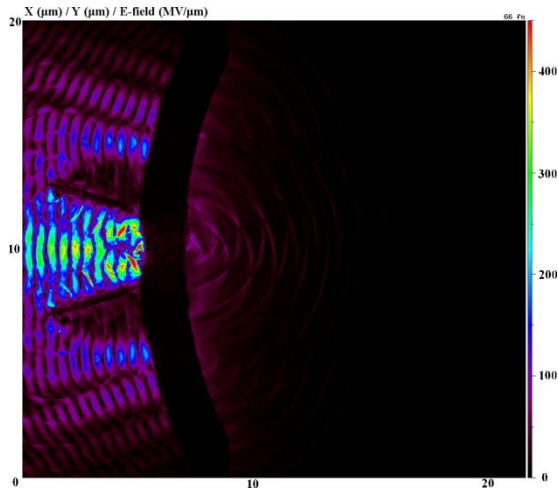


Figure 21. Instantaneous E-field magnitude at 66 fs for the cone microdotted target.

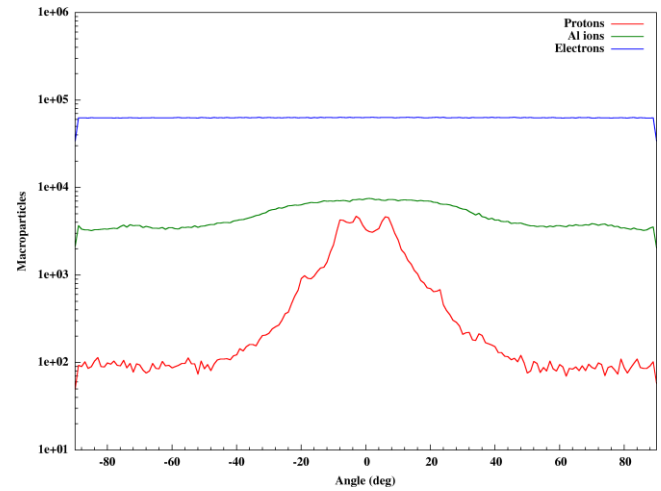


Figure 22. Angular distribution at 198 fs for protons - red curve, Al ions - green curve and electrons - blue curve for the cone microdotted target.

The results obtained in this case indicate, as expected, that the cone structure both focuses the laser pulse and guides towards the tip the hot electrons generated by the interaction of the laser light with the cone sides.

The pulse focusing effect of the cone-like structure can be clearly seen in Figure 21. Compared to the case of the simple curved foil (Figure 17), the reflections off the target are diminished, being contained mostly in the cone structure. Also, due to the cone structure, the laser energy is focused on a much smaller target surface, leading to an improved acceleration process, as demonstrated by the higher electron and ion energies achieved (Figure 23).

By looking at the angular distributions (Figure 22) we can observe a degradation of the focusing of the proton beam compared to the case without the cone (Figure 18). This larger angular spread is a consequence of the proportionality between the microdot surface and the cone tip size. Because the acceleration is done in the TNSA regime having a microdot with a surface larger than the cone tip means that the edges of the microdot will be accelerated at large angles (above 60°) from the target normal direction.

Also, as a result of using a concave tip cone target, the maximum energy, shown in Figure 23, (619.551 MeV for electrons, 187.454 MeV for protons and 44.03 MeV per nucleon for Al ions) is greatly increased compared to the other two cases (Figure 15 and

Figure 19). Consequently, the electromagnetic fields generated (Figure 24) are much higher than in the other two cases (Figures 16 and 20). The increase of the electromagnetic fields at times later than 100 fs can be attributed to the numerical error caused by the limited size of the simulation box. The increase in total electron energy observed after 500 fs corresponds to numerical heating but its effect on the laser-plasma interaction and subsequent ion acceleration is negligible as these occur on much shorter time scales.

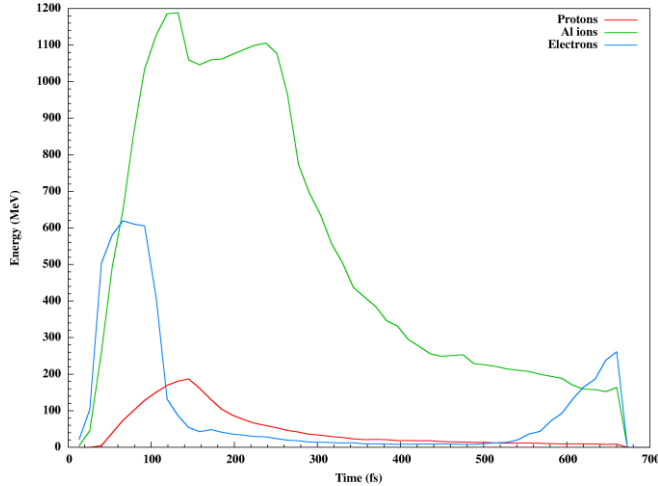


Figure 23. Temporal evolution of the maximum energy for: protons - red curve, Al ions - green curve and electrons - blue curve in the case of the cone microdotted target.

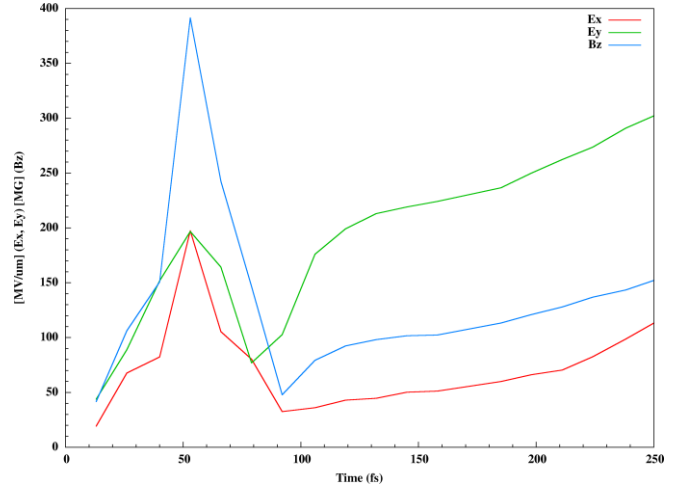


Figure 24. Temporal evolution of electromagnetic fields for the cone microdotted target; Ex - red curve, Ey - green curve, Bz - blue curve.

3.2.4. Improving the beam characteristics obtained from laser ion acceleration interaction with micro-structured solid targets

In order to determine the effect of the different profiles, baseline cases for flat foils have been studied for the purpose of comparison. When referring to the baseline cases, the laser pulse is normal to the target surface in all points, thus the main laser absorption mechanism is $\mathbf{j} \times \mathbf{B}$ heating [16].

Case #	Case characteristics
1	100 nm thick flat foil
2	2 μm thick flat foil and high density microstructure
3	2 μm thick flat foil with cone focusing structure and high density microstructure
4	2 μm thick curved foil and high density microstructure
5	2 μm thick curved foil with cone focusing structure and high density microstructure
6	2 μm thick curved foil with cone focusing structure and low density microstructure
7	2 μm thick increased curvature foil with cone focusing structure and low density microstructure

Table 1. Characteristics of the seven cases performed within this study

Figure 25 depicts the maximum energies achieved for all the seven cases studied (characteristics presented in Table 1) with electrons energies in black triangles, protons energies in red circles and Al ions energies in green squares.

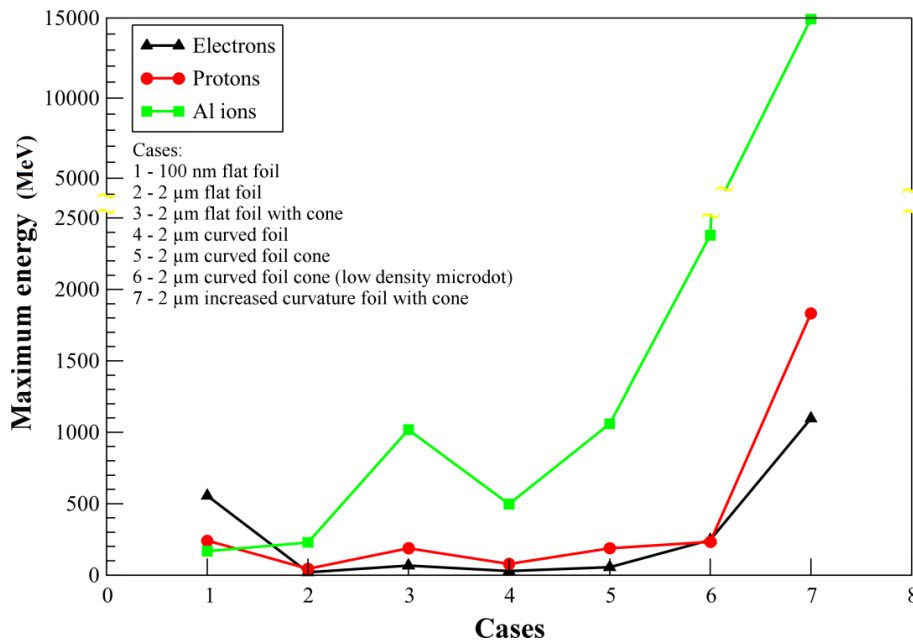


Figure 25. Maximum energies plot for the 3 species involved. The black triangles, the red circles and the green squares correspond respectively to electrons, protons and Al ions.

We can observe a significant increase of the maximum energy of the accelerated particles due to the effect of the cone focusing structure obtained for case 3. This is achieved as a result of the superior hot electron conversion facilitated by the introduction of

the cone structure. When comparing cases 2 and 4 a slight increase of the maximum energy is observed through the introduction of a curvature in target geometry. The maximum energy profiles are similar for the flat and curved cases with a cone focusing structure, as seen in Figure 25, cases 3 and 5. A significant increase in the maximum energy of the Al ions can be observed starting with case 6 that is owed to the decrease in density of the microdot layer (thus having a faster depletion of the microstructure layer), respectively because of the increase in foil curvature in case 7, as will be discussed in the next chapter.

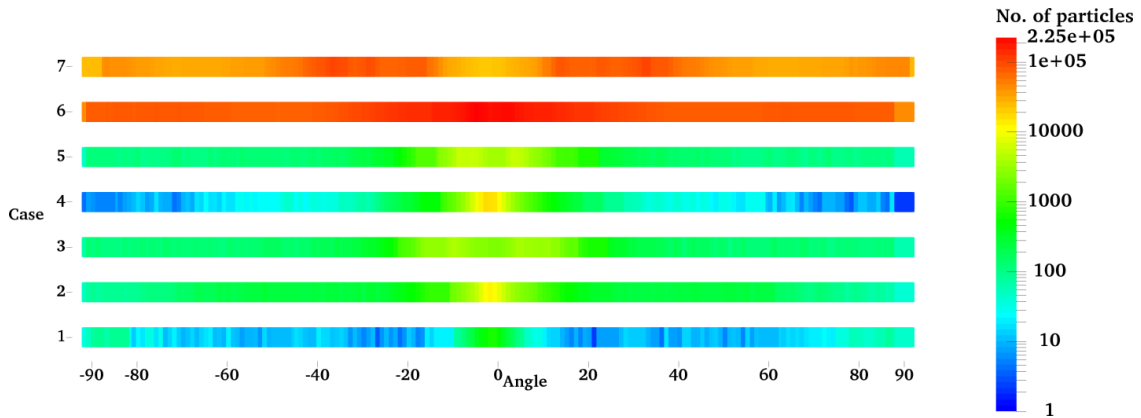


Figure 26. Angular distribution of the protons in all seven studied cases

The collimation of the accelerated particle beam is of great interest for the goal of this work. For this purpose, the angular distribution was plotted for the protons (Figure 26), for all seven cases studied. This distribution is plotted only for the forward-accelerated particles, 0° being the direction normal to the target surface.

From the angular distribution plot we can observe that, when considering the whole range of proton energies, the particle collimation seems to decrease, but when considering the high energy particles, we have a majority of them being accelerated at angles lower than 30° from the normal direction. It is also important to note that in the cases where a pulse focusing cone structure is used, the number of accelerated particles increases significantly.

3.3. Conclusions on structured targets

This study has been focused on the particularities of three types of target density profiles with a proton-rich microdot: flat, curved and cone target with a concave tip. It is

important to note that at the onset of the ultra-high intensity regime the improvements in maximum particle energy and angular distribution follow the trends observed in lower intensity cases previously studied in the literature [82-87]. While each of these target augmentations (curvature, microdot and cone structure) has its advantages, a composite target featuring all three attributes has the potential to produce higher quality proton and ion beams. From our simulations we can clearly see that the case of a microdotted concave tip cone target has led to the most favorable results in terms of hot electron conversion, laser pulse focusing and particle beam maximum energy. Further studies will have to be done in order to confirm that the poor proton angular distribution for the cone target is a consequence of the proportionality between cone tip size and microdot size.

The studied cases indicated that the trends presented in past works are followed, so it is important to note the conservation of these attributes at the onset of the ultra-high energy regime. By comparing the cases of flat versus curved, we can observe that by adding a slight curvature to the target, a better collimation is achieved in the case of protons.

The cone structure indeed has a significant effect of enhancing the electric field generated by the laser pulse into a smaller area corresponding to the microdot on the back surface of the target. Further increasing the target curvature, coupled with the focusing effect of the cone structure, has a significant positive effect on the maximum energies attainable and also on the maximum number of accelerated particles but also presents the downside of increasing the energy dispersion of the accelerated particles.

Considering the trends observed for these specific laser parameters, one can say that in order to port these results to increased laser intensity new target optimum thicknesses and curvatures need to be found. Similarly, if one would increase the laser pulse duration the cone focusing structure size would need to be changed in order to avoid it being completely destroyed in the process.

Although the results obtained from 2D simulations are a good stepping stone for experiment characterization, future work should focus on 3D simulations, in order to have a better approximation of the results expected from experiments [102].

The results of this study were published in two AIP Conference Proceedings articles [88], [89]: Dragos Tatomirescu, Alexandra Popescu, Emmanuel d'Humières and Daniel

Vizman, *Numerical Simulation of Laser Ion Acceleration at Ultra High Intensity*, AIP Conf. Proc. 1796, 020013-1–020013-6 and Dragos Tatomirescu, Emmanuel d'Humières and Daniel Vizman, *Improving the Particle Beam Characteristics Resulting from Laser Ion Acceleration at Ultra High Intensity through Target Manipulation - Numerical Modeling*, AIP Conf. Proc. 1916, UNSP 030002.

Chapter 4

Target curvature influence on particle beam characteristics resulting from laser ion acceleration with microstructured enhanced targets at ultra-high intensity

With the latest advances in laser science, the need to produce superior quality ion and electron beams has been a hot research field in the past decade. The work presented in this chapter focuses on the parametric study of target curvature in order to determine its effect on the spatial distribution of the accelerated proton beam, the proton maximum energy, and the characteristics of the gamma photons produced for potential usage as secondary sources.

For the scope of this work, the laser pulse parameters were kept constant, while varying the curvature radius of the target. As declared in the previous chapter, the laser parameters are chosen in order to be similar to the preliminary experiments that will be done at the ELI-NP facility. This study continues the work presented in Chapter 3 and focuses on further studying the effects of target curvature coupled with a cone laser

focusing structure. The results show increased particle beam focusing and a significant enhancement in particle maximum energy.

4.1. Simulation parameters

The numerical studies presented in this chapter comprise five density profiles. Each case consisted of a concave foil with a laser focusing cone structure where the curvature radius of the foil was varied between 50 μm and 10 μm with a 10 μm decrement.

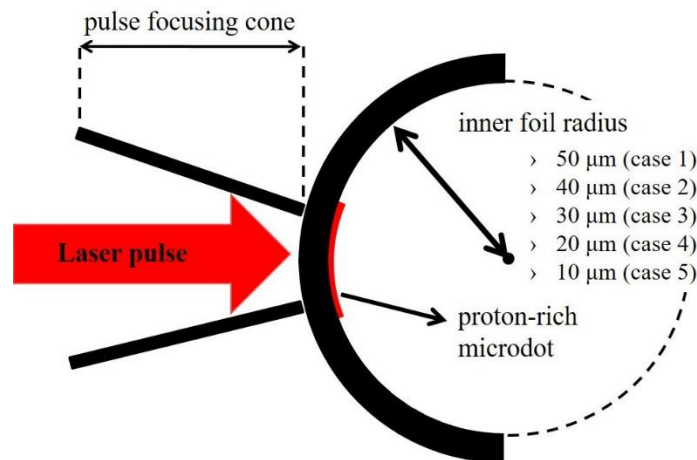
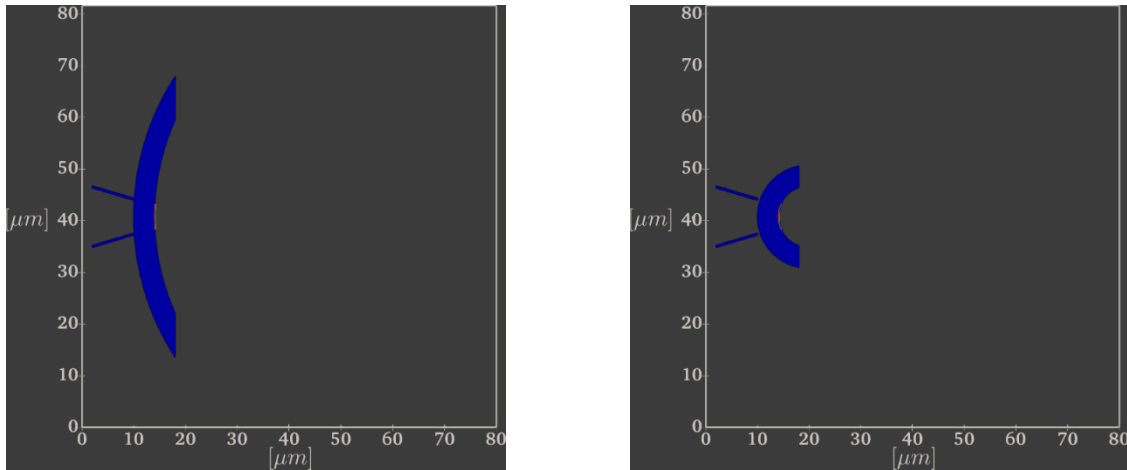


Figure 27. Basic geometrical setup for target with pulse focusing cone structure and proton-rich microdot to increase the maximum number of accelerated particles

The basic setup for the target density profile is shown in Figure 27. The density profiles have attached on their backside a proton-rich microdot (red arc on Figure 27).

The targets are composed of two layers, an Aluminum layer of 4 μm thickness and a 0.2 μm thick proton-rich microdot. The slope of the pulse focusing cone is approximately 17° and the foil is connected to the focusing structure, having an inner radius of 50 μm in the first case (Figure 28a), and with each new case the curvature radius was further reduced by 10 μm . The smallest value of the curvature radius is 10 μm , and it can be seen in Figure 28b. The simulation box is composed of a grid with the size of 4000x4080 cells. Each cell contains 28 particles within the Aluminum target (2 Aluminum ions and 26 electrons) and 52 particles in the microdot (26 protons and 26 electrons).



a) Case 1: 50 μm curvature radius

b) Case 5: 10 μm curvature radius

Figure 28. Particle density profiles for cases 1 and 5 at simulation step 0; In blue we have the Aluminum populated layers, while in red is depicted the proton-rich microdot

The target density is considered in the simulations to be $75 \cdot n_c$ ($n_c = \epsilon_0 m_e \omega_0^2 / e^2$ is the critical density of the laser) in the Aluminum target and $750 \cdot n_c$ in the proton-rich microdot. The spatial and temporal resolutions ($\lambda / \Delta x$ and $T_0 / \Delta T$) are set at 50. The laser pulse used in the simulations has a Gaussian profile with an irradiance of 10^{22} W/cm². The full width at half maximum (FWHM) of the focal spot is 5 μm and the period is $\tau = 3.3$ fs, the pulse consisting of a total of 24 periods. The pulse focus point is at the tip of the cone structure (the front border of the foil structure).

4.2. Results and discussion

In Chapter 3 we have shown that, in order to have a superior quality for the accelerated particle beam, multiple target optimizations can be performed. The addition of a proton-rich microdot on the back side of the target has led to a substantial increase in the amount of accelerated protons. The size of this structure, relative to the transverse width of the laser pulse in focus, also has a significant effect on the characteristics of the accelerated particles. Within this chapter, we will further study the effects the curvature of the foil has on the acceleration of particles.

In the following we will discuss the simulation results obtained with the conditions previously described. The analysis of the results is done at 475.2 fs after the start of the interaction, the time when the laser pulse has fully interacted with the target.

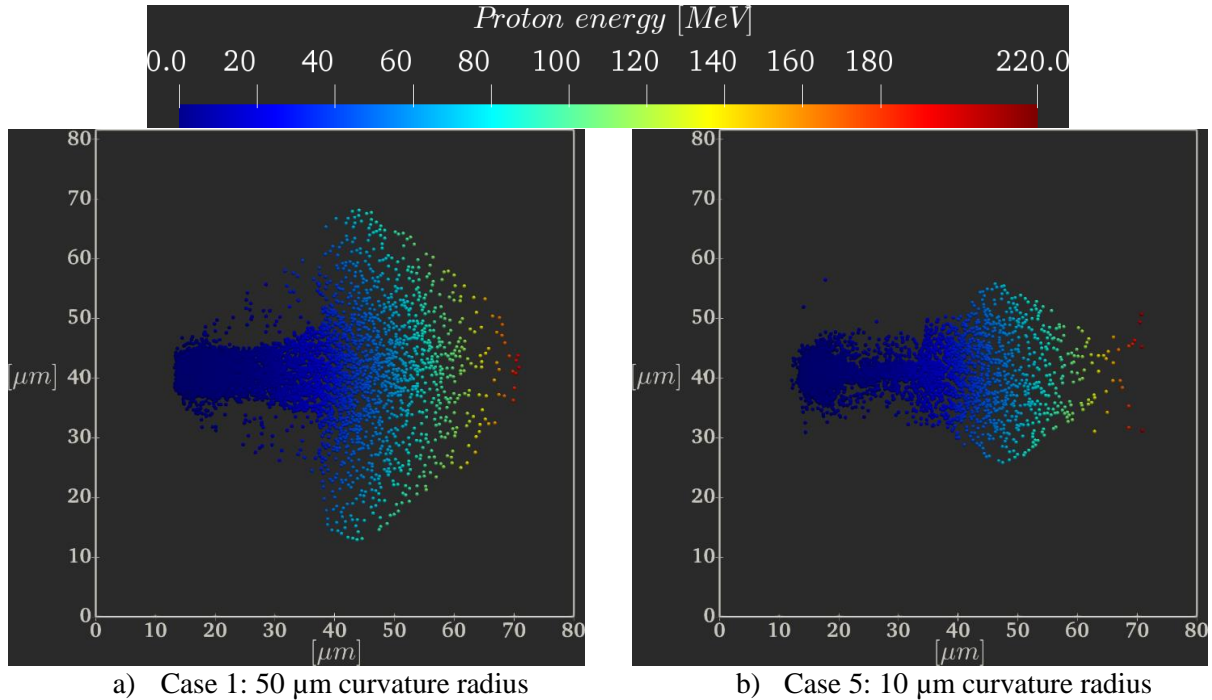


Figure 29. Proton energy distribution within the simulation box; the colour scale represents the energy distribution in the simulated geometry (475.2 fs after the start of the simulation).

When analyzing the energies of the accelerated protons and the shape of the accelerated spectrum (Figure 29), we find that the outline is similar, with an increase in the maximum energy as the curvature of the foil changes. Figure 29.b, showing the proton energies for the foil with the smallest curvature radius, has the highest value for proton energy (we can also observe in Figure 29.b that the highest energy protons have past their focusing point), approximately 207 MeV, about 15 MeV increase from the biggest curvature radius case (Figure 29.a), where we have a maximum energy for the protons of 193 MeV. Having all other target and pulse parameters constant throughout the different cases, we can pinpoint this increase in maximum energy to the foil curvature. The increase in energy is also smaller than the increase observed between cases 5 and 7 in the previous chapter. This fact can be attributed to the increased thickness of the foil for the cases presented here.

Furthermore, along with the increase in energy, we can observe a superior collimation in the case of a target with a smaller curvature radius of the foil (Figure 30). In the case of the 10 μm curvature (Figure 30.b), we can see that the protons with energies above 15 MeV are accelerated at angles under 30° , while in the 50 μm curvature case (Figure 30.a), for the same energies, we can observe that the particle spectrum is less collimated, reaching angles as high as 60° .

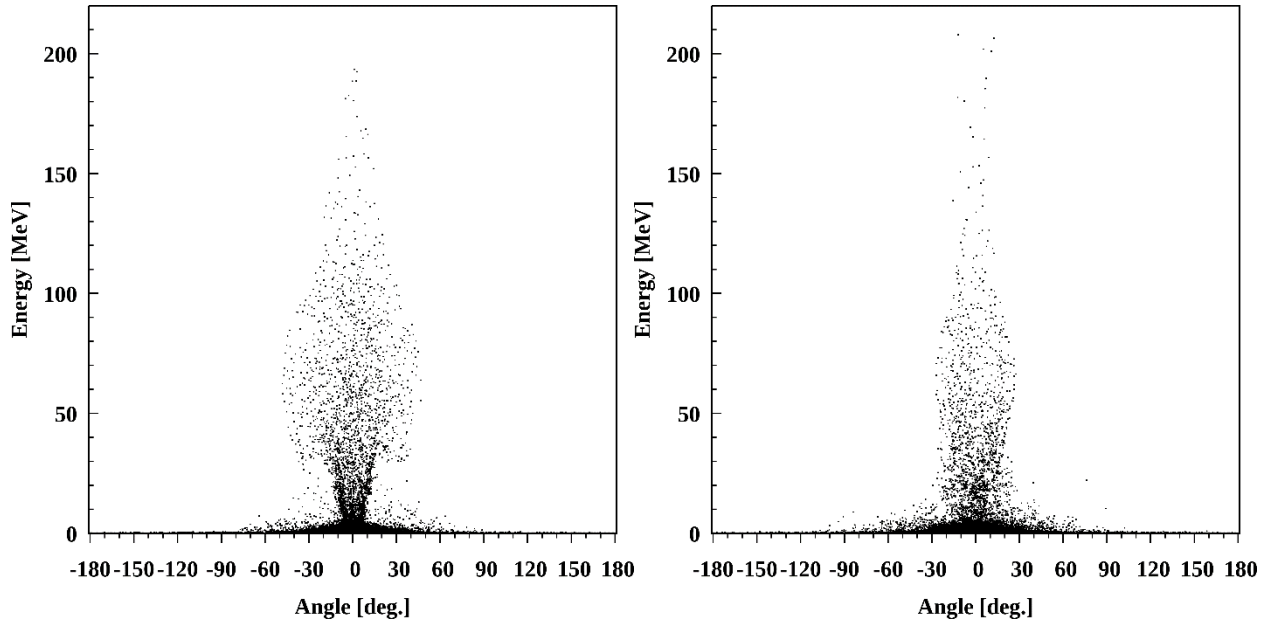
a) Case 1: 50 μm curvature radiusb) Case 5: 10 μm curvature radius

Figure 30. Proton energy as a function of the angle between the accelerated particles and the normal direction (475.2 fs after the start of the simulation).

Another important aspect of our study is the production of gamma photons. Because of the ultra-high intensity of the laser pulse, the radiation loss of an accelerated electron can no longer be negligible and affects the electron motion (radiative damping). The PICLS code solves the relativistic equation of motion of the radiating electron, and has implemented the friction force (1st-order term) and the damping of the Lorentz force (2nd-order term) equations within the Boris scheme (time centered scheme) to integrate the kinetic equation [90]. This process becomes dominant at high intensities, such as those described here, when the Bremsstrahlung emissions saturate and thus is the main source of hard x-rays in this regime.

In Figure 31 we present the angular energy distribution of the emitted gamma photons plotted for least curved (Figure 31.a) and the most curved (Figure 31.b) target cases. We can distinguish two peaks in these distributions, located at 0.2 rad (11.45°), respectively 0.4 rad ($\sim 22.91^\circ$).

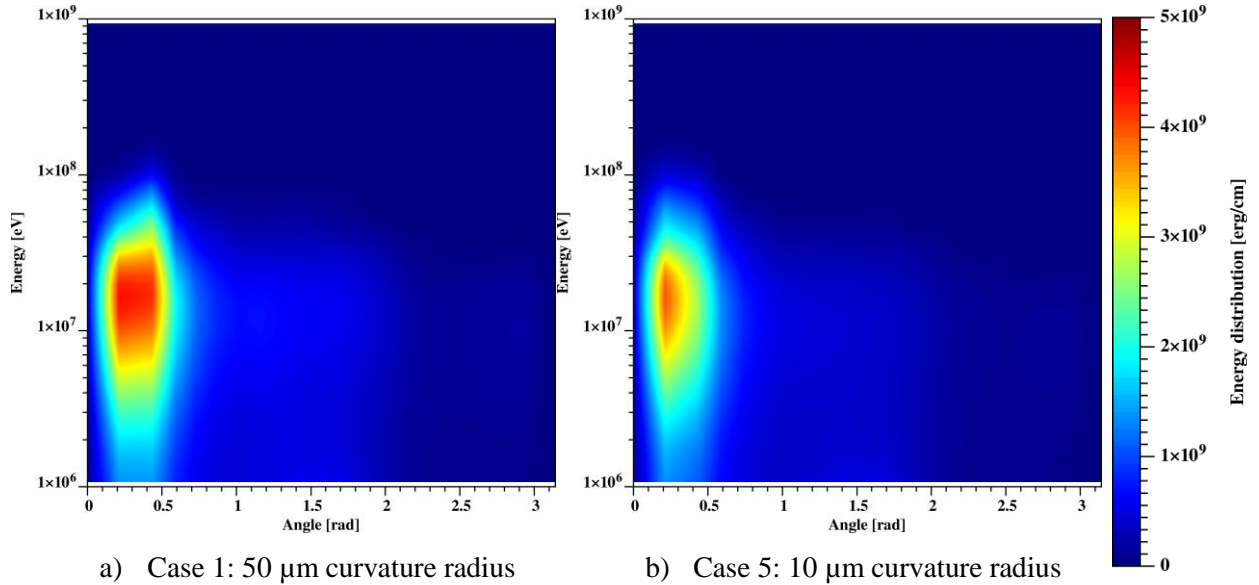


Figure 31. Photon energy distribution as a function of the angle between the photon and the normal direction; the colour scale represents the energy distribution in the simulated geometry.

While in the case of a high curvature radius the peak at 0.4 rad is predominant, we can see that in the low curvature radius case this peak is severely diminished, leaving the 0.2 rad peak predominant. These results support the trends observed for the angular distribution of the protons. Having mainly a TNSA acceleration regime, the preferential acceleration direction of the ions follows the most energetic electrons acceleration direction. This fact indicates that the photons are mainly generated due to synchrotron-like emission.

Analyzing the photon count as a function of their energy (Figure 32), we can observe that the general trend of the photon energy distribution is conserved within all the density cases presented. A cutoff at the 50 MeV energy level is observed for the higher curvature radius cases simulated. However, as the target curvature radius decreases, we can see a decrease in high energy photons. This fact can be attributed to the fact that with this

curvature decrease, the mass of the target is decreased, thus less electrons populate the Aluminum foil.

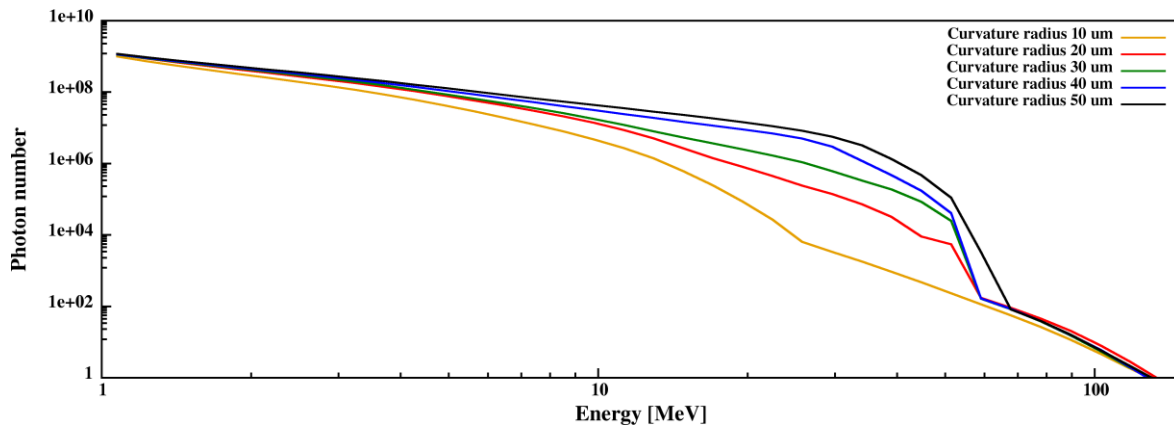


Figure 32. Photon count as a function of their energy; profiles represented for the 5 different foil curvature radii studied.

In terms of laser energy absorption (trends presented in Figure 33), as we are modeling a microstructured target, the absorption percentage of the laser light into the target is high, above 90%. It is also obvious from Figure 33 that the profiles of the 5 cases studied are very similar, with a slight decrease as the target curvature decreases.

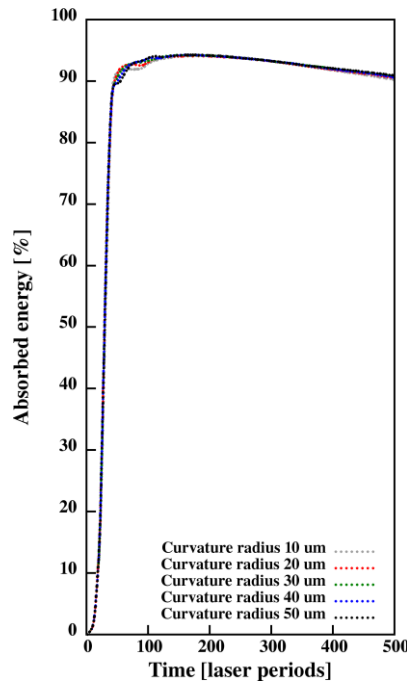


Figure 33. Percentage of laser energy absorbed in the target; profiles represented for the 5 different foil curvature radii studied.

When looking at the energy distribution between the particle species during the simulation for our 5 cases, Figure 34, we can observe the increase in total energy for the Al ions with the decrease in curvature radius. It does not seem to be the case for the total energy converted in protons.

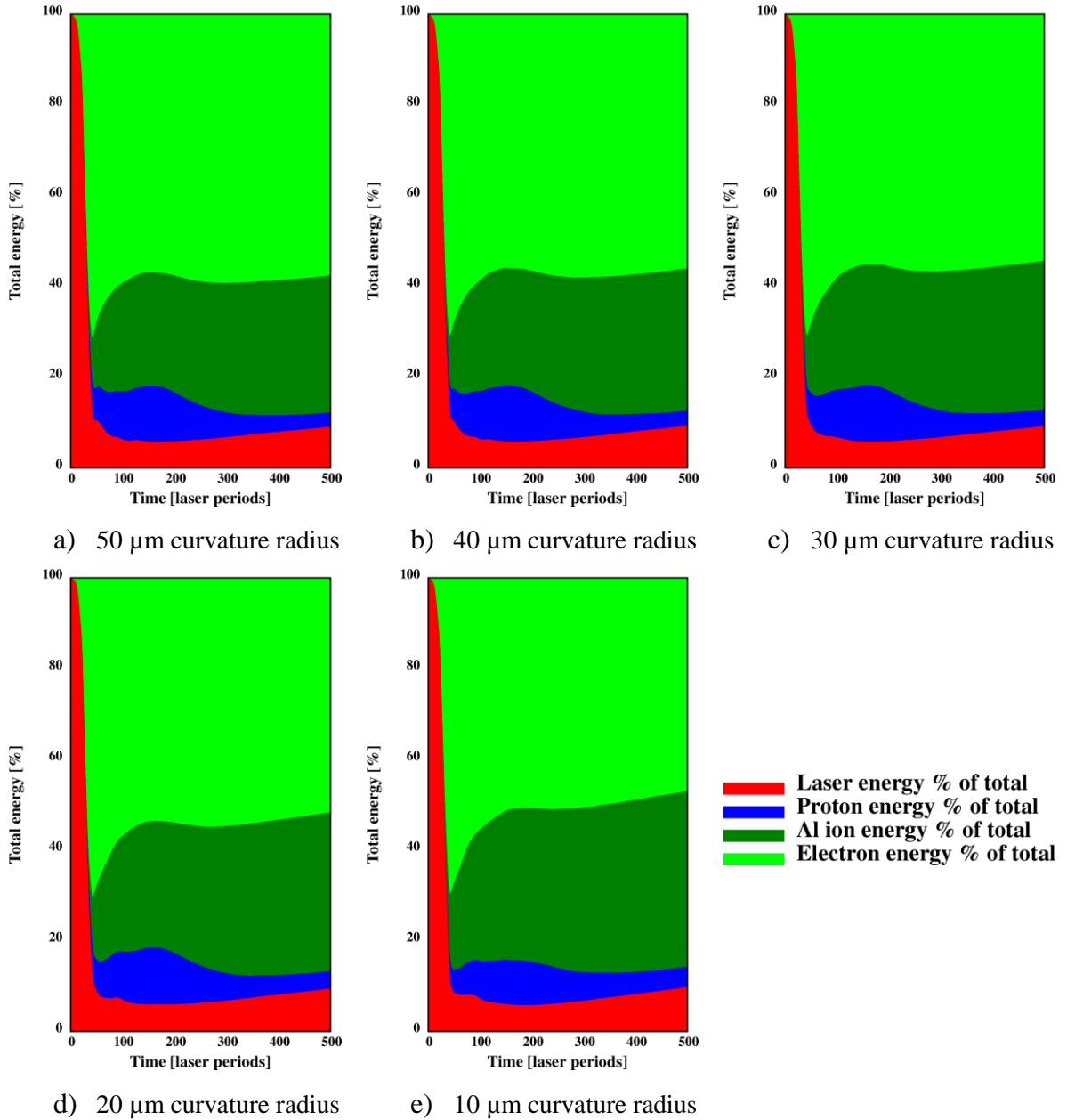


Figure 34. Energy balance during the simulations; profiles represented for the 5 different foil curvature radii studied

4.3. Conclusions on curvature influence

The results of the study presented in this chapter show the effects resulting from the manipulation of the target curvature of a microstructured Aluminum foil enhanced with a cone focusing structure in interaction with a high intensity ultra-short laser pulse in order to prepare first ultra-high intensity experiments on facilities like BELLA, CETAL, APOLLON and the ELI high power lasers. The influence target curvature has on the protons accelerated from a curve shaped foil that is enhanced with a proton-rich structure on the inner edge was presented.

We have shown that, with the decrease in curvature radius the maximum energies of protons are increased, noting a 15 MeV increase from the highest curvature radius case to the lowest one, corresponding to an 8% increase in energy. While discussing the protons, we have seen in previous experimental studies [41] that a proton rich structure attached to the back side of the target enhances the proton beam spectrum. The numerical modeling performed within this study further demonstrates this assumption. Furthermore, we observed that as the curvature radius of the foil decreased, the collimation of the protons improved, leading to acceleration angles under 30° from the normal direction for particles over 15 MeV.

The emitted gamma photons observed reach a maximum energy around 100 MeV and present a good collimation under 0.4 rad ($\sim 22^\circ$). However, we observed a decrease in high energy photon number tied to the decrease in foil curvature radius due to reductions in target mass as the curvature decreases.

As also stated in the previous chapter, any change in laser parameters requires further changes to the target parameters in order to find new optimum values that will result in the most efficient particle acceleration. In this respect, a further study into the optimum foil thickness will be performed in order to determine the thickness required for the most efficient acceleration, conserving the most favorable curvature and microstructure parameters.

The results of this study were sent to publication in the Plasma Physics and Controlled Fusion journal [93]. The article identifiers are: Dragos Tatomirescu, Daniel Vizman and Emmanuel d'Humières, *Target curvature influence on particle beam characteristics resulted from laser ion acceleration with microstructured enhanced targets at ultra-high intensity*.

Chapter 5

Laser ion acceleration and high energy radiation generation from near-critical gas jets

In the past two decades, laser-accelerated ion sources and their applications have been intensely researched. Recently, it has been shown through experiments that proton beams with characteristics comparable to those obtained with solid targets can be obtained from gaseous targets [62], [68-73]. By means of Particle-In-Cell simulations, the work presented in this chapter studies in detail the effects of a near-critical density gradient on ion and electron acceleration after the interaction with ultra-high intensity lasers. Compared to solid targets where we have limited laser absorption to the target surface, the laser pulse inside low density targets heats electrons on a large volume which leads to a higher laser absorption overall. This acceleration regime is also advantageous for several applications because of the reduced debris produced. Another advantage of such targets is the adaptability to high repetition rate lasers. A typical problem for thin foils is the laser contrast, but in the case of near-critical targets this becomes less detrimental than in the case of solid targets, as gas jets do not absorb much laser energy for laser intensities below

10^{13} W/cm² for a one micron wavelength laser. Ion acceleration produced from the interaction of a very high intensity laser with underdense targets has been studied with Particle-In-Cell (PIC) simulations [68-70], but the simulated targets did not reproduce the gas targets available for experiments. The first experiments of ion acceleration via laser interaction with underdense targets showed radial acceleration [71]. Recent experiments proved that using high intensity lasers one can obtain strong longitudinal proton acceleration [62], [72,73]. In this case the energy of the longitudinally accelerated protons is greater than the one of the transversally accelerated protons. The accelerating mechanism that causes the energetic accelerated ions seen in [62], [72,73] has not yet been described in detail and therefore is the center of an ongoing debate [63, 64]. In the case of near-critical gas targets, the density gradient is not easy to achieve experimentally (however, such experimental endeavors have been achieved in the past [74]), thus, the dependence of the particle acceleration on the specific plasma density is important in order to optimize such experimental efforts.

We can observe that the peak density of the gas jet has a significant influence on the spectrum features. As the gas jet density increases, so does the peak energy of the central quasi-monoenergetic ion bunch due to the increase in laser absorption while at the same time having a broadening effect on the electron angular distribution.

5.1. Simulation parameters

In this work, 2D PIC simulations were performed using the code PICLS [80]. The wavelength of the incident pulse is 1 μm , with a laser pulse period of 3.3 fs, consisting of a total of 24 periods, with a full width at half maximum (FWHM) of 12 periods, and an irradiance of 1×10^{22} W/cm². The transverse FWHM of the focal spot is 5 μm . The pulse focus point was set at the middle of the gas jet (60 μm from the left border of the simulation box). The pulse interacts with the target at normal incidence and the spatial and temporal profiles are truncated Gaussians. The proposed laser parameters are in accordance with the parameters obtainable at CETAL, and were chosen in order to perform preparatory experiments for the ELI-NP facility. The plasma is composed of Xenon ions and electrons with a maximum density that was varied from $1n_c$ up to $4n_c$ ($n_c = \epsilon_0 m_e \omega_0^2 / e^2$ is the critical

density of the laser). The development of very dense gas jets intended for laser-plasma interaction experiments was already proven [94].

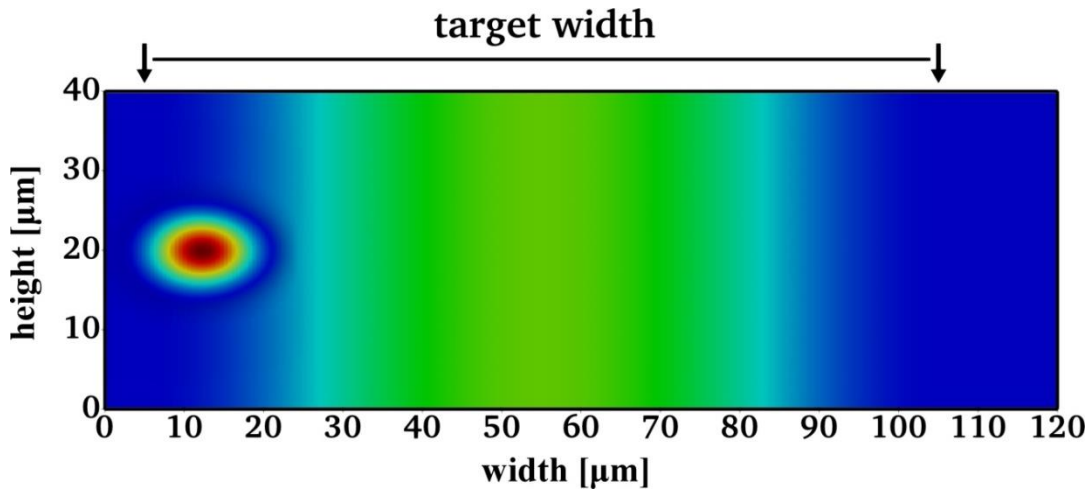


Figure 34. Representation of the density and laser pulse set-up used for the simulations; \cos^2 density profile in the x direction with a 50 microns FWHM and uniform in the y direction with the laser pulse coming from the left side, propagating along the x direction.

The simulation box is composed of a grid with the size of 1200x400 cells. Each cell contains 55 macroparticles (54 electrons and 1 Xe ion). The gas target has a \cos^2 density profile with a 50 microns FWHM in the x direction and uniform in the y direction. The spatial and temporal resolutions ($\lambda/\Delta x$ and $T_0/\Delta T$) are set to 10. These resolutions are enough to correctly describe the laser propagation in vacuum and in the plasma for the density chosen in the study considering the directional splitting scheme that is used in the PICLS code [95].

Each simulated case performed 3011 iterations, amounting for 1 ps of real-time interaction. The PICLS code used for the simulation work uses the ionization module presented in [96]. The general setup for the studied cases can be seen in Figure 34.

5.2. Results and discussions

In the following we will discuss the simulation results obtained with the conditions previously described. The analysis of the results is done at 429 fs after the start of the interaction, at the moment when the laser pulse exits the simulated gas jet.

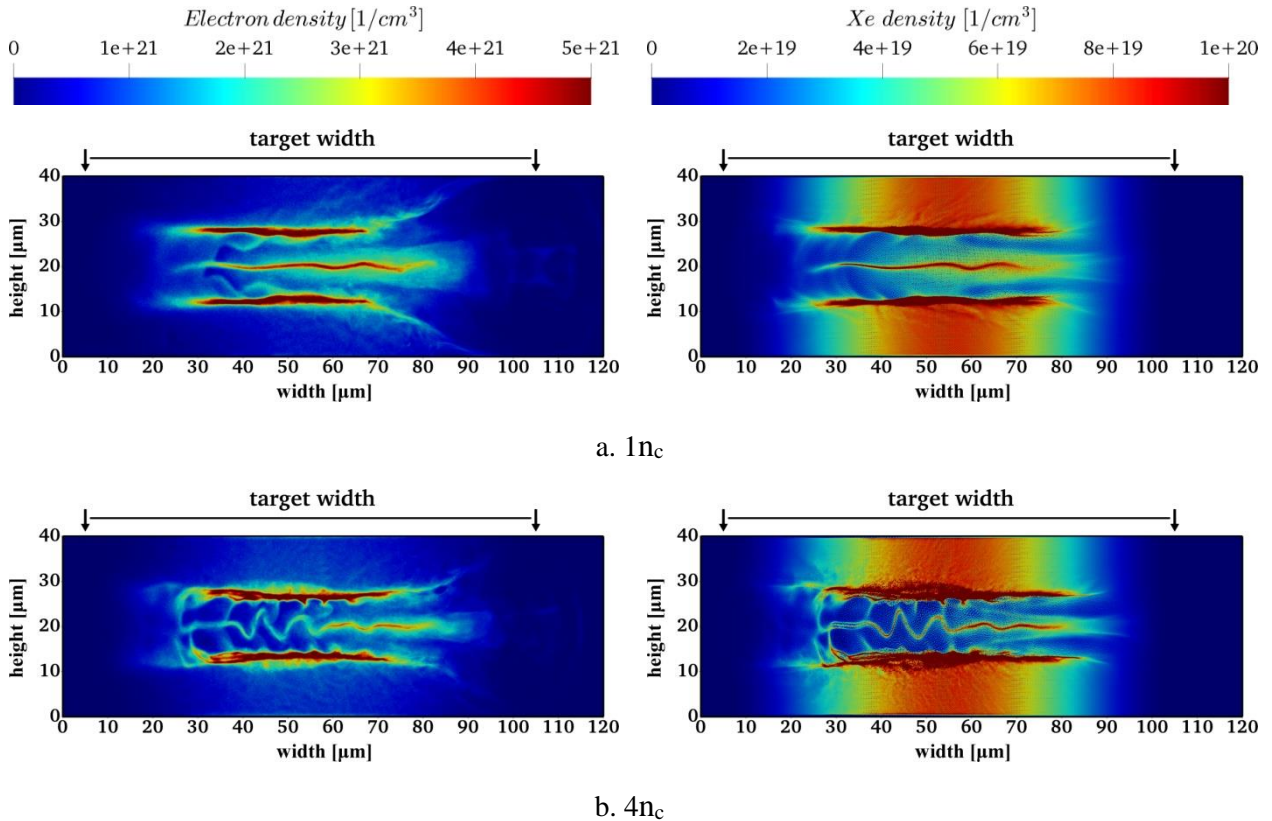


Figure 35. Electron density distribution (left) and Xe ions density distribution (right) for: a. $1n_c$ and b. $4n_c$ in a simulation box of size $120 \times 40 \mu m$, 429 fs after the laser pulse enters the simulation box, with the target extending between 5 and 105 μm on the x direction. The maximum visualized density is set to $5 \cdot 10^{21} cm^{-3}$ in the case of electrons, respectively $1 \cdot 10^{20} cm^{-3}$ for the Xe ions, densities above these set values being represented at maximum colour scale value.

As expected, due to the gaseous nature of the simulated target, initially, the focused ultra-short laser pulse rapidly ionizes the gas particles as an effect of the strong electromagnetic field that is created at the edges of the laser pulse.

After its creation in the target, the plasma interacts with the most intense part of the laser pulse, pushing the plasma electrons in radial directions as an effect of the

ponderomotive force. This radial acceleration forms a spherical shaped cavity within the target (which surrounds the laser pulse as it advances), with a dense sheath of electrons at its edge. As seen in Figure 35, the charge displacement produced by the movement of this cavity through the gas target accelerates the Xe ions in a similar transverse direction.

In order to achieve a better visibility for the density changes within the target, Figure 35 was plotted with a maximum density for the color scale that is below the maximum density. The maximum visualized density is set to $5 \cdot 10^{21} \text{ cm}^{-3}$ in the case of electrons, respectively $1 \cdot 10^{20} \text{ cm}^{-3}$ for the Xe ions. Densities above these set values being represented at maximum color scale value.

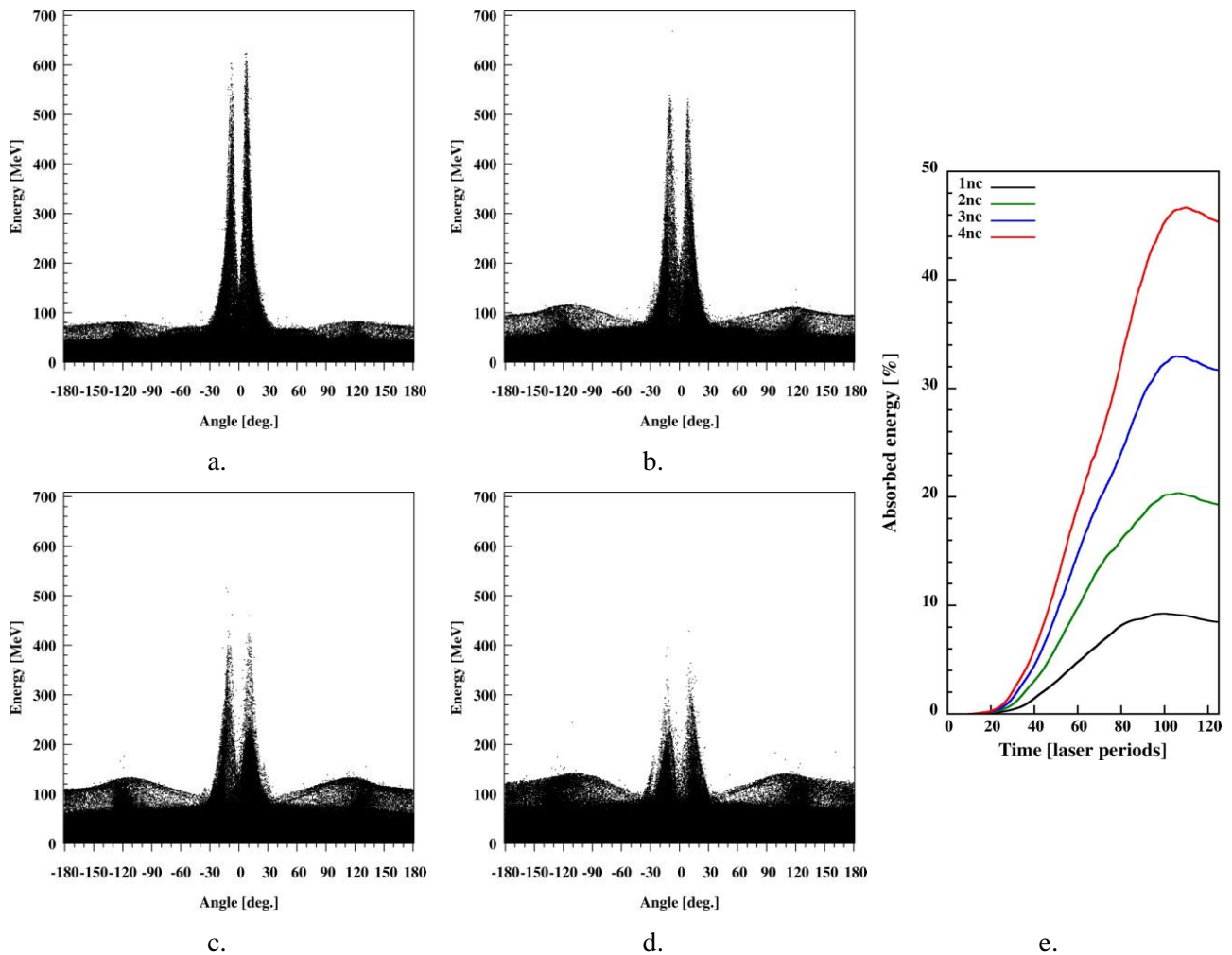


Figure 36. Electron energy as a function of the angle between the accelerated particles and the normal direction for a. $1n_c$, b. $2n_c$, c. $3n_c$ and d. $4n_c$ (429 fs after the start of the simulation). e) Laser absorption for all studied cases.

Furthermore, we can observe that with each density increment the amount of laser energy that is absorbed increases (Figure 36e), making the channel acceleration due to the movement of the cavity through the target geometry more clear at high densities. When investigating the angular energy distributions of the accelerated electrons (seen in Figure 36), it is obvious that the most efficient acceleration is being done at a 15° angle in relation to the normal incidence.

Also, with the increase in target density we can observe a decrease of the electron maximum energy, from 640 MeV in the least dense case, down to 440 MeV in the maximum density case. Even though we observe an increase in laser energy absorption into the target due to the increase in density (Figure 36e), as seen in the past [96] this density increase also has the effect of broadening the angular distribution of the electrons.

Analyzing the angular distribution of the Xe ion energies (Figure 37), we can clearly observe the transverse acceleration that occurs due to the ponderomotive force. The most energetic ions are accelerated at an angle of 90° in relation to the normal incidence on all four cases. Even though the most energetic particles are accelerated in a transverse direction, it is important to note that there is also an important coagulation of accelerated particles, at slightly lower energies, with a collimation of less than 20° . The advancement of this quasi-monoenergetic Xe ion bunch, centered around 600 MeV, through the target can be observed for the maximum density case studied in Figure 37e.

The maximum energy of the ions found in the central bunch increases with the target density, from an approximate value of 4.62 MeV to 11.11 MeV per nucleon while the transversely accelerated ions maximum energy increases from 14.62 MeV to 32.03 MeV per nucleon from the low density case to the high density one. The effects of the increased laser energy absorption (Figure 36e) can be seen in the significant increase in energy for the accelerated ions that occurs with the increase in gas jet peak density.

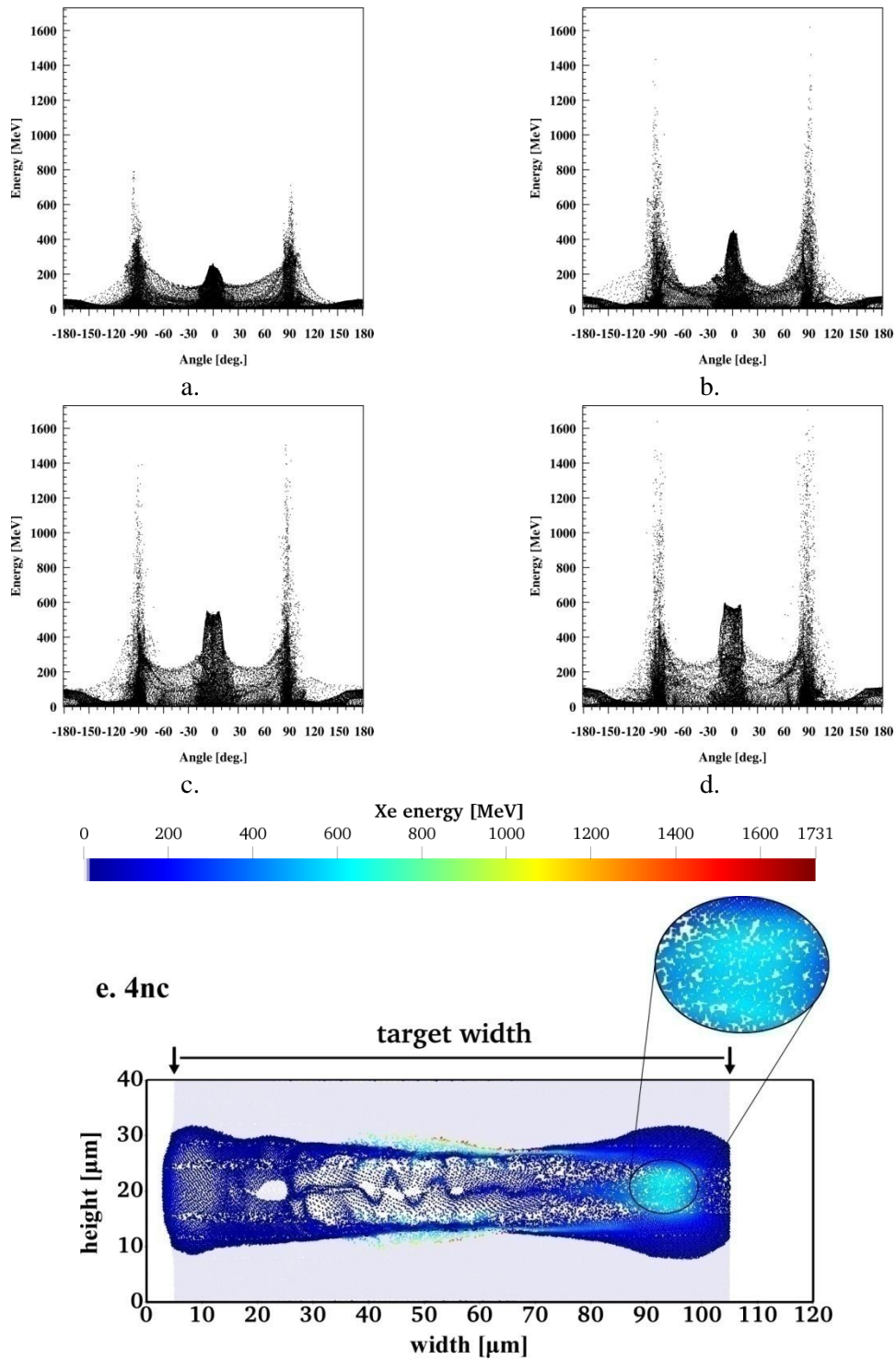


Figure 37. Xe ions energy as a function of the angle between the accelerated ions and the normal direction for a. 1nc, b. 2nc, c. 3nc and d. 4nc (429 fs after the start of the simulation). e) energy distribution within the simulation box for Xe ions in the case of 4 nc density.

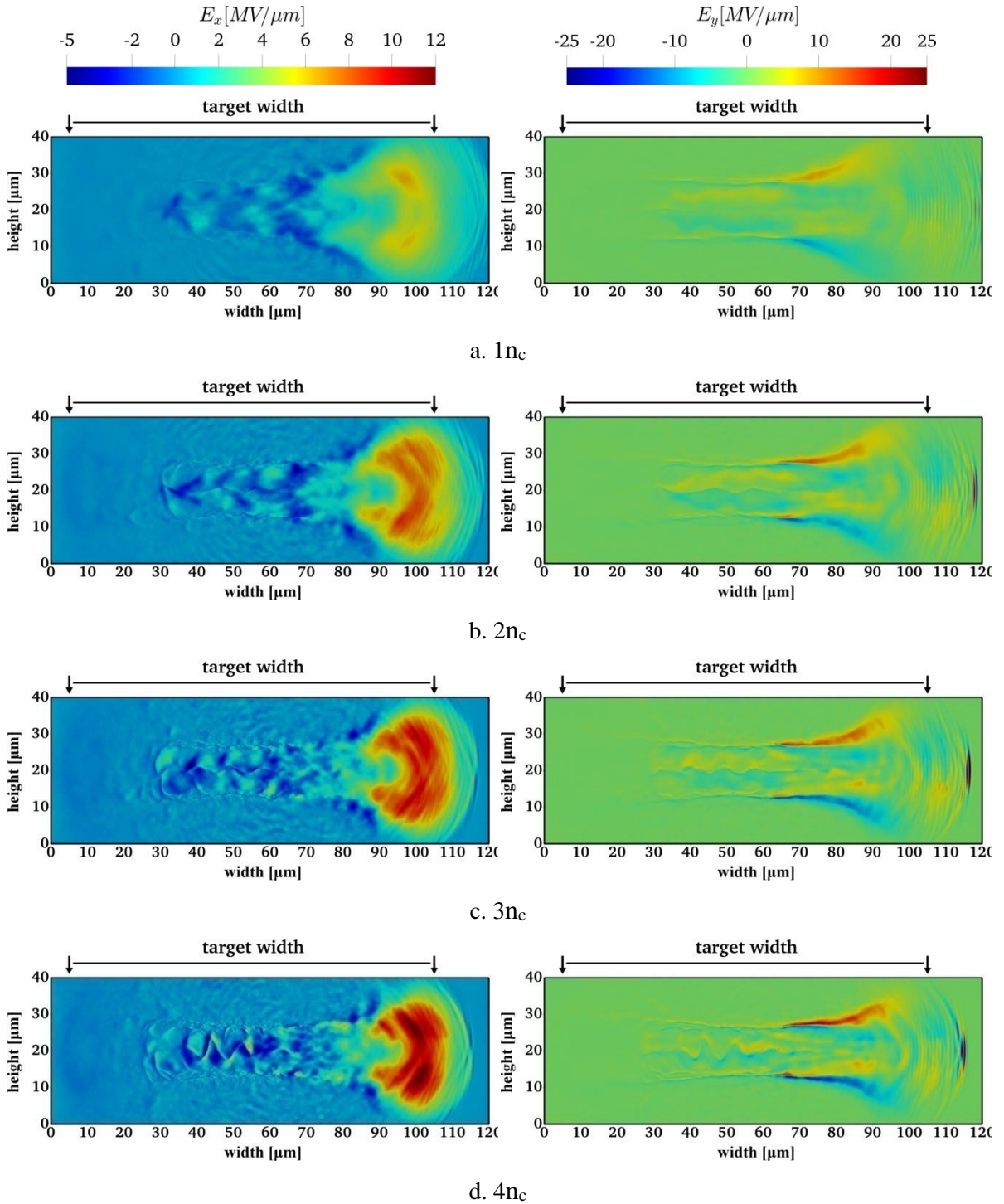


Figure 38. x component of the electric field (left) and y component of the electric field (right) for the studied cases at 429 fs after the laser pulse enters the simulation box.

As expected, we can see in Figure 38 that the y component of the electric field generated by the laser pulse within the target structure exceeds the value of the incident component (E_x), accounting for the greater energies of the radially accelerated particles. The effects of the increased laser energy absorption that occurs with the increase in target density can be observed by looking at the profiles for both components of the electric field. There is a significant increase in the electric field magnitude from the low density case, of target density equal to the laser light critical density (Figure 38a), to the highest density studied, with a target density four times higher (Figure 38d).

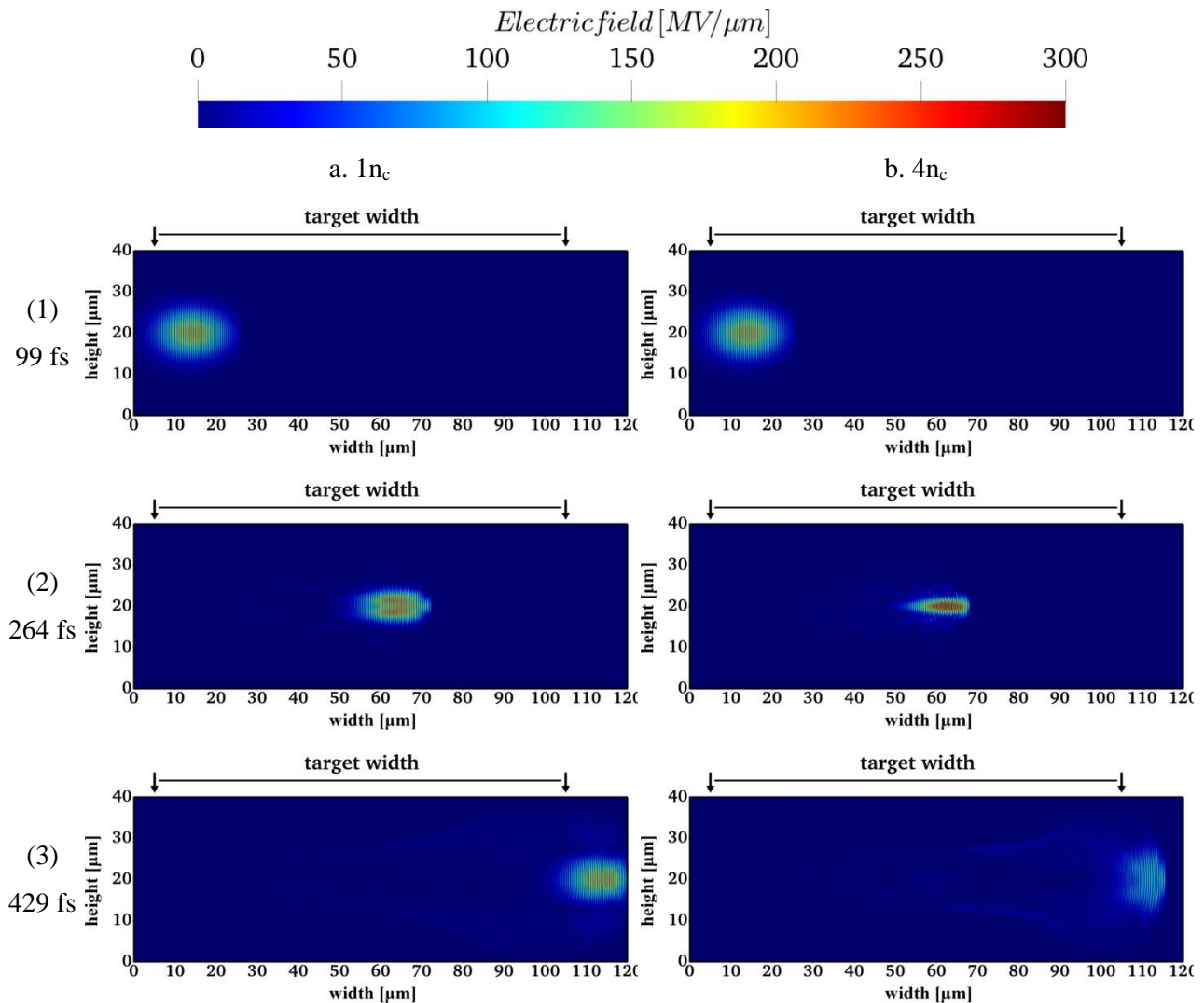


Figure 39. Temporal evolution of the laser pulse for minimum (a) and maximum (b) density at three different timesteps: 99 fs, 264 fs and 429 fs.

In Figure 39, the temporal evolution of the laser pulse interaction with two near-critical plasma densities is presented (the minimum and maximum densities studied in our work).

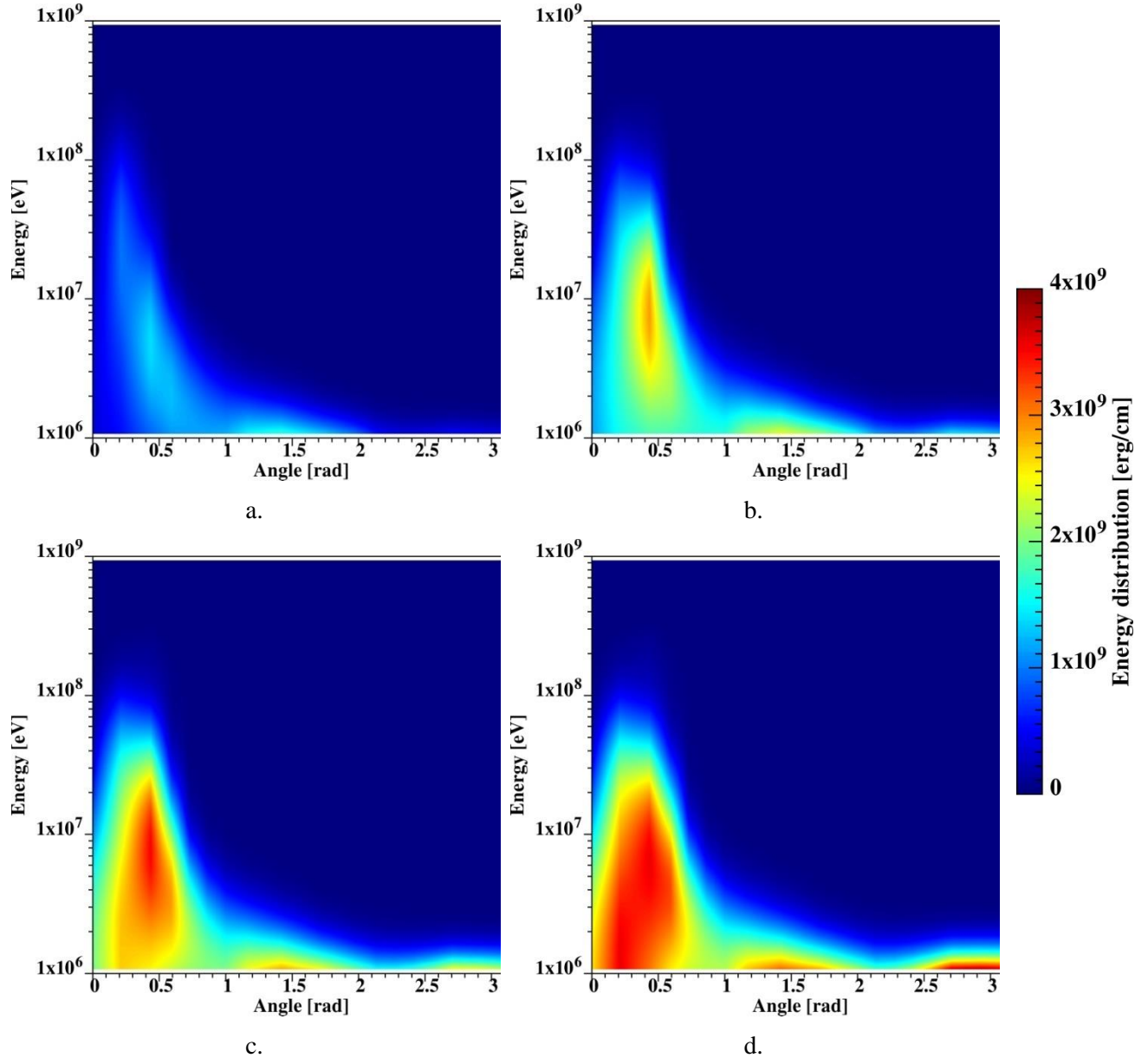


Figure 40. Photon energy distribution as a function of the angle between the photon and the normal direction for a. $1n_c$, b. $2n_c$, c. $3n_c$ and d. $4n_c$; the colour scale represents the energy distribution in the simulated geometry.

We can see that in the case of lower density, shown in Figure 39a., the laser pulse is not focused inside the target, thus being less affected. Meanwhile, as density increases (Figure

39b.), a strong focusing occurs which degrades the laser pulse profile. This also causes a higher absorption of the laser pulse as previously shown in Figure 36.

Another important aspect of our study is the production of gamma photons. Because of the ultra-high intensity of the laser pulse, the radiation loss of an accelerated electron can no longer be negligible and affects the electron motion (radiative damping). As already mentioned in the previous chapter, this process becomes dominant at high intensities, such as those described here, when the Bremsstrahlung emissions saturate and thus radiative damping is the main source of hard x-rays in this regime.

In Figure 40 we present the angular energy distribution of the emitted gamma photons plotted for four different target densities, starting from a density equal to the laser critical density (Figure 40a), to a density of $4n_c$ (Figure 40d). Looking at Figure 40a we can observe that two peaks of emitted photons are emerging at an angular spread of 0.2 rad and 0.4 rad, which is consistent with the preferential direction of emission of the most energetic electrons (see Figure 36). This fact indicates that the photons are mainly generated due to synchrotron-like emission. As the target density increases, Figures 40b and 40c, we obtain an increasingly higher amount of photons emitted on these 2 angular directions. The largest photon energy distribution is achieved in the case of the highest density, 4 times the laser light critical density (Figure 40d), with emission angles under 0.7 rad ($\sim 40^\circ$) and a peak density at 0.4 rad ($\sim 22^\circ$).

Analyzing the photon count as a function of their energy (Figure 41), we can observe that the general trend of the photon energy distribution is conserved within all the density cases presented. The simulation results indicate that the maximum emitted photon count increases with the increase in target density, and a cutoff at the 250 MeV energy level is observed for the cases simulated.

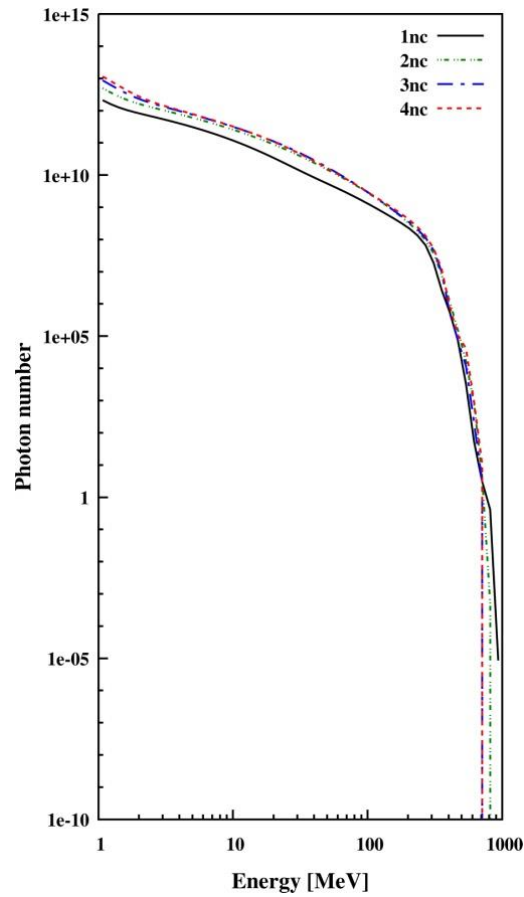


Figure 41. Photon count as a function of their energy; profiles represented for 4 different critical density cases.

The increased absorption observed with the increase in gas jet maximum density can also be seen in the graphs depicting the energy division among the different particle species during the simulations (Figure 42). At times later than 100 fs we see that the amount of total energy being converted to hot electrons is increasingly higher as the density increases. Also, as previously stated, with this increase in hot electron population we also observe an increase in the energy of the accelerated Xenon ions.

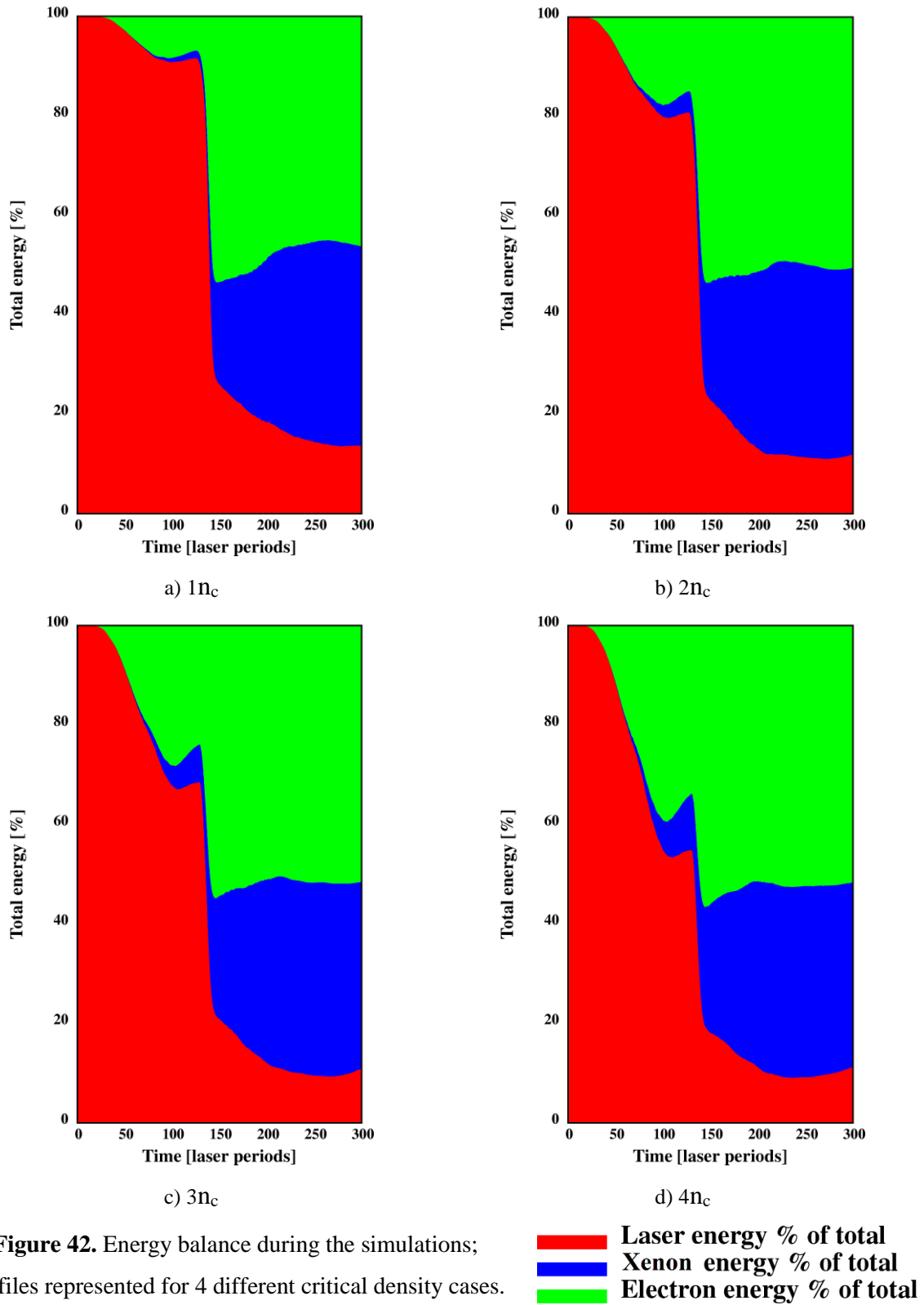


Figure 42. Energy balance during the simulations; profiles represented for 4 different critical density cases.

5.3. Conclusions on near-critical gas targets

This study focused on the effects resulting from the manipulation of the density of a gaseous Xe target in interaction with a high intensity ultra-short laser pulse in order to prepare first ultra-high intensity experiments on facilities like BELLA, CETAL, APOLLON and the ELI high power lasers. The results of the PIC simulations performed indicate that the spectrum features can be controlled by changing the peak density of the gas jet when using ultra high intensity laser pulses, in correlation with the results reported for lower intensity pulses reported in the literature [97], [98].

With the increase in gas density we also observe an increase in energy for the accelerated ions. A careful analysis of the acceleration direction also reveals that in a similar manner, for a simple \cos^2 density profile, the increase in density also accentuates the transverse ion acceleration. Further studies need to be done in order to find a suitable density profile that is both experimentally feasible and can reduce the transverse acceleration that was observed from the use of this geometry. The emitted gamma photons with a maximum energy around 250 MeV present a good collimation under 0.4 rad ($\sim 22^\circ$), with the highest energies observed in the $4n_c$ case. The photon distribution as a function of the energy is consistent through all density cases.

As a continuation of this study, the effects of shooting a laser pulse into a foam-like gas target will be investigated by means of numerical simulation. As stated, the debris generated by gaseous target is severely less than in the case of solid targets, and by encapsulating gaseous media into foam materials would also increase the experiment repetition rate, and possibly decrease the difficulties encountered in manufacturing gas jets that can reach near-critical densities.

The results of this study were published in the Plasma Physics and Controlled Fusion journal [99], with an impact factor of 2.392 and an article influence score of 0.968. The article identifiers are: Dragos Tatomirescu, Emmanuel d'Humières and Daniel Vizman, *Numerical modeling of laser-driven ion acceleration from near-critical gas*, Plasma Phys. Control. Fusion 60 (2018) 064002 (9pp).

Chapter 6

Final conclusions

The study presented in **Chapter 3** has been focused on the particularities of solid foil targets that were enhanced with a proton-rich microdot and a laser focusing cone structure. The curvature of the foil was demonstrated to play an important role in the past, so for this reason, it was also added as a parameter of this study. It is important to note that the results presented indicate that at the onset of the ultra-high intensity regime the improvements in maximum particle energy and angular distribution follow the trends observed in lower intensity cases previously studied in the literature [82-87].

By comparing the cases of flat versus curved, we can observe that by adding a slight curvature to the target, a better collimation is achieved in the case of protons. The cone structure indeed has a significant effect of enhancing the electric field generated by the laser pulse into a smaller area corresponding to the microdot on the back surface of the target. Further increasing the target curvature, coupled with the focusing effect of the cone structure, has a significant positive effect on the maximum energies attainable and also on the maximum number of accelerated particles but also presents the downside of increasing the energy dispersion of the accelerated particles.

While each of these target augmentations (curvature, microdot and cone structure) has its advantages, a composite target featuring all three attributes has the potential to

produce higher quality proton and ion beams. From our simulations we can clearly see that the case of a microdotted concave tip cone target has led to the most favorable results in terms of hot electron conversion, laser pulse focusing and particle beam maximum energy.

The results of this study were published in two AIP Conference Proceedings articles [88], [89]: Dragos Tatomirescu, Alexandra Popescu, Emmanuel d'Humières and Daniel Vizman, *Numerical Simulation of Laser Ion Acceleration at Ultra High Intensity*, AIP Conf. Proc. 1796, 020013-1–020013-6 and Dragos Tatomirescu, Emmanuel d'Humières and Daniel Vizman, *Improving the Particle Beam Characteristics Resulting from Laser Ion Acceleration at Ultra High Intensity through Target Manipulation - Numerical Modeling*, AIP Conf. Proc. 1916, UNSP 030002.

In **Chapter 4** we have shown that, with the decrease in curvature, we experience an increase in proton maximum energy. We saw a 15 MeV difference in maximum energy between the highest curvature case to the lowest one. While discussing the protons, we have seen previously, in Chapter 3 that a proton rich structure attached to the back side of the target enhances the proton beam spectrum. The numerical modeling performed within this study further demonstrates this assumption. Not only did we observe increased maximum energy for the proton with the decrease in foil curvature radius, but also the collimation of the proton beam improved. In the case of 10 μm curvature radius, we observed that the protons with energies above 15 MeV were accelerated at angles no larger than 30° from the normal direction.

While the results of the proton distribution were the main goal of this study, we also looked at the emitted gamma photons for possible applications as secondary sources. We saw maximum energies around 100 MeV, with a good collimation, under 0.4 rad ($\sim 22^\circ$). As the foil curvature radius decreased, we observed a decrease in the number of high energy photons. This decrease can be attributed to the decrease in target mass that was a side effect of the curvature radius reduction.

The results of this study were sent to publication in the Plasma Physics and Controlled Fusion journal [93]. The article identifiers are: Dragos Tatomirescu, Daniel Vizman and Emmanuel d'Humières, *Target curvature influence on particle beam*

characteristics resulted from laser ion acceleration with microstructured enhanced targets at ultra-high intensity.

The study presented in **Chapter 5** focused on the effects resulted from the manipulation of the density of a gaseous Xe target in interaction with a high intensity ultra-short laser pulse in order to prepare first ultra-high intensity experiments on facilities like BELLA, CETAL, APOLLON and the ELI high power lasers. The results of the PIC simulations performed indicate that the spectrum features can be controlled by changing the peak density of the gas jet when using ultra high intensity laser pulses, in correlation with the results reported for lower intensity pulses reported in the literature [94], [96].

With the increase in gas density we also observe an increase in energy for the accelerated ions. A careful analysis of the acceleration direction also reveals that in a similar manner, for a simple \cos^2 density profile, the increase in density also accentuates the transverse ion acceleration. Further studies need to be done in order to find a suitable density profile that is both experimentally feasible and can reduce the transverse acceleration that was observed from the use of this geometry. The emitted gamma photons with a maximum energy around 250 MeV present a good collimation under 0.4 rad ($\sim 22^\circ$), with the highest energies observed in the $4n_c$ case. The photon distribution as a function of the energy is consistent through all density cases.

The results of this study were published in the Plasma Physics and Controlled Fusion journal, with an impact factor of 2.392 and an article influence score of 0.968. The article identifiers are: Dragos Tatomirescu, Emmanuel d'Humières and Daniel Vizman, *Numerical modeling of laser-driven ion acceleration from near-critical gas*, Plasma Phys. Control. Fusion 60 (2018) 064002 (9pp).

References

- [1] M. Borghesi et al.- *Proton imaging: a diagnostic for inertial confinement fusion/fast ignitor studies*, ***Plasma Physics and Controlled Fusion* 43**, A267 (2001).
- [2] M. Roth et al. - *Fast Ignition by Intense Laser-Accelerated Proton Beams*, ***Physical Review Letters* 86**, 436 (2001).
- [3] V. Malka et al. - *Practicability of protontherapy using compact laser systems*, ***Medical Physics* 31**, 1587 (2004).
- [4] S. Bulanov et al. - *Oncological hadrontherapy with laser ion accelerators*, ***Physics Letters A* 299**, 240(2002).
- [5] S. Fritzler et al. - *Proton beams generated with high-intensity lasers: Applications to medical isotope production*, ***Applied Physics Letters* 83**, 3039 (2003).
- [6] S. P. Davis et al. - *Numerical simulations of energy transfer in counter-streaming plasmas*, ***High Energy Density Physics* 9**, 231 (2013).
- [7] W. P. Leemans et al. -*The BErkeley Lab Laser Accelerator (BELLA): A 10 GeV Laser Plasma Accelerator*, ***AIP Conference Proceedings* 1299**, 3 (2010).

- [8] G. A. Mourou, G. Korn, W. Sandner, J. L. Collier (eds.) -ELI - *Extreme Light Infrastructure: Science and Technology with Ultra-Intense Lasers Whitebook*, THOSS Media GmbH (2011).
- [9] A. Macchi et al. - *Laser Acceleration of Ion Bunches at the Front Surface of Overdense Plasmas*, ***Physical Review Letters*** **94**, 165003 (2005).
- [10] A. P. L. Robinson et al. - *Radiation pressure acceleration of thin foils with circularly polarized laser pulses*, ***New Journal of Physics*** **10**, 013021 (2008).
- [11] A. P. L. Robinson et al. - *Relativistically correct hole-boring and ion acceleration by circularly polarized laser pulses*, ***Plasma Physics and Controlled Fusion*** **51**, 024004 (2009).
- [12] E. L. Clark et al. - *Measurements of Energetic Proton Transport through Magnetized Plasma from Intense Laser Interactions with Solids*, ***Physical Review Letters*** **84**, 670 (2000).
- [13] R. A. Snavely et al. - *Intense High-Energy Proton Beams from Petawatt-Laser Irradiation of Solids*, ***Physical Review Letters*** **85**, 2945 (2000).
- [14] S. C. Wilks et al. - *Energetic proton generation in ultra-intense laser–solid interactions*, ***Physics of Plasmas*** **8**, 542 (2001).
- [15] T. Ceccotti et al. - *Proton Acceleration with High-Intensity Ultrahigh-Contrast Laser Pulses*, ***Physical Review Letters*** **99**, 185002 (2007).
- [16] S. C. Wilks et al. - *Absorption of ultra-intense laser pulses*, ***Physical Review Letters*** **69**, 1383, (1992).
- [17] S. C. Wilks - *Simulations of ultraintense laser–plasma interactions*, ***Physics of Fluids B: Plasma Physics*** **5**, 2603 (1993).

-
- [18] B. F. Lasinski et al. - *Particle-in-cell simulations of ultra intense laser pulses propagating through overdense plasma for fast-ignitor and radiography applications*, ***Physics of Plasmas* 6**, 2041 (1999).
- [19] S. P. Hatchett et al. - *Electron, photon, and ion beams from the relativistic interaction of Petawatt laser pulses with solid targets*, ***Physics of Plasmas* 7**, 2076 (2000).
- [20] P. A. Norreys et al. - *Observation of a highly directional γ -ray beam from ultrashort, ultraintense laser pulse interactions with solids*, ***Physics of Plasmas* 6**, 2150 (1999).
- [21] J. Fuchs et al. - *Laser-driven proton scaling laws and new paths towards energy increase*, ***Nature Physics* 2**, 48 (2006).
- [22] Y. Ping et al. - *Absorption of Short Laser Pulses on Solid Targets in the Ultrarelativistic Regime*, ***Physical Review Letters* 100**, 085004 (2008).
- [23] H. Alfvén - *On the Motion of Cosmic Rays in Interstellar Space*, ***Physical Review* 55**, 425 (1939).
- [24] A. R. Bell et al. - *Fast electron transport in laser-produced plasmas and the KALOS code for solution of the Vlasov–Fokker–Planck equation*, ***Plasma Physics and Controlled Fusion* 48**, R37 (2006).
- [25] F. Pisani et al. - *Experimental evidence of electric inhibition in fast electron penetration and of electric-field-limited fast electron transport in dense matter*, ***Physical Review E* 62**, R5927(R) (2000).
- [26] M. Roth, M. Schollmeier - *Ion Acceleration—Target Normal Sheath Acceleration*, ***CERN Yellow Reports* 1**, 231 (2016).
- [27] J. J. Honrubia et al. - *Simulations of heating of solid targets by fast electrons*, ***Laser and Particle Beams* 24**, 217 (2006).

- [28] J. J. Santos et al. - *Fast-electron transport and induced heating in aluminum foils*, ***Physics of Plasmas* 14**, 103107 (2007)
- [29] H. A. Bethe - *Molière's Theory of Multiple Scattering*, ***Physical Review* 89**, 1256 (1953).
- [30] J. R. Davies - *How wrong is collisional Monte Carlo modeling of fast electron transport in high-intensity laser-solid interactions?*, ***Physical Review E* 65**, 026407 (2002).
- [31] K. U. Akli et al. - *Temperature sensitivity of Cu K_α imaging efficiency using a spherical Bragg reflecting crystal*, ***Physics of Plasmas* 14**, 023102 (2007).
- [32] J. E. Crow, P. L. Auer, J. E. Allen - *The expansion of a plasma into a vacuum*, ***Journal of Plasma Physics* 14**, 65 (1975).
- [33] N. A. Krall, A. W. Trivelpiece - *Principles of Plasma Physics*, San Francisco Press, San Francisco (1986).
- [34] S. Augst et al. - *Tunneling ionization of noble gases in a high-intensity laser field*, ***Physical Review Letters* 63**, 2212 (1989).
- [35] M. Hegelich et al. - *MeV Ion Jets from Short-Pulse-Laser Interaction with Thin Foils*, ***Physical Review Letters* 89**, 085002 (2002).
- [36] P. McKenna et al. - *Lateral Electron Transport in High-Intensity Laser-Irradiated Foils Diagnosed by Ion Emission*, ***Physical Review Letters* 98**, 145001 (2007).
- [37] J. Schreiber et al. - *Source-size measurements and charge distributions of ions accelerated from thin foils irradiated by high-intensity laser pulses*, ***Applied Physics B* 79**, 1041 (2004).
- [38] M. Allen et al. - *Direct Experimental Evidence of Back-Surface Ion Acceleration from Laser-Irradiated Gold Foils*, ***Physical Review Letters* 93**, 265004 (2004).

-
- [39] M. Roth et al. - *Energetic ions generated by laser pulses: A detailed study on target properties*, ***Physical Review Special Topics - Accelerators and Beams*** **5**, 061301 (2002).
- [40] B. M. Hegelich et al. - *Laser acceleration of quasi-monoenergetic MeV ion beams*, ***Nature*** **439**, 441 (2006).
- [41] H. Schworer et al. - *Laser-plasma acceleration of quasi-monoenergetic protons from microstructured targets*, ***Nature*** **439**, 445 (2006).
- [42] S. Ter-Avetisyan et al. - *Quasimonoenergetic Deuteron Bursts Produced by Ultraintense Laser Pulses*, ***Physical Review Letters*** **96**, 145006 (2006).
- [43] D. C. Carroll et al. - *Active manipulation of the spatial energy distribution of laser-accelerated proton beams*, ***Physical Review E*** **76**, 065401(R) (2007).
- [44] M. Schollmeier - *Optimization and control of laser-accelerated proton beams*, Ph.D. thesis, Technische Universität Darmstadt (2008).
- [45] M. Borghesi et al. - *Fast Ion Generation by High-Intensity Laser Irradiation of Solid Targets and Applications*, ***Fusion Science and Technology*** **49**, 412 (2006).
- [46] T. E. Cowan et al. - *Ultralow Emittance, Multi-MeV Proton Beams from a Laser Virtual-Cathode Plasma Accelerator*, ***Physical Review Letters*** **92**, 204801 (2004).
- [47] S. Wilks, W. L. Kruer, M. Tabak, A. B. Langdon - *Absorption of ultra-intense laser pulses*, ***Physical Review Letters*** **69**, 1383 (1992).
- [48] J. Denavit - *Absorption of high-intensity subpicosecond lasers on solid density targets*, ***Physical Review Letters*** **69**, 3052 (1992).
- [49] L. O. Silva et al. - *Proton Shock Acceleration in Laser-Plasma Interactions*, ***Physical Review Letters*** **92**, 015002 (2004).

- [50] Y. Sentoku, T. E. Cowan, A. Kemp, H. Ruhl - *High energy proton acceleration in interaction of short laser pulse with dense plasma target*, ***Physics of Plasmas* 10**, 2009 (2003).
- [51] A. Pukhov - *Three-Dimensional Simulations of Ion Acceleration from a Foil Irradiated by a Short-Pulse Laser*, ***Physical Review Letters* 86**, 3562 (2001).
- [52] J. Fuchs et al. - *Experimental study of laser penetration in overdense plasmas at relativistic intensities. II: Explosion of thin foils by laser driven fast electrons*, ***Physics of Plasmas* 6**, 2569 (1999).
- [53] T. Schlegel et al. - *Relativistic laser piston model: Ponderomotive ion acceleration in dense plasmas using ultraintense laser pulses*, ***Physics of Plasmas* 16**, 083103 (2009).
- [54] O. Klimo, J. Psikal, J. Limpouch, V. T. Tikhonchuk - *Monoenergetic ion beams from ultrathin foils irradiated by ultrahigh-contrast circularly polarized laser pulses*, ***Physical Review Special Topics - Accelerators and Beams* 11**, 031301 (2008).
- [55] A. Macchi, S. Veghini, F. Pegoraro - *“Light Sail” Acceleration Reexamined*, ***Physical Review Letters* 103**, 085003 (2009).
- [56] M. Grech et al. - *Energy dispersion in radiation pressure accelerated ion beams*, ***New Journal of Physics* 13**, 123003 (2011).
- [57] M. Tamburini, et al. - *Radiation reaction effects on radiation pressure acceleration*, ***New Journal of Physics* 12**, 123005 (2010).
- [58] A. Henig et al. - *Radiation-Pressure Acceleration of Ion Beams Driven by Circularly Polarized Laser Pulses*, ***Physical Review Letters* 103**, 245003 (2009).
- [59] D. Haberberger et al. - *Collisionless shocks in laser-produced plasma generate monoenergetic high-energy proton beams*, ***Nature Physics* 8**, 95 (2011).

-
- [60] C.A. J. Palmer et al. - *Monoenergetic Proton Beams Accelerated by a Radiation Pressure Driven Shock*, ***Physical Review Letters*** **106**, 014801 (2011).
- [61] K. Matsukado et al. - *Energetic Protons from a Few-Micron Metallic Foil Evaporated by an Intense Laser Pulse*, ***Physical Review Letters*** **91**, 215001 (2003).
- [62] A. Yogo et al. - *Laser ion acceleration via control of the near-critical density target*, ***Physical Review E*** **77**, 016401 (2008).
- [63] S. V. Bulanov, T. Z. Esirkepov - *Comment on “Collimated Multi-MeV Ion Beams from High-Intensity Laser Interactions with Underdense Plasma”*, ***Physical Review Letters*** **98**, 049503 (2007).
- [64] L. Willingale et al. Reply, ***Physical Review Letters*** **98**, 049504 (2007).
- [65] S. S. Bulanov et al. - *Generation of GeV protons from 1 PW laser interaction with near critical density targets*, ***Physics of Plasmas*** **17**, 043105 (2010).
- [66] T. Nakamura, S. V. Bulanov, T.Zh. Esirkepov, M. Kando- *High-Energy Ions from Near-Critical Density Plasmas via Magnetic Vortex Acceleration*, ***Physical Review Letters*** **105**, 135002 (2010).
- [67] E. d’Humières et al. - *Investigation of high intensity laser proton acceleration with underdense targets*, ***Journal of Physics: Conference Series*** **244**, 042023 (2010).
- [68] T. ZH. Esirkepov et al. - *Ion acceleration by superintense laser pulses in plasmas*, ***Journal of Experimental and Theoretical Physics Letters***. **70**, 82 (1999).
- [69] M. Yamagiwa et al. - *Ion explosion and multi-mega-electron-volt ion generation from an underdense plasma layer irradiated by a relativistically intense short-pulse laser*, ***Physical Review E*** **60**, 5987 (1999).
- [70] Y. Sentoku et al. - *High density collimated beams of relativistic ions produced by petawatt laser pulses in plasmas*, ***Physical Review E*** **62**, 7271 (2000).

- [71] K. Krushelnick et al. - *Multi-MeV Ion Production from High-Intensity Laser Interactions with Underdense Plasmas*, ***Physical Review Letters*** **83**, 737 (1999).
- [72] L. Willingale et al. - *Collimated Multi-MeV Ion Beams from High-Intensity Laser Interactions with Underdense Plasma*, ***Physical Review Letters*** **96**, 245002 (2006).
- [73] P. Antici et al. - *Laser acceleration of high-energy protons in variable density plasmas*, ***New Journal of Physics*** **11**, 023038 (2009).
- [74] M. Hansson et al. - *Down-ramp injection and independently controlled acceleration of electrons in a tailored laser wakefield accelerator*, ***Physical Review Special Topics—Accelerators and Beams*** **18**, 071303 (2015).
- [75] G. Lapenta, Particle In Cell Method. A brief description of the PIC Method, url: <https://perswww.kuleuven.be/~u0052182/weather/pic.pdf> (visited on 09/27/2017).
- [76] D. Frenkel, B. Smit - *Understanding Molecular Simulation: From Algorithms to Applications*, Academic Press, San Diego (2002).
- [77] C. K. Birdsall, A. B. Langdon - *Plasma physics via computer simulation*, McGraw-Hill, Inc., New York (1985).
- [78] R. W. Hockney, J. W. Eastwood - *Computer simulation using particles*, Taylor & Francis, Inc. Bristol, PA, (1988).
- [79] G. Filipič - *Principles of “Particle in cell” simulations*, University of Ljubljana (2008)
(available at url: http://mafija.fmf.uni-lj.si/seminar/files/2007_2008/Seminar2.pdf).
- [80] Y. Sentoku, A. Kemp - *Numerical methods for particle simulations at extreme densities and temperatures: Weighted particles, relativistic collisions and reduced currents*, ***Journal of Computational Physics*** **227**, 6846 (2008).
- [81] P. Mora - *Plasma Expansion into a Vacuum*, ***Physical Review Letters*** **90**, 185002 (2003).

-
- [82] D. Dahiya, A. Kumar, V. K. Tripathi - *Influence of target curvature on ion acceleration in radiation pressure acceleration regime*, **Laser and Particle Beams** **33**, 143 (2015).
- [83] B. Qiao et al. - *Dynamics of high-energy proton beam acceleration and focusing from hemisphere-cone targets by high-intensity lasers*, **Physical Review E** **87**, 013108 (2013).
- [84] M. Zakova, et al. - *Reduction of angular divergence of laser-driven ion beams during their acceleration and transport*, **Proceedings SPIE 9515, Research Using Extreme Light: Entering New Frontiers with Petawatt-Class Lasers II**, 95151F (2015)
- [85] P. K. Patel, et al. - *Isochoric Heating of Solid-Density Matter with an Ultrafast Proton Beam*, **Physical Review Letters** **91**, 125004 (2003).
- [86] Y. Sentoku et al. - *Laser light and hot electron micro focusing using a conical target*, **Physics of Plasmas** **11**, 3083 (2004).
- [87] N. Renard-Le Galloudec, E. d’Humières - *New micro-cones targets can efficiently produce higher energy and lower divergence particle beams*, **Laser and Particle Beams** **28**, 513 (2010).
- [88] **D. Tatomirescu**, A. Popescu, E. d’Humières, D. Vizman - *Numerical simulation of laser ion acceleration at ultra high intensity*, **AIP Conference Proceedings** **1796**, 020013 (2017).
- [89] **D. Tatomirescu**, E. d’Humières, D. Vizman - *Improving the particle beam characteristics resulting from laser ion acceleration at ultra high intensity through target manipulation – Numerical modeling*, **AIP Conference Proceedings** **1916**, 030002 (2017).
- [90] R. R. Pandit, Y. Sentoku - *Higher order terms of radiative damping in extreme intense laser-matter interaction*, **Physics of Plasmas** **19**, 073304 (2012).

- [91] S. Buffechoux et al. - *Hot Electrons Transverse Refluxing in Ultraintense Laser-Solid Interactions*, **Physical Review Letters** **105**, 015005 (2010).
- [92] S. Chen et al. - *Focusing Dynamics of High-Energy Density, Laser-Driven Ion Beams*, **Physical Review Letters** **108**, 055001 (2012).
- [93] **D. Tatomirescu**, D. Vizman, E. d'Humières - *Target curvature influence on particle beam characteristics resulted from laser ion acceleration with microstructured enhanced targets at ultra-high intensity*, sent for publication in **Plasma Physics and Controlled Fusion** (2018).
- [94] F. Sylla et al. - *Development and characterization of very dense submillimetric gas jets for laser-plasma interaction*, **Review of Scientific Instruments** **83**, 033507 (2012).
- [95] R. Nuter et al. - *Maxwell solvers for the simulations of the laser-matter interaction*, **The European Physical Journal D** **68**, 177 (2014).
- [96] Y. Sentoku et al. - *Dynamic Control over Mega-Ampere Electron Currents in Metals Using Ionization-Driven Resistive Magnetic Fields*, **Physical Review Letters** **107**, 135005 (2011).
- [97] S. N. Chen, et al. - *Collimated protons accelerated from an overdense gas jet irradiated by a 1 μm wavelength high-intensity short-pulse laser*, **Scientific Reports** **7**, 13505 (2017).
- [98] P. Antici, et al. - *Acceleration of collimated 45 MeV protons by collisionless shocks driven in low-density, large-scale gradient plasmas by a 10^{20} W/cm², 1 μm laser*, **Scientific Reports** **7**, 16463 (2017).
- [99] **D. Tatomirescu**, D. Vizman, E. d'Humières - *Numerical modeling of laser-driven ion acceleration from near-critical gas targets*, **Plasma Physics and Controlled Fusion** **60**, 064002 (2018).

-
- [100] E. B. Saloman - *Energy Levels and Observed Spectral Lines of Xenon, XeI through XeLIV*, *J. Phys. Chem. Ref. Data*, Vol. **33**, No. **3** (2004).
- [101] J. Boris, in *Proceedings of the 4th Conference on the Numerical Simulation of Plasmas* (Naval Research Lab, Washington DC 1970).
- [102] E. d'Humières, et al. - *Optimization of laser- target interaction for proton acceleration*, *Phys. Plasmas* **20**, 023103 (2013).
- [103] H. Ruhl et al., *Plasma Phys. Rep.* **27**, 363 (2001).
- [104] R. A. Snavely et al., *Inertial Fusion Science and Applications 2003 Proceedings* (American Nuclear Society Inc., Monterey, CA, 2004), pp. 349.
- [105] D. T. Offermann et al., *Phys. Plasmas* **18**, 056713 (2011).
- [106] J. H. Bin et al., *Phys. Plasmas* **16**, 043109 (2009).
- [107] A. A. Andreev and K. Yu. Platonov, *Contrib. Plasma Phys.* **53**, 173 (2013).
- [108] D. Margarone et al., *Phys. Rev. Lett.* **109**, 234801 (2012).
- [109] C. McGuffey et al., in *Conference on Lasers and Electro-Optics/Pacific Rim* (Optical Society of America 2013), pp. TuD4_1.
- [110] F. Brunel, *Phys. Rev. Lett.* **59**, 52 (1987).
- [111] V. L. Ginzburg, *The Propagation of Electromagnetic Waves in Plasmas* (Pergamon, New York, 1964).
- [112] W. L. Kruer, *The Physics of Laser Plasma Interaction* (Addison-Wesley, New York, 1988).
- [113] E. S. Weibel, *Phys. Fluids* **10**, 741 (1967).
- [114] E. G. Gamaliy and V. T. Tikhonchuk, *JETP Lett.* **48**, 453 (1988).

- [115] P. J. Catto and R. M. More, *Phys. Fluids* **20**, 704 (1977).
- [116] J. T. Mendonca, *Phys. Rev. A* **28**, 3592 (1983).
- [117] Z. M. Sheng, K. Mima, Y. Sentoku, M. S. Jovanovic, T. Taguchi, J. Zhang, and J. Meyer-ter-Vehn, *Phys. Rev. Lett.* **88**, 055004 (2002).
- [118] A. Bourdier, D. Patin, and E. Lefebvre, *Laser Part. Beams* **25**, 169 (2007).
- [119] W. L. Kruer and K. Estabrook, *Phys. Fluids* **28**, 430 (1985).

Acknowledgements

Completing my doctoral studies and writing this thesis would have been impossible without the help and support of the people with whom I had the privilege to work.

First of all, I would like to thank Prof. Dr. Emmanuel d'Humières and Prof. Dr. Daniel Vizman for the confidence they gave me when they accepted to be my scientific coordinators. I also want to thank them for the help and advice given during my PhD studies and the professionalism with which they have led me to get the title of Doctor.

I would like to thank the members of the public defense committee for agreeing to participate in this event and for the advices they offered me that brought about the final version of my thesis.

I would also want to thank Lect. Dr. Alexandra Popescu for all the help and support she offered me during my PhD, especially for her help with the understanding of numerical modeling, the constructive discussions we had and her overall willingness to give me advices.

I also want to thank the members of the guidance committee, Prof. Dr. Marius Paulescu and Conf. Dr. Paul Barvinschi for the patience to analyze the doctoral thesis and for the constructive observations and suggestions that led to the improvement of the thesis.

Special thanks to my colleagues from the Numerical Modeling Laboratory from the Physics Faculty at West University of Timisoara, especially Vasile Pupazan, Radu Negrila, Oana Mares, Andrei Cordos and Stelian Arjoca for constructive discussions, peer counseling and moral support during my doctoral studies.

I would also want to thank my colleagues from the C.E.L.I.A. institute at the University of Bordeaux, especially Jonathan Page and Julien Moreau for their support and constructive discussions during my stays in Bordeaux.

I thank my friends, Liliana Beale, Adina Beale, Alin Chilom, Norbert Cara, Cristina Obeanu and Delia Costea, for the constant encouragement they have given me.

And, last but not least, I would like to thank my parents and my brother who have always been with me and who have always supported me.

This work has been supported by a grant of the Romanian National Authority for Scientific Research and Innovation, project number E13/30.06.2014 (ELICRYS) and 32-ELI/01.09.2016 (ELICRYS-2) in the frame of the ELI-RO Programme, ELI-NP Domain.

This work was also supported by the French National Research Agency Grant ANR-17-CE30-0026-02 PINNACLE.

This work was also granted access to the HPC resources of CINES under allocations A0020510052 and A0030506129 made by GENCI (Grand Equipement National de Calcul Intensif), and has been partially supported by the 2015-2019 grant of the Institut Universitaire de France obtained by CELIA.

This study has been carried out with financial support from the French State, managed by the French National Research Agency (ANR) in the frame of “the Investments for the future” Programme IdEx Bordeaux – LAPHIA (ANR--10--IDEX--03--02).

Annexes

Annexe 1. Xenon ionization module

Integration into the PICLS code of the energy levels and observed spectral lines that concern the Xenon atom, for all degrees of ionization. The values are extracted from experimental data compiled in [100].

```
...  
aIie(is,45)=      3.806d3  
aIie(is,46)=      3.806d3  
  
c..  Xenon (Z=54)  
else if(q(is).eq.54) then  
aIie(is, 0)=      0.121298420E+02  
aIie(is, 1)=      0.209750000E+02  
aIie(is, 2)=      0.310500000E+02  
aIie(is, 3)=      0.409000000E+02  
aIie(is, 4)=      0.541400000E+02  
aIie(is, 5)=      0.667030000E+02  
aIie(is, 6)=      0.916000000E+02  
aIie(is, 7)=      0.105976000E+03  
aIie(is, 8)=      0.179850000E+03  
aIie(is, 9)=      0.201700000E+03  
aIie(is,10)=      0.229020000E+03  
aIie(is,11)=      0.263500000E+03  
aIie(is,12)=      0.294400000E+03  
aIie(is,13)=      0.325300000E+03  
aIie(is,14)=      0.358300000E+03
```

aIie(is,15)= 0.389600000E+03
aIie(is,16)= 0.420900000E+03
aIie(is,17)= 0.452200000E+03
aIie(is,18)= 0.572500000E+03
aIie(is,19)= 0.607700000E+03
aIie(is,20)= 0.642900000E+03
aIie(is,21)= 0.678100000E+03
aIie(is,22)= 0.726000000E+03
aIie(is,23)= 0.762400000E+03
aIie(is,24)= 0.852700000E+03
aIie(is,25)= 0.857000000E+03
aIie(is,26)= 0.149000000E+04
aIie(is,27)= 0.149100000E+04
aIie(is,28)= 0.158700000E+04
aIie(is,29)= 0.168400000E+04
aIie(is,30)= 0.178100000E+04
aIie(is,31)= 0.187700000E+04
aIie(is,32)= 0.198700000E+04
aIie(is,33)= 0.208500000E+04
aIie(is,34)= 0.218300000E+04
aIie(is,35)= 0.228100000E+04
aIie(is,36)= 0.254800000E+04
aIie(is,37)= 0.263700000E+04
aIie(is,38)= 0.272600000E+04
aIie(is,39)= 0.281400000E+04
aIie(is,40)= 0.300100000E+04
aIie(is,41)= 0.309300000E+04
aIie(is,42)= 0.329600000E+04
aIie(is,43)= 0.333380000E+04
aIie(is,44)= 0.722400000E+04
aIie(is,45)= 0.749100000E+04
aIie(is,46)= 0.775800000E+04

```

aIie(is,47)=      0.802400000E+04
aIie(is,48)=      0.861700000E+04
aIie(is,49)=      0.889900000E+04
aIie(is,50)=      0.960672000E+04
aIie(is,51)=      0.981274720E+04
aIie(is,52)=      0.402727000E+05
aIie(is,53)=      0.412997000E+05

```

```

c..   Gold (Z=79)
else if(q(is).eq.79) then
aIie(is, 0)=      0.823000000E+01
aIie(is, 1)=      0.178230000E+02
...

```

Annexe 2. PICLS grid output for PARAVIEW compatible data files

In order to have a better and faster way of determining whether the input parameters are correct, and for ease of visualization of the final results of the numerical studies, I made the output files of the PICLS code compatible with the free visualization software PARAVIEW. The first step into this endeavor, was to write the grids used by the PICLS code, in order to have them available to the PARAVIEW software. This was performed using the following:

```

...
c ***** (dnss) *****
c... dragos 21/04/2017
c... output for paraview visualisation

iout=11
      if(combined_file_opt) then
mtag=1901

```

```
        all=0.d0
if(iam.eq.0) then
open(iout,
    \           file=dir(1:idirln)//'/dnss/dnss_all_'//label2)
    call
combined_diagout_av(nodes,Dns,0,Nx_pe,0,Ny_pe,1,N_sp,
    \           all,0,Nx,0,Ny,mtag,nd_parax,nd_paray,
    \           Nxp1,Nyp1,1)
    do j=0,Ny,Ny_d
        do i=0,Nx,Nx_d
            write(iout,1401)
i,j,(real(all(i,j,k)*dsv),k=1,N_sp)
        enddo
    enddo

    close(iout)
    if(zip_opt) then
        call system('gzip -f
'//dir(1:idirln)//'/dnss/dnss_all_'
    \           //label2)
endif

    if(zoom_opt) then
open(iout,
    \           file=dir(1:idirln)//'/dnss/dnss_zoom_'
    \           //label2)
    do j=Ny_ls,Ny_le,Ny_ld
        do i=Nx_ls,Nx_le,Nx_ld
            write(iout,1400)
(real(all(i,j,k)*dsv),k=1,N_sp)
        enddo
    enddo

    close(iout)

    if(zip_opt) then
        call system('gzip -f '//dir(1:idirln)//
    \           '/dnss/dnss_zoom_'//label2)
```

```
endif
endif
      else
isize=(Nx_pe+1)*(Ny_pe+1)*N_sp
      call MPI_SEND(Dns, isize, MPI_REAL8, 0, mtag,
        \          MPI_COMM_WORLD, info)
endif
      else
open(iout,
  \      file=dir(1:idirln)//'/dnss/dnss_all_'//label1
  \      //'_'//label2)
      do j=0, Ny_pe, Ny_d
        do i=0, Nx_pe, Nx_d
          write(iout, 1400) (real(Dns(i, j, is))*dsv), is=1, N_sp)
        enddo
      enddo
      close(iout)
      if(zip_opt) then
        call system('gzip -f
  //dir(1:idirln)//'/dnss/dnss_all_'
  \          //label1//'_'//label2)
      endif
endif
endif
1401 format(1p, ' ', i6.1, ' ', i6.1, ' ', e12.4, ' ', e12.4, ' ', e12.4)

c ***** (/dnss) *****
...
```

Scientific activity

ISI articles

1. **Dragos Tatomirescu**, Daniel Vizman, Emmanuel d’Humières - *Numerical modeling of laser-driven ion acceleration from near-critical gas targets*, ***Plasma Physics and Controlled Fusion* 60**, 064002 (2018).
IF: 3.032; AIS: 0.767
2. **Dragos Tatomirescu**, Daniel Vizman, Emmanuel d’Humières - *Target curvature influence on particle beam characteristics resulted from laser ion acceleration with microstructured enhanced targets at ultra-high intensity*, ***Plasma Physics and Controlled Fusion*** (sent for publication).
IF: 3.032; AIS: 0.767

ISI indexed articles

1. **Dragos Tatomirescu**, Emmanuel d’Humières, Daniel Vizman - *Improving the particle beam characteristics resulting from laser ion acceleration at ultra high intensity through target manipulation – Numerical modeling*, ***AIP Conference Proceedings* 1916**, 030002 (2017)

2. **Dragos Tatomirescu**, Alexandra Popescu, Emmanuel d'Humières, Daniel Vizman - *Numerical simulation of laser ion acceleration at ultra high intensity*, *AIP Conference Proceedings* **1796**, 020013 (2017).

International conference participations

1. **EPS 2018 Physics Conference**, Prague (Czech Republic) 02-06/07/2018
 - **Dragos Tatomirescu**, Emmanuel d'Humières, Daniel Vizman - *Influence of the peak density of near-critical gas targets on the spectrum features using ultra-high laser intensity through numerical modelling*

2. **15e congrès de la Division Plasmas de la SFP**, Bordeaux (France) 12-14/06/2018
 - **Dragos Tatomirescu**, Emmanuel d'Humières, Daniel Vizman - *Near-critical gas targets peak density influence on the accelerated particles spectrum features using ultra-high laser intensity through numerical modelling*

3. **TIM18 Physics Conference**, Timisoara (Romania) 24-26/05/2018
 - **Dragos Tatomirescu**, Alexandra Popescu, Daniel Vizman, Emmanuel d'Humières - *Near-critical gas targets peak density influence on the accelerated particles spectrum features using ultra-high laser intensity through numerical modelling*

4. **EPS 2017 Conference**, Belfast (Northern Ireland) 26-30/06/2017
 - **Dragos Tatomirescu**, Emmanuel d’Humières, Daniel Vizman - *Target curvature influence on particle focusing and maximum energy in laser-plasma acceleration at ultra high intensity*

5. **TIM17 Physics Conference**, Timisoara (Romania) 22-28/05/2017
 - **Dragos Tatomirescu**, Emmanuel d’Humières, Daniel Vizman - *Improving the Particle Beam Characteristics Resulted from Laser Ion Acceleration at Ultra High Intensity through Target Manipulation – Numerical Modeling*

6. **TIM 15-16 Physics Conference**, Timisoara (Romania) 26-28/05/2016
 - **Dragos Tatomirescu**, Alexandra Popescu, Emmanuel d’Humières, Daniel Vizman - *Numerical simulation of laser ion acceleration at ultra high intensity*

Summer schools participations

1. **2nd ELI Summer School – ELISS 2017**
27 August - 1 September 2017, Cheile Gradistei - Fundata, Romania

2. **International Summer School on Crystal Growth and Advanced Materials for Energy Conversion**
10 - 15 July 2017, Bucharest, Romania

3. **Parallel filesystems and parallel IO libraries @MdlS (Maison de la simulation)**
6 March 2017, Gif-sur-Yvette, France

4. **CERN - SEENET - MTP PhD Training program in High Energy Physics – “Computational methods in Cosmology and General Relativity”**
11 - 17 December 2016 Timisoara, Romania

5. **First NESUS Winter school & PhD Symposium**
8 - 11 February 2016 Timisoara, Romania

6. **1st ELI-NP Summer School – “Perspectives in Physics with High-Power Lasers and Gamma Beams”**
21 - 25 September 2015, Bucharest, Romania

7. **International Summer School on Materials for Energy Conversion**
6 - 11 July 2015, Bucharest, Romania